UNIVERSITY OF CALIFORNIA

Los Angeles

Hydrodynamical Simulations of Turbulence in Galactic Centers

A dissertation submitted in partial satisfaction

of the requirements for the degree

Doctor of Philosophy in Astronomy and Astrophysics

by

Jesus Mario Salas

2021

ABSTRACT OF THE DISSERTATION

Hydrodynamical Simulations of Turbulence in Galactic Centers

by

Jesus Mario Salas
Doctor of Philosophy in Astronomy and Astrophysics
University of California, Los Angeles, 2021
Professor Mark R. Morris, Co-Chair
Professor Smadar Naoz, Co-Chair

Turbulence is a prevalent phenomenon in the interstellar medium, and in particular, in the environment at the centers of galaxies. For example, detailed observations of the Milky Way's Central Molecular Zone (CMZ) have revealed that it has a complex and turbulent structure. It is suspected that turbulence is responsible for maintaining the relatively high temperatures in the CMZ, as well as for suppressing star formation. Therefore, turbulence is a key phenomenon for understanding the dynamics and energetics of this region.

In galactic-scale simulations, turbulence is often modeled by invoking star formation and supernovae feedback. However, these phenomena do not appear to be sufficient for explaining the high-velocity dispersion observed in the CMZ, indicating that additional gas-stirring processes are likely to be operating. In this thesis, I present a new numerical method to drive turbulence in galactic centers. Instead of relying on a particular physical mechanism, I have adopted a Fourier forcing module, which has the advantage of being independent of the actual sources of turbulence, but which is adjustable to the scales needed to match observations. I have applied this method using a Smoothed Particle Hydrodynamics (SPH) code. This

turbulence injection method is capable of balancing the self-gravity of gas in different physical scenarios, which allows the simulations to be run for long timescales, thereby enabling my study of the effects of turbulence on the gas dynamics.

First, I introduce this new numerical tool and present simulations of a simplistic model of the CMZ to showcase its performance and numerical convergence. I find that turbulence induces a flocculent spiral pattern similar to that observed in the centers of other galaxies. Furthermore, the driving module induces a turbulent viscosity which enhances mass inflow to the center.

To further show the flexibility and applicability of this method, I present larger-scale simulations of galactic nuclear rings. Nuclear rings are a common feature of galaxies which form due to the effects of bar potentials, and the CMZ contains such a ring. I find that turbulence thickens nuclear rings and enhances mass accretion towards the center, both effects caused by turbulent viscosity. This mass inflow could explain the feeding of material from the CMZ to the inner few parsecs of the Galaxy.

As a final example of my method's versatility, I performed simulations of the Circumnuclear Disk (CND) at the center of the Milky Way. The transient vs long-lived nature of the CND is widely debated in the literature. Some authors have argued that the observed stream morphology and non-axisymmetric density distribution implies that the CND is a transient structure. However, the results of my simulations suggest that these arguments are not correct. I find that turbulent perturbation on sufficiently large scales, such as those that would be produced by supernova blast waves, creates a disk with a non-uniform density structure, and promotes the creation of streams that endure for longer than a few dynamical timescales.

In conclusion, the work I present in this thesis shows that my injection method is a flexible tool that can be applied to a variety of physical scenarios. Furthermore, this method can be

adapted to different hydrodynamical codes based on alternative hydrodynamics techniques.

The dissertation of Jesus Mario Salas is approved.

Andrea M. Ghez

Bradley M. S. Hansen

Smadar Naoz, Committee Co-Chair

Mark R. Morris, Committee Co-Chair

University of California, Los Angeles

2021

TABLE OF CONTENTS

LIST OF FIGURES

LIST OF TABLES

ACKNOWLEDGMENTS

This material is based upon work supported by the National Science Foundation Graduate Research Fellowship Program under Grant No. DGE-1144087. This work used computational and storage services associated with the Hoffman2 Shared Cluster provided by UCLA Institute for Digital Research and Education's Research Technology Group. This work also used the Extreme Science and Engineering Discovery Environment (XSEDE) Comet at the San Diego Supercomputer Center at UC San Diego through allocations AST170039 and AST180051. XSEDE is supported by National Science Foundation grant number ACI-1548562.

I acknowledge that the results presented in this thesis are based on published works with additional coauthors. Chapter 2 is a version of Salas et al. (2021), which was written in collaboration with my advisors, Professor Mark R. Morris and Professor Smadar Naoz. Similarly, Chapter 3 is a version of a Salas et al. (2020), which was written also in collaboration with Professors Morris and Naoz. Chapter 4 is a version of Dinh et al. (2021), which is work done in collaboration with UCLA student Cuc K. Dinh, as well as Professors Morris and Naoz. Finally, Appendix A presents the paper Salas et al. (2019), which was done in collaboration with Professors Morris and Naoz, and former UCLA graduate student Alexander P. Stephan.

VITA

2010–2014 B.S. — Physics
Texas A&M University - Kingsville

2014–2016 M.S. — Astronomy
University of California, Los Angeles

PUBLICATIONS

J. M. Salas, M. R. Morris, S. Naoz, "Modeling turbulence in galactic centers". AJ, 161, 243 (2021)

C. K. Dinh, **J. M. Salas**, M. R. Morris, S. Naoz, 2021 "Effects of turbulence in the Circumnuclear Disk " arXiv:2102.09569

J. M. Salas, S. Naoz, M. R. Morris, 2020, "The effects of turbulence on galactic nuclear gas rings". arXiv:2010.04170

J. M. Salas, S. Naoz, M. R. Morris, A. Stephan, "Unseen companions of V Hya inferred from periodic ejections", MNRAS, 487, 3029 (2019)

CHAPTER 1

Introduction

1.1 Background and motivation

Turbulence is one of the major dynamical processes governing the structure and evolution of the interstellar medium (ISM, Elmegreen & Scalo, 2004a). For example, supersonic turbulence is known to be a dominant process in regulating (both inhibiting and fostering) star formation in molecular clouds (McKee & Ostriker, 2007). However, galactic centers show a number of interesting deviations from the star formation behavior seen at larger galactic radii. For example, molecular clouds in our own Galactic Center (GC) show systematic differences in their properties from clouds in the Galactic disk: they appear to have thermal, turbulent and magnetic pressures much higher than those present in the large-scale Galactic disk (e.g., Spergel & Blitz, 1992).

The main gaseous feature of the GC, the Central Molecular Zone (CMZ), has a rich and complex structure that extends over a galactocentric radius of ~ 300 pc and contains a mass of M$\sim 3-7\times10^7$ M$_\odot$ (e.g., Morris & Serabyn, 1996). It is largely composed of relatively dense ($n \sim 10^3$-10^5 cm^{-3}) and warm gas ($\sim 70-100$ K on average, e.g., Güsten et al. 1981; Morris et al. 1983; Huettemeister et al. 1993; Ao et al. 2013), mostly condensed into Giant Molecular Clouds (GMCs) or dense tidal streams of molecular gas. These relatively warm gas temperatures are one of the key properties of CMZ clouds, and there is evidence showing that the gas is kept warm by the dissipation of turbulence (e.g., Immer et al., 2016; Ginsburg

et al., 2016). It has also been suggested that turbulence plays a role in the suppression of star formation in this region (e.g., Kruijssen et al. 2014). However, the driving mechanism for the turbulence in CMZ clouds has not been conclusively identified (see Kruijssen et al. 2014 for a discussion of possible sources of turbulence). Furthermore, the large turbulent velocity dispersion within the CMZ must be responsible for supporting the gas against gravitational collapse, since the thermal pressure of the gas would be insufficient.

Numerical simulations have shown that interstellar turbulence decays quite rapidly, on timescales of the order of the free-fall time of the system (e.g., Mac Low, 1999). Therefore, energy must be injected into the system in order to maintain the turbulence. Simulations of turbulence-driven gas are often employed in studies of the interstellar medium and star formation (e.g., Stone et al., 1998; Mac Low et al., 1998; Krumholz & McKee, 2005; Burkhart et al., 2009; Federrath et al., 2010). Typically, this is achieved by a Fourier forcing module, which can be modelled with a spatially static pattern in which the amplitude is adjusted in time (Stone et al., 1998; Mac Low, 1999). Other studies employ a forcing module that can vary both in time and space (e.g., Padoan et al., 2004; Schmidt et al., 2006; Federrath et al., 2010).

In the case of galactic-scale simulations, driven turbulence is mimicked by injecting energy due to supernovae (SN). For example, simulations by Kim et al. (2011); Emsellem et al. (2015); Shin et al. (2017); Seo et al. (2019); Armillotta et al. (2019), and Tress et al. (2020) have modelled turbulence by using star formation and SN feedback models. In general, these models depend on underlying assumptions regarding star formation rates, SN energies and injection rates. Furthermore, recent studies (e.g., Scannapieco et al., 2012; Rosdahl et al., 2017; Keller & Kruijssen, 2020) have demonstrated that the different choices of SN feedback model (including the underlying physical processes driving the feedback) produce significant differences in morphology, density, etc, of the simulated galaxies. Also, it has been shown that despite the high densities and the large amount of available gas, there is about an

order of magnitude less active star formation in the CMZ than might be expected from the quantity and surface density of molecular gas (e.g., Longmore et al., 2013; Kruijssen et al., 2014). Therefore, other physical processes may supplement this methodology to explain the high-velocity dispersions observed in the CMZ.

For these reasons, I was prompted to develop a more general mechanism for driving turbulence in the CMZ that could account for multiple sources of turbulence. Consequently, I adapted the Fourier forcing module described by Mac Low (1999) in order to simulate not just the CMZ, but as I show in this thesis, this method can be applied in general to gas that orbits under the influence of a galactic potential.

1.2 Structure of the dissertation

My thesis is outlined as follows:

I present in Chapter 2 a review of Salas et al. (2021). I describe the numerical methods behind this turbulence driving module, which is based on the Fourier model by Mac Low (1999). In order to examine its effectiveness, I use a simplistic model of the CMZ consisting of spherical giant molecular clouds. I describe the tests that were performed in order to find the optimal parameters that yielded consistent gas densities over long time-scales. I found that turbulence induces a spiral structure in CMZ, similar to that observed in other galactic centers. Additionally, I find that my method induces a turbulent viscosity, which enhances mass inflow towards the galactic center. I also describe all the additional components of my turbulence method, which could be modified and adapted to other physical scenarios.

Chapter 3 is a description of the paper Salas et al. (2020), in which I apply this driving method to study the effects of turbulence on simulations of nuclear gaseous rings. Nuclear rings are a common feature of barred galaxies, and our Galaxy is thought to have such a ring in the form of the CMZ ring (Molinari et al., 2011; Henshaw et al., 2016). While

nuclear rings are well understood in terms of the elementary theory of galactic dynamics, this model does not account for the effects of turbulence in the evolution of nuclear rings. My simulations revealed that turbulence thickens nuclear rings and induces a filamentary structure. Turbulence also enhances mass accretion to the inner few parsecs of the galaxy, which could help explain the mechanism behind the mass inflow from the CMZ to the Galactic Center.

Chapter 4 details the results from Dinh et al. (2021). This paper was written in collaboration with UCLA undergraduate student Cuc K. Dinh, whom I mentored for this project. In this Chapter I describe simulations of the circumnuclear disk (CND), in which we use a modified version of my turbulence injection method. The transient nature of the CND has been debated in the literature; some suggest the CND is a short-lived disk, while others argue for a longer-lived disk. We find that turbulence promotes a long-lived disk, as well as create streams and clumps, similar to the observed morphology of the CND. Furthermore, our results suggest that some of the clumps described in observations may actually be artifacts due to the resolution of observations and the orientation of the CND.

In Chapter 5 I summarize the results of my thesis, and submit that my turbulence methods is a promising new tool for hydrodynamical simulations to model turbulence in galactic centers.

Additionally, I present in Appendix A a project separate from the main topic of this thesis, which consists of exploring a new hypothesis to explain the mysterious ejections of the star V-Hydrae.

CHAPTER 2

A new turbulence injection method for SPH

2.1 Introduction

In this Chapter I present a summary of my paper, Salas et al. (2021), which introduces a proof-of-concept method to drive turbulence in gas that orbits under the influence of a galactic potential. Instead of relying on a particular physical mechanism, I adopt a Fourier forcing module, which has the advantage of being independent of the source of turbulence. My turbulence treatment is based on the method described by Mac Low (1999), in which a turbulent velocity field is drawn from a spatially static pattern having a power spectrum $P(k) \propto k^{-n}$, where k is the wavenumber. I apply this method to the code Gadget2 (Section 2.2.1) and I test its effectiveness using a simplistic model of the CMZ.

2.2 Numerical methods

Here I present below a brief summary of the numerical methods.

2.2.1 Gadget2 code

All hydrodynamical simulations shown in this thesis were performed with the fully parallel, N–body/SPH code Gadget2 (Springel, 2005). The code is based on the tree–Particle Mesh (treePM) method for computing the gravitational forces and on the standard SPH method for solving the 3D Euler equations of hydrodynamics. For a full description of the code, see

Springel (2005). For a full review of the theory and applications of SPH, see, e.g, G. R. Liu (2003) and Monaghan (2005).

Hydrodynamics

Smoothed particle hydrodynamics (SPH) is a numerical method for solving the equations of fluid dynamics. It uses a set of tracer particles ("fluid elements") which sample the gas. Each particle, i, has a spatial coordinate (r_i), velocity (v_i) and mass (m_i), and the continuous fluid quantities (density, internal energy, etc) are defined by a kernel interpolation technique: the SPH interpolation of a quantity B is based on the interpolating kernel W:

$$B(\mathbf{r}) \approx \int B'(\mathbf{r}) W(\mathbf{r} - \mathbf{r'}, h) d\mathbf{r}' \tag{2.1}$$

Equation 2.1 reproduces B exactly if W is a delta function. The kernel is generally a function which tends to the delta function as the length scale h (called the smoothing length) tends to zero. Gadget2's SPH formulation of the density estimate is in the form:

$$\rho_i = \sum_{j=1}^{N} m_j W(|r_{ij}|, h), \tag{2.2}$$

where ρ_i is the density of (the fluid element traced by) a particle, m_j is the particle's mass, and $r_{ij} = r_i - r_j$ is the distance between two neighboring particles. $W(r, h)$ is defined in Gadget2 as

$$W(r,h) = \frac{8}{\pi h^3} \begin{cases} 1 - 6\left(\frac{r}{h}\right)^2 + 6\left(\frac{r}{h}\right)^3, & 0 \leqslant \frac{r}{h} \leqslant \frac{1}{2} \\ 2\left(1 - \frac{r}{h}\right)^3, & \frac{1}{2} < \frac{r}{h} \leqslant 1 \\ 0, & \frac{r}{h} > 1 \end{cases} \tag{2.3}$$

In Gadget2, the thermodynamic state of each particle is defined in terms of its thermal

energy per unit mass, e_i, which is later converted to entropy per unit mass, A_i [1], and used as the independent thermodynamic variable evolved in SPH.

In this entropy formulation of SPH, the (adaptive) smoothing lengths h_i of each particle are defined such that their kernel volumes contain a constant mass for the estimated density, i.e.,

$$\frac{4\pi}{3} h_i^3 \rho_i = N_{neigh} \bar{m} \tag{2.4}$$

where N_{neigh} is the typical number of smoothing neighbors, and $\bar{m}$ is an average particle mass. For equal–mass particles, this is equivalent to demanding that the number of neighbors (N_{neigh}) be constant, and the accuracy of SPH calculations relies on this requirement, as shown by Attwood et al. (2007). Therefore, in all simulations shown in this thesis, N_{neigh} is set by the code's default value of 64 $\pm \Delta N_{neigh}$, where ΔN_{neigh} is the allowed variation of the number of neighbors, set by default to a value of 2. If the number of neighbors is outside this range of $\pm \Delta N_{neigh}$, the code will adapt the smoothing length to ensure N_{neigh} is again in this range.

Provided there are no shocks or external sources of heat, the entropy formulation used in Gadget2 manifestly conserves both energy and entropy, even when fully adaptive smoothing lengths are used (Springel & Hernquist, 2002). On the contrary, traditional formulations of SPH can violate entropy conservation in some situations. However, flows of ideal gases can easily develop discontinuities, where entropy is generated by micro–physics. In SPH, such shocks need to be captured by an artificial viscosity. Gadget2 adopts the Monaghan–Balsara form of the artificial viscosity (Monaghan & Gingold, 1983; Balsara, 1995). The strength of the viscosity is regulated by the parameter α_{MB}. In all simulations presented in this thesis, I used the code's default value of 0.75 (see Eq. 14 in Springel 2005).

[1] A_i is actually an entropic function defined as $P_i = A_i \rho_i^\gamma$, where P_i is the pressure on particle i, and γ is the adiabatic index. However, since for an ideal gas A_i only depends on the entropy, in Gadget2 A_i is simply referred as the "entropy".

Gravity

Gadget2 uses a hierarchical multipole expansion, commonly called a tree algorithm (Barnes & Hut, 1986), to calculate the gravitational forces. In a three–dimensional N–body simulation, the Barnes–Hut algorithm divides the N particles into groups by storing them in a cubical root node that encloses the whole space (octree). The octree is then repeatedly subdivided into eight "children", which represent the eight octants of the space, until "leaf" nodes containing single particles are constructed.

The calculation of the net force on a particle is obtained by "walking" the tree, starting from the root: if the center of mass of an internal node is sufficiently far from a particle, the particles inside that node are treated as a single body whose position and mass are the center of mass and total mass of the internal node, respectively. If the node is sufficiently close to the particle, the process is repeated for each of its children.

Gadget2 also offers a treePM algorithm (Xu, 1995) for the computation of gravitational forces. This method restricts the tree algorithm to short–range scales, while computing the long–range gravitational force by means of a Particle Mesh (PM) algorithm (Hockney & Eastwood, 1988; Efstathiou et al., 1985). In the PM algorithm, a system of particles is converted into a grid (or "mesh") of density values. The potential is then solved for this density grid using Fast Fourier Transforms, from which the gravitational acceleration can be obtained. By testing the performance of both algorithms, I opted for using the tree algorithm in all my simulations, since it provided faster results.

The gravitational acceleration at short range is also kernel–softened to avoid large accelerations and the need for increasingly small timesteps. Gadget2 uses a Plummer softening length, ϵ, and uses the same kernel (Eq. 2.3) as for SPH. The particles are also allowed to have individual gravitational softening lengths, and their values are adjusted such that for every time step, ϵ_i/h_i is of order unity. The positions and velocities of particles are advanced

through a complete time step by means of a leapfrog algorithm.

The simulations presented in this chapter consider self-gravity (i.e., the mutual gravitational interactions between the SPH particles). The smoothing length of each particle in the gas is fully adaptive down to a set minimum of 0.001 pc. I modified the standard version of Gadget2 to include the gravitational potential of a Milky Way-like galaxy, and the effects of pressure by a surrounding medium. I describe these modifications below.

2.2.2 External Pressure

The interstellar medium of the GC is modeled via an external pressure term to approximate a constant pressure boundary. Following Clark et al. (2011), I modify Gadget2's momentum equation (Springel & Hernquist, 2002):

$$\frac{dv_i}{dt} = -\sum_j m_j \left[f_i \frac{P_i}{\rho_i^2} \nabla_i W_{ij}(h_i) + f_j \frac{P_j}{\rho_j^2} \nabla_i W_{ij}(h_j) \right] \tag{2.5}$$

where v_i is the velocity of particle i, m_j is the mass of particle j, P_i is the pressure, ρ_i is the density, $W_{ij}(h_i)$ is the kernel function which depends on the smoothing length h_i, and f is a unitless coefficient that depends on ρ_i and h_i. I replace P_i and P_j with $P_i - P_{ext}$ and $P_j - P_{ext}$, respectively, where P_{ext} is the external pressure. The pair-wise nature of the force summation over the SPH neighbors ensures that P_{ext} cancels for particles that are surrounded by other particles. At the boundary, where the P_{ext} term does not disappear, it mimics the pressure contribution from a surrounding medium (Clark et al., 2011). I set P_{ext} equal to 10^{-10} ergs cm^{-3}, an approximate value for the GC (Spergel & Blitz, 1992; Morris & Serabyn, 1996).

2.2.3 The galactic potential

To calculate the gravitational potential, I use the density profile from Zhao et al. (1994):

$$\rho(r, \theta, \phi) = \rho_0 \left(\frac{r}{r_0} \right)^{-p} \left[1 + Y(\theta, \phi) \right] , \tag{2.6}$$

which is a modified version of the prolate bar density profile introduced by Binney et al. (1991). The gravitational potential then has the form:

$$\Phi(r,\theta,\phi) = 4\pi G\rho_0 r_0^2 \left(\frac{r}{r_0}\right)^{\alpha} P(\theta,\phi) \ , \tag{2.7}$$

where (r,θ,ϕ) are spherical coordinates fixed on the rotating bar[2], $\alpha = 2-p$, and $P(\theta,\phi)$ is the associated Legendre function, which can be written as:

$$P(\theta,\phi) = \frac{1}{\alpha(1+\alpha)} - \frac{Y(\theta,\phi)}{(2-\alpha)(3+\alpha)} \ , \tag{2.8}$$

and $Y(\theta,\phi)$ is a linear combination of spherical harmonic functions of the $l=2$, $m=0,2$ modes:

$$Y(\theta,\phi) = -b_{20}P_{20}(\cos\theta) + b_{22}P_{22}(\cos\theta)\cos 2\phi \ . \tag{2.9}$$

The parameter b_{20} determines the degree of oblateness/prolateness while b_{22} determines the degree of non-axisymmetry. Motivated by the previous work of Kim et al. (2011), and more recently of Gallego & Cuadra (2017)[3], I use the parameters: $\alpha = 0.25$, $b_{20} = 0.3$, $b_{22} = 0.1$, $\rho_0 = 40$ M$_\odot$ pc^{-3} and $r_0 = 100$ pc. Given these parameters, a bar with axis ratios of [1: 0.74: 0.65] is obtained for the isodensity surface that intersects points [$x=0$, $y=\pm 200$ pc, $z=0$]. Enclosed masses inside 200 pc and 1000 pc are 10^9 M$_\odot$ and 7×10^9 M$_\odot$, respectively.

In addition to the gravitational force due to the potential above, I introduced the rotation of the bar by adding centrifugal and Coriolis forces. I used the most recent estimate for the Galactic bar's pattern speed ($\Omega_{bar} = 40$ km s^{-1} kpc^{-1}; e.g., Bland-Hawthorn & Gerhard 2016; Portail et al. 2017).

[2]The coordinate $r = \sqrt{x^2+y^2+z^2}$, where x, y, z are the standard Cartesian coordinates. The supermassive black hole would be at $r=0$, the bar's major axis is aligned with the x-axis, and the z axis represents the vertical direction, with the galactic plane at $z=0$

[3]I note that there is a negative sign misprint in Kim et al. (2011) (their Equation 2) and in Gallego & Cuadra (2017) (their associated Legendre function).

2.3 Turbulence Driving

As noted in the Introduction of this thesis, driven turbulence is often modelled using one of two types of Fourier forcing modules. Both methods require Fourier transforms on a cubic grid (or lattice) with N^3 points (or a square lattice with N^2 on 2D simulations, where typical values for N = 128, 256, 1024, etc). By imposing this cubic lattice onto a simulation box with a physical size of L per side, I can use the separation between adjacent lattice points (L/N) as a proxy for the resolution of the turbulence. Hence, for a large-scale simulation such as the CMZ environment, e.g., $L = 500$ pc, and simultaneously resolving turbulence on small scales, e.g., 0.01 pc, the turbulence cubic lattice would have to contain $N^3 = 5000^3$ points, which would require massive computational resources. To circumvent this limitation, I instead use many smaller turbulence grids to fill the volume of my larger simulation box, as follows:

First, I create a library of 10 files, which my modified version of the Gadget2 code reads in at the start of the simulation. Each file contains a unique realization of a turbulent velocity field (in the form of a 3D matrix) with power spectrum $P(k) \propto k^{-4}$ (suitable for compressible gas; e.g., Clark et al. 2011). Each of these 3D matrices of turbulence is generated using the methods described in Rogallo (1981) and Dubinski et al. (1995): via fast Fourier transforms inside a 128^3 box.

These 3D turbulence matrices can be visualized as lattice cubes (or grids) with equally spaced lattice points, containing $128 \times 128 \times 128$ points. The parameter that sets the physical size of these cubes is named L_{cube}. In the test model used in this chapter, I make the simplifying assumption that turbulence is injected on scales similar to the average size of CMZ clouds, i.e., $L_{cube} = 8$ pc per side. Thus, the separation between two adjacent lattice points along one axis is $8\text{pc}/128 = 0.0625$ pc.

In some studies, the driving module only contains power on the larger scales (e.g., Federrath

et al. 2010). This type of driving models the kinetic energy input from large-scale turbulent fluctuations, which then break up into smaller structures as the kinetic energy cascades down to scales smaller than the turbulence injection scale. However, in SPH, the artificial viscosity may damp this energy cascade and prevent it from reaching the smaller scales. Consequently, to create the different realizations of turbulent velocity fields, I use a discrete range of k values from $k_{min} = 2$ to $k_{max} = 128$, thus effectively injecting energy on scales between $L_{cube}/2 = 4$ pc (for $k = 2$) and $L_{cube}/128 = 0.06$ pc (for $k = 128$). To create the initial (turbulent) velocity field of an individual cloud (see Section 2.4), I use trilinear interpolation to calculate the velocity components for each SPH particle, based on that particle's position on a turbulence cube. This interpolation method results in a turbulent velocity function $\vec{I}(x, y, z)$.

Next, I use $64 \times 64 \times 64$ cubes of turbulence to fill up the volume of my large simulation box. This gives me a simulation box of size $L_{global} = 8\text{pc} \times 64 = 512$ pc per side. Thus, the spatial resolution of the turbulence in my large simulation box is the same as the resolution of an individual turbulence lattice cube. Each of the turbulence lattice cubes that fill up the large simulation box is randomly chosen from my library of 10 files, thereby avoiding a velocity field that is coherent over scales greater than L_{cube}. A 2D graphic representation of the method I describe here is shown in Figure 2.1. This method raises a concern regarding the interface between the turbulence cubes, namely, that there will be discontinuities in the turbulent velocity kicks throughout the gas at the cubes' interfaces. However, the turbulent velocity added to the gas is quite small in comparison with the orbital velocity, and indeed, I find in practice that there are no obvious shocks or discontinuities at the interfaces that exceed those induced by the injected velocity increments (see Section 2.6).

To drive the turbulence, I follow a method similar to that described by Mac Low (1999): every N_t timesteps (I fixed the timestep in all my simulations to $\Delta t_s = 1000$ yrs) I add a

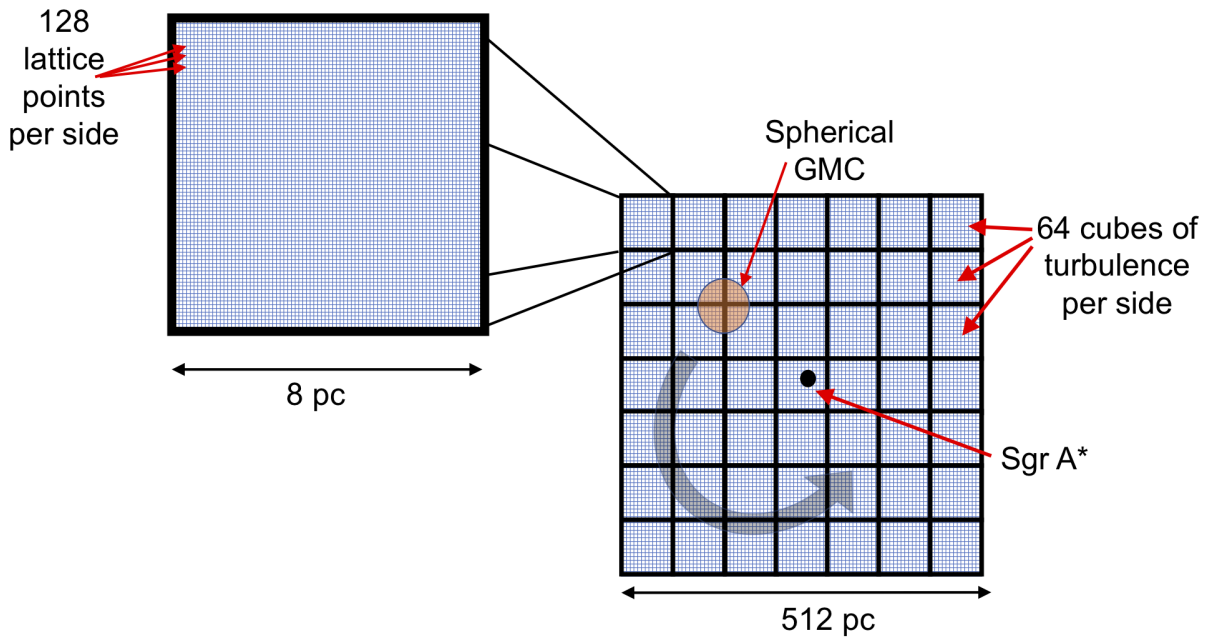

Figure 2.1: Two dimensional representation of my turbulence driving method. A single turbulence cube is shown on the left, while the combination of cubes to fill up the large simulation box is shown on the right. Note that the above schematic is intended for illustration purposes, since the number of cubes sketched is different from what I actually used.

velocity increment to every SPH particle, given by:

$$\Delta\vec{v}(x,y,z) = A\sqrt{G\rho}\ \vec{I}(x,y,z)\ , \tag{2.10}$$

where $\vec{I}(x,y,z)$ is the turbulent velocity interpolated from the turbulence field of the cube that contains the particle in question. The amplitude A is chosen to maintain a constant kinetic energy input rate $\dot{E_{in}} = \Delta E_{in}/(N_t \Delta t_s)$, and the term $\sqrt{G\rho}$ is added to counteract gravitational collapse by ensuring that higher-density regions receive more kinetic energy[4]. Any particle outside the $(512\ \mathrm{pc})^3$ simulation box does not receive any turbulent energy.

For compressible gas with a time-dependent density distribution, maintaining a constant kinetic energy input rate requires solving a quadratic equation in the amplitude A every time the driving is performed (Mac Low, 1999). For N_{sph} particles of mass m_p, each with density ρ_i, A is derived from (see Section 2.8):

$$\Delta E_{in} = \frac{1}{2} m_p \sum_{i=1}^{N_{sph}} \left[A^2 G \rho_i \vec{I_i} \cdot \vec{I_i} + 2A\sqrt{G\rho_i}\ \vec{I_i} \cdot \vec{v_{1,i}} \right] \ . \tag{2.11}$$

Following Mac Low (1999), I take the larger root as the value for A.

Therefore, my methodology introduces two adjustable parameters: ΔE_{in}, the energy input per injection, and N_t, the number of timesteps between injections.

Finally, to mimic the random nature of turbulence, I change the turbulent velocity field of each of the 64^3 cubes every time the driving is performed. This is done by replacing each of the cubes with a different one, chosen randomly from the 10 files in my library. See Section 2.8 for further details.

[4]This density factor stems from the assumption that molecular clouds are supported against gravitational collapse by turbulence, and therefore the velocity kicks should be inversely proportional to the free-fall time, $t_{ff} \propto (G\rho)^{-1/2}$.

2.4 Initial conditions

To initiate the computations, I use a fiducial model of the central region of the Milky Way, consisting of a collection of 100 initially isolated, spherical GMCs. Each cloud contains $N_p = 10^4$ particles, with mass $m_p = 30$ $M_\odot$ per particle. The clouds are distributed randomly in an annular disk of inner radius 30 pc, outer radius 200 pc, and a Gaussian scale height of 30 pc. Each cloud has a radius of 4 pc, and an initial turbulent velocity field such that $|E_{turb}/E_{pot}| = 0.5$ (i.e., they are initially in virial equilibrium). The clouds' initial center of mass velocities were set so that they move on circular orbits and are parallel to the galactic plane, with their magnitudes (v_ϕ) calculated using the potential described in Section 2.2.3. In order to also give the system a broader vertical structure, the initial v_z components of each cloud were set such that $v_z = 0.5 v_\phi$, with the v_z vector always pointing towards the galactic plane. Figure 2.2 shows the initial snapshot of my CMZ model.

All simulations were run using an isothermal equation of state with $T = 100$ K. This assumption of isothermal gas is somewhat crude, but may still provide an adequate physical approximation to the real thermodynamics in dense molecular gas (Wolfire et al., 1995; Pavlovski et al., 2006).

During my testing phase, I also considered an initially uniform disk as my initial condition. Except for the time to reach a steady-state (see Section 2.6), the end result was qualitatively identical to the model described in this chapter. I therefore conclude that the specific features of the initial conditions are unimportant for my purposes as long as the particles are initially distributed over the same domain. I opted for a collection of clouds as my initial conditions due to the flexibility in setting the position, size, mass, initial turbulent velocity field, etc, of each individual cloud.

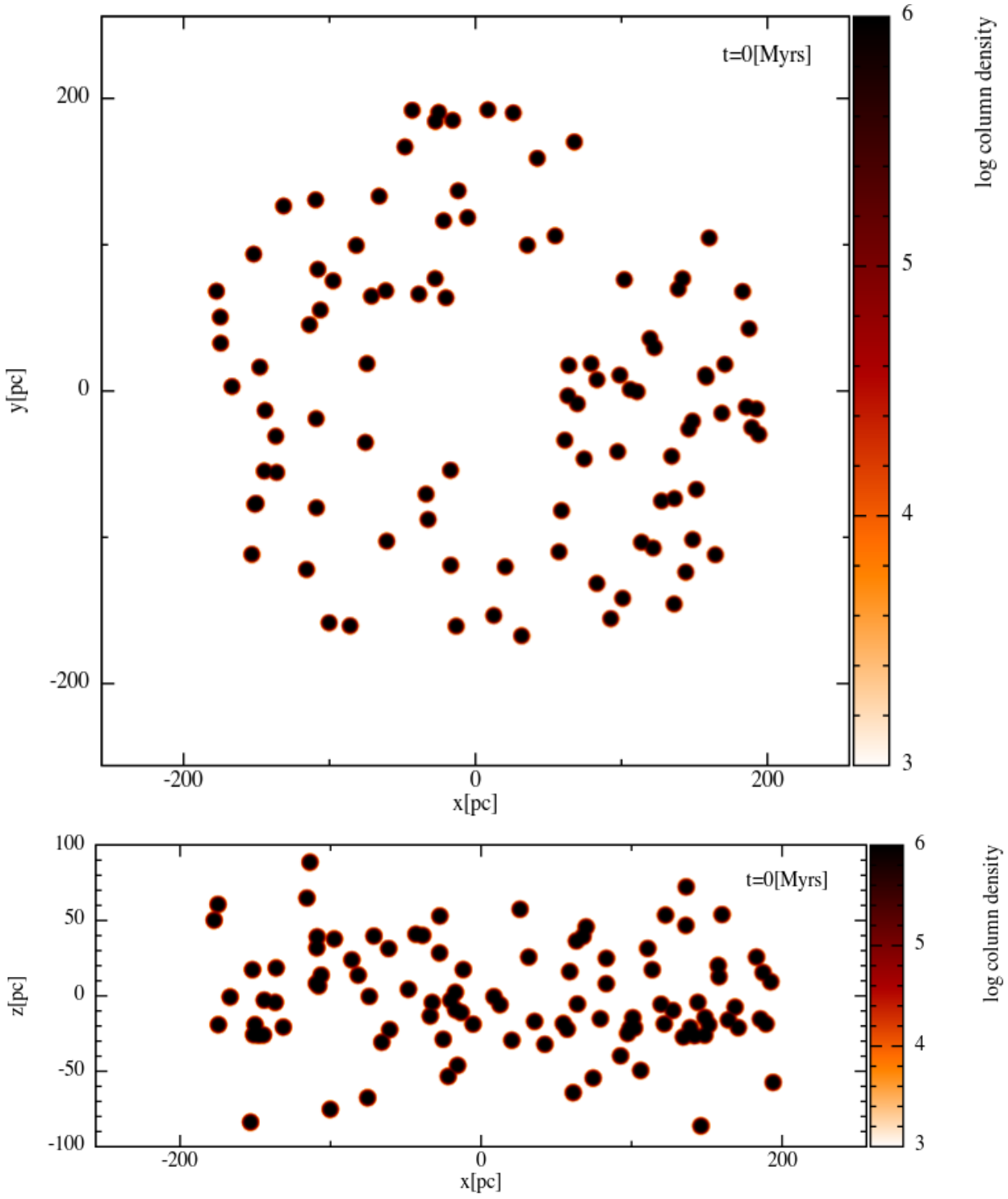

Figure 2.2: Initial conditions for my test simulations, x-y plane and edge-on view. Color bar indicates column number density in log scale (units in cm^{-3} pc).

2.5 Convergence and consistency tests

When the self-gravity of the gas is included, combined with a relatively low temperature, my CMZ simulations without injected turbulence experience runaway gravitational collapse, causing the simulations to fail within a dynamical timescale ($\sim 0.1 - 0.3$ Myrs). This effect can be alleviated by increasing the softening length (which in my simulations is set equal to the smoothing length, i.e., 0.001 pc). In such a case, the simulation can run for long timescales, however the gas concentrates to unphysically large densities, causing the simulation to slow down to an impractical pace, and is thus an expensive use of computing resources. This result thereby emphasizes the importance of the turbulence injection method introduced in this chapter. However, turbulence injected too infrequently leads to the same result as if there was no turbulence injection: gas collapses locally to unphysically large densities (see Section 2.9). Therefore, it is important to inject turbulence relatively often.

In practice, the turbulence driving method described in Section 2.3, adds an additional velocity "kick" to each particle every N_t timesteps. The energy ΔE_{in} injected per N_t timestep is kept constant. With these two free parameters I conducted several tests using my CMZ model to find the optimal range of values that give rise to reasonable densities over long timescales. I varied the energy input ΔE_{in} from 10^{46} to 10^{50} ergs, and N_t from 1 to 5. I describe in detail all performed tests in Section 2.9. My tests led me to the choice of parameters $N_t = 2$, $\Delta E_{in} = 10^{47}$ ergs (e.g., see Figure 2.12).

2.6 Results

I ran the system for 250 Myrs, using the initial conditions described in Section 2.4, the turbulence parameters described in Section 2.5, and including self-gravity. The system reaches a semi-steady state after $50-100$ Myrs regardless of the turbulence parameters (as described in Section 2.9), and thus the choice of 250 Myrs allows me to capture the relevant dynamics (see below). I also ran a simulation without turbulence (and self-gravity turned off) for

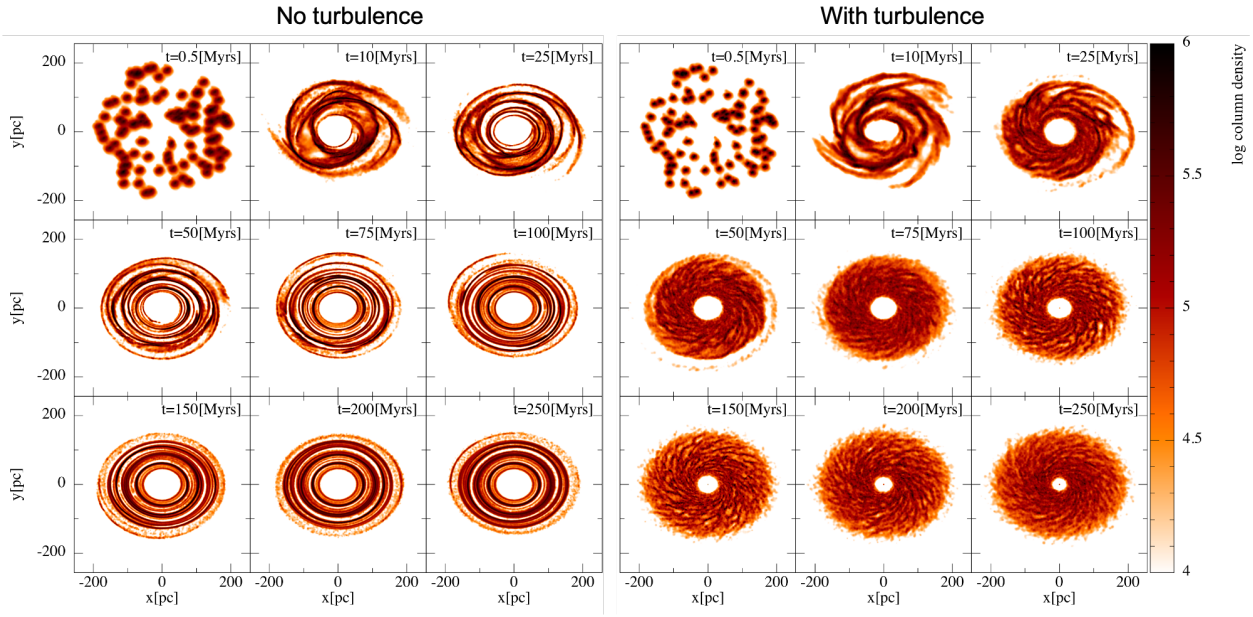

Figure 2.3: Column number density at different times for the no-turbulence run (left) and turbulence run (right). The long axis of the bar is oriented along the x-axis. The color map is in logarithmic scale. Units are in cm^{-3} pc.

comparison. I show the face-on and edge-on views of the resulting column density evolution of my simulations in Figures 2.3 and 2.4, respectively. The results shown here indicate that my turbulence injection module is capable of balancing the self-gravity of gas concentrations, which allows me to run the simulation for long timescales. Furthermore, discontinuities due to the grids' interfaces are unnoticeable, as anticipated.

In both runs, the clouds are tidally stretched relatively quickly, and the gas settles into a disk after $\sim$ 50 Myrs. In the simulation without turbulence, the clouds are stretched into gas streams which comprise the disk, and reaches steady state by $\sim$ 50 Myrs. The inner inner cavity of radius $\sim$ 30 pc, which is a product of the initial conditions, remains unchanged for the entire simulation.

However, there are two major differences between the two simulations. First, the resulting streams in the simulation with turbulence coalesce into a disk with a flocculent spiral pattern.

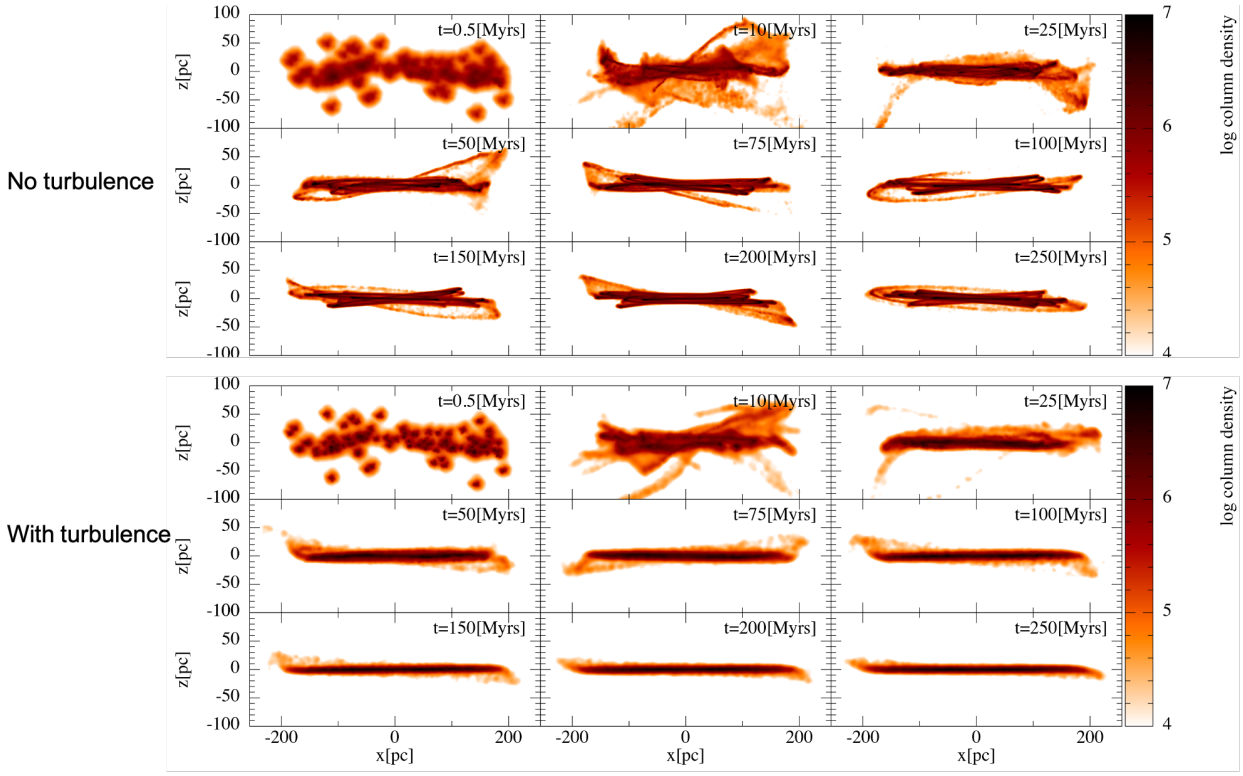

Figure 2.4: Edge-on view of the column number density at different times for the no-turbulence run (top) and turbulence run (bottom). The long axis of the bar is oriented along the x-axis. The color map is in log scale. Units are in cm^{-3} pc. The simulation without turbulence exhibits a more pronounced vertical structure than the simulation with turbulence. This is because in the simulation with turbulence, self-gravity is included, and thus the mutual gravitational interactions between particles compresses the disk to the galactic plane.

Second, the inner cavity fills in slowly over time. I address each of these differences below.

2.6.1 Spiral structure

After running for ~ 50 Myrs, the gas in the run with turbulence settles into a quasi-steady state with a flocculent spiral pattern (because of the constantly injected turbulence, a perfect steady state cannot occur). These spiral segments are attributable to the dynamical response of my self-gravitating, shearing disk to local density perturbations (e.g., Julian & Toomre 1966), which in this case are caused by the forced turbulence. It is a common result that turbulence promotes the development of high-density regions due to convergent flows (e.g., Elmegreen & Scalo 2004a; McKee & Ostriker 2007).

A similar result was found on galactic scales by D'Onghia et al. (2013). The spiral patterns in their simulations of self-gravitating disks of stars are not global as predicted by classical static density wave theory, but locally they appear to fluctuate in amplitude with time. Their spirals are actually segments produced by sheared local under-dense and over-dense regions. These under-dense and over-dense regions act as gravitational perturbers, maintaining the local spiral morphology. In my case, it is the injected turbulence that acts as the local perturber in the gas.

Furthermore, observations of galactic centers have revealed intricate dust structures that are often organized in a clear spiral pattern. For example, the survey studies by Regan & Mulchaey (1999); Martini & Pogge (1999); Pogge & Martini (2002) and Martini et al. (2003a,c) indicate that $\sim 50 - 80\%$ of galaxies in their samples possess nuclear spirals, regardless of their nuclear activity. The pattern of some of the observed nuclear spirals is highly organized, similar to grand-design spirals in main galactic discs. Others display a more chaotic, or flocculent, spiral pattern. A direct comparison between my simulations and observations is difficult due to the limited spatial resolution of the observations, however, my results suggest that turbulence could be (at least partially) responsible for the spiral pattern

observed in the gas layer in the centers of galaxies.

2.6.1.1 Effects of external pressure

As discussed in Section 2.2.2, I modified Gadget2 to model an external pressure boundary, as opposed to the vacuum or periodic boundary conditions that are the only choices in the standard version of the code. I used an observationally motivated value of $P_{ext} = 10^{-10}$ erg cm^{-3} for the Galactic Center. However, it is worth investigating how varying this pressure term affects the gas morphology. I ran two additional simulations with $P_{ext} = 0$ (standard vacuum boundary conditions) and $P_{ext} = 10^{-9}$ erg cm^{-3}, which is an order of magnitude greater than the value from my fiducial simulations. I show the column density maps (both face-on and edge-on) at $t = 100$ Myr in Figure 2.5. As depicted, without the external pressure term (see left panels in Figure 2.5), the gas disk has a smooth boundary at the edges, as well as material above and below the plane. When the external pressure term is introduced with my fiducial value, it pushes the low density gas at the edge towards the disk, and it increases the density contrast of the flocculent spiral pattern. Similarly, when the pressure term is large ($P_{ext} = 10^{-9}$ erg cm^{-3}, right panels in Figure 2.5), the density contrast of the spirals is increased further. Furthermore, the material above and below the plane is pushed towards the disk. Interestingly, this behaviour suggests an observational test for the value of external pressure, which may be used for systems in which the pressure is undetermined.

2.6.2 Inward migration

The inner cavity closes slowly over time, as gas migrates inward. This might imply a loss of angular momentum in the system due to the turbulence. In Figure 2.6 I show the total (specific) angular momentum over time for both simulations. Despite my strategy for avoiding adding a net angular momentum to the simulations (see Section 2.8), I see that, in the run with turbulence, angular momentum slightly decreases, from $\sim 1.45 \times 10^{10}$ km s^{-1} pc at 50 Myrs to $\sim 1.4 \times 10^{10}$ km s^{-1} pc at 250 Myrs, a difference of $\sim 3\%$. Clearly, the

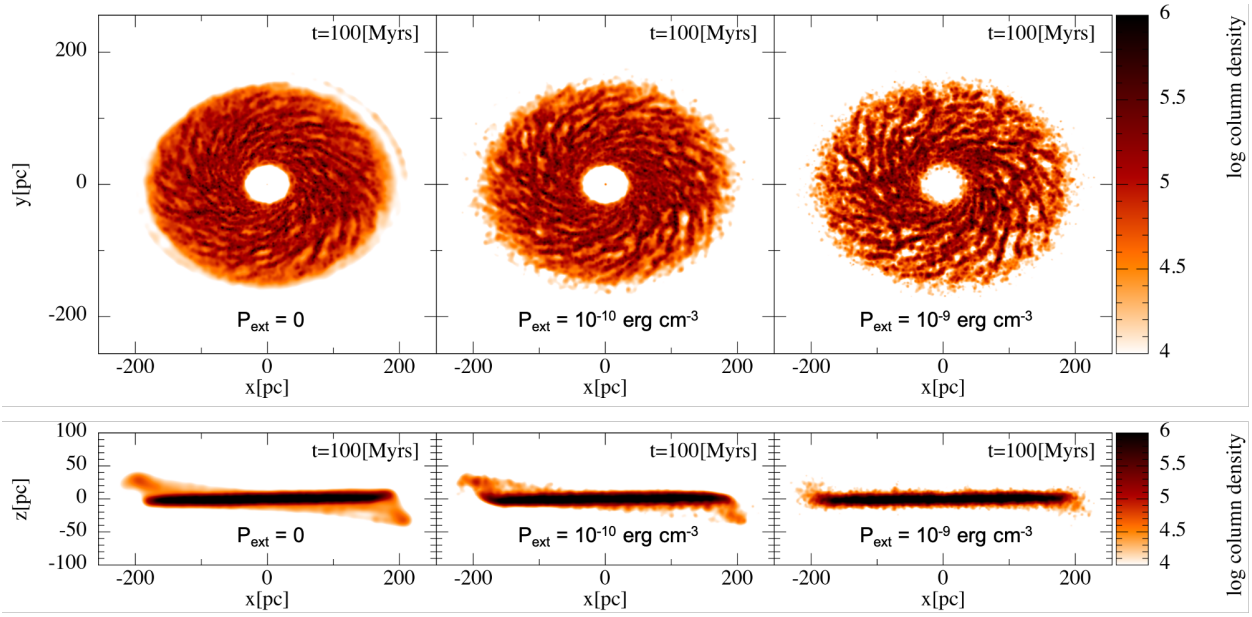

Figure 2.5: Column number density maps of three simulations performed to compare between different values of P_{ext}. The turbulence parameters are the same as my fiducial run (N_t=2, ΔE_{in}=10^{47} ergs). The top panels show the face-on views, while the bottom panels show the edge-on views. Left panels: vacuum boundaries (no external pressure). Middle panels: P_{ext} = 10^{-10} erg cm^{-3}, same as my fiducial model (e.g., Figure 2.3). Right panels: P_{ext} = 10^{-9} erg cm^{-3}, i.e., a factor of 10 greater than my fiducial model. The external pressure pushes the lower density gas into the disk and enhances the density contrast of the gas spiral arms.

sign switching strategy I describe in Section 2.8 does not completely ensure angular momentum conservation. Furthermore, it has been shown that turbulence can impose a nonzero angular momentum (e.g., Clark et al., 2011). However, this change is quite small over long timescales, and thus I do not consider this to be the reason for the inward migration[5].

Conversely, it has been shown that supersonic turbulence inside accretion disks (e.g., Wang et al. 2009) can promote accretion onto SMBHs by enhancing angular momentum transfer (e.g., Collin & Zahn 2008; Chen et al. 2009). In particular, Hobbs et al. (2011) demonstrated using numerical simulations of supermassive black hole accretion that turbulence can broaden the angular momentum distribution, setting some gas on low angular momentum orbits. I find a similar result in Figure 2.7, where I show the mass fraction as a function of specific angular momentum at different times for both simulations. I find that in the simulation without turbulence (left panel of Figure 2.7) the gas settles into a triple-peaked distribution by 100 Myrs (red curve), and the location of these peaks, as well as the overall distribution, does not change over time. In contrast, the simulation with turbulence exhibits an angular momentum distribution with a single peak (right panel of Figure 2.7). This peak then slowly moves towards lower angular momentum values over time.

This transport of angular momentum can be explained in terms of the elementary theory of accretion disks (e.g., Shakura & Sunyaev, 1973; Lynden-Bell & Pringle, 1974; Pringle, 1981): viscous torques between adjacent annuli of gas in an accretion disk provokes mass to flow inwards. While Gadget2 does contain an artificial viscosity, this treatment is dedicated to capturing shocks in SPH, and has no effect on the transfer of angular momentum, as seen in my turbulence-free simulation (Figure 2.3). The transport of angular momentum is

[5]I verified that the inward migration is indeed a feature of the injected turbulence by considering the possibility that the interaction between turbulence and the rotating, non-axisymmetric potential could have led to this angular momentum decrease. I tested this idea by running a simulation with a rotating, axisymmetric potential (by setting $b_{22} = 0$ and $\Omega_{bar} = 40$ km s^{-1} kpc^{-1}, see Section 2.2.3), and another with a non-rotating, axisymmetric potential (by setting $b_{22} = 0$ and $\Omega_{bar} = 0$). However, in both cases, I recover the same negative slope as in my fiducial model (red line in Figure 2.6). Thus, I conclude that this small angular momentum reduction is a feature of the injected turbulence.

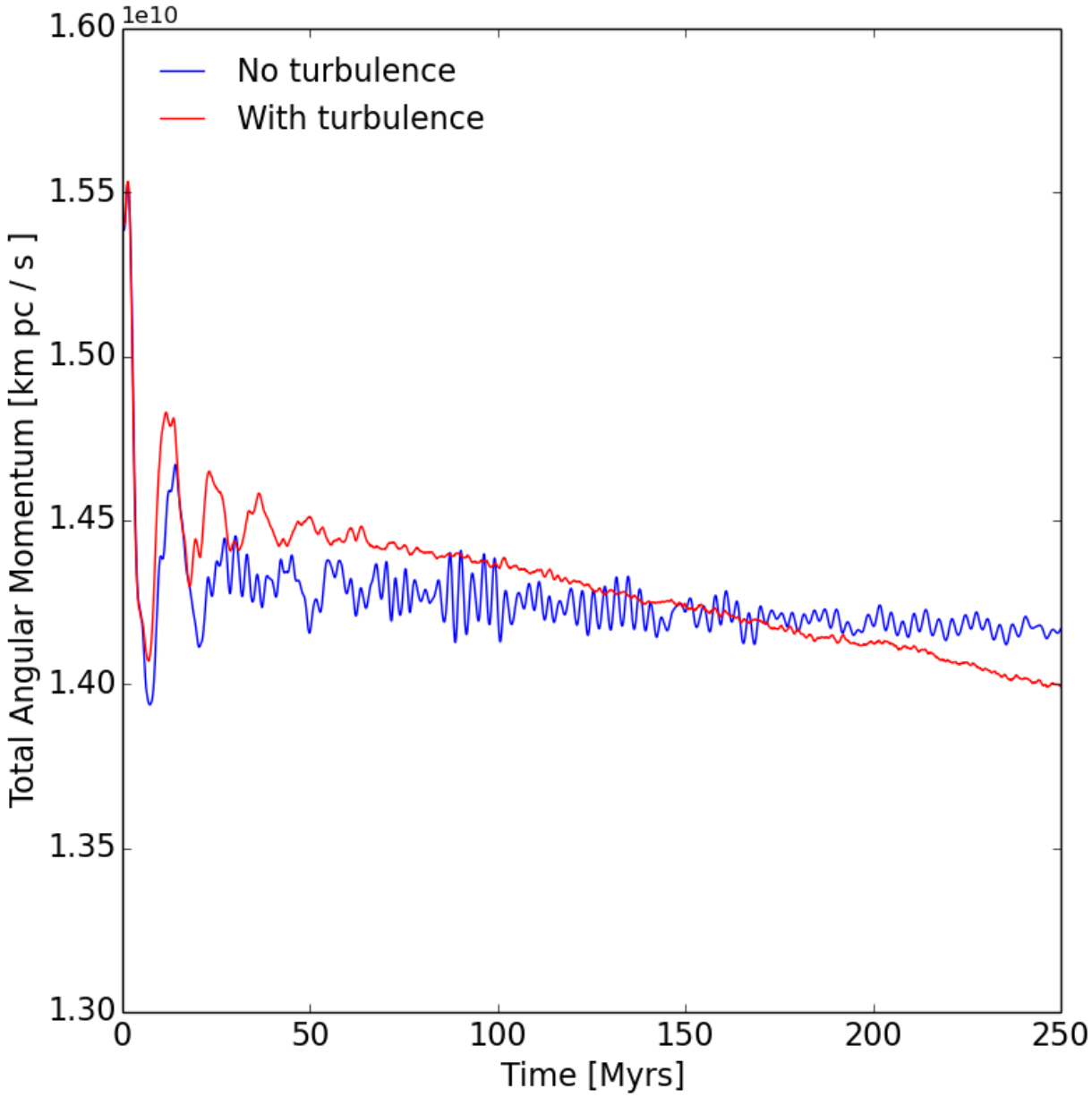

Figure 2.6: Evolution of the total specific angular momentum (l) in the simulations. In the run with turbulence, l decreases slightly, with a difference of $\sim$ 3% between 50 and 250 Myrs. However, this change is sufficiently small that the angular momentum can be considered approximately constant.

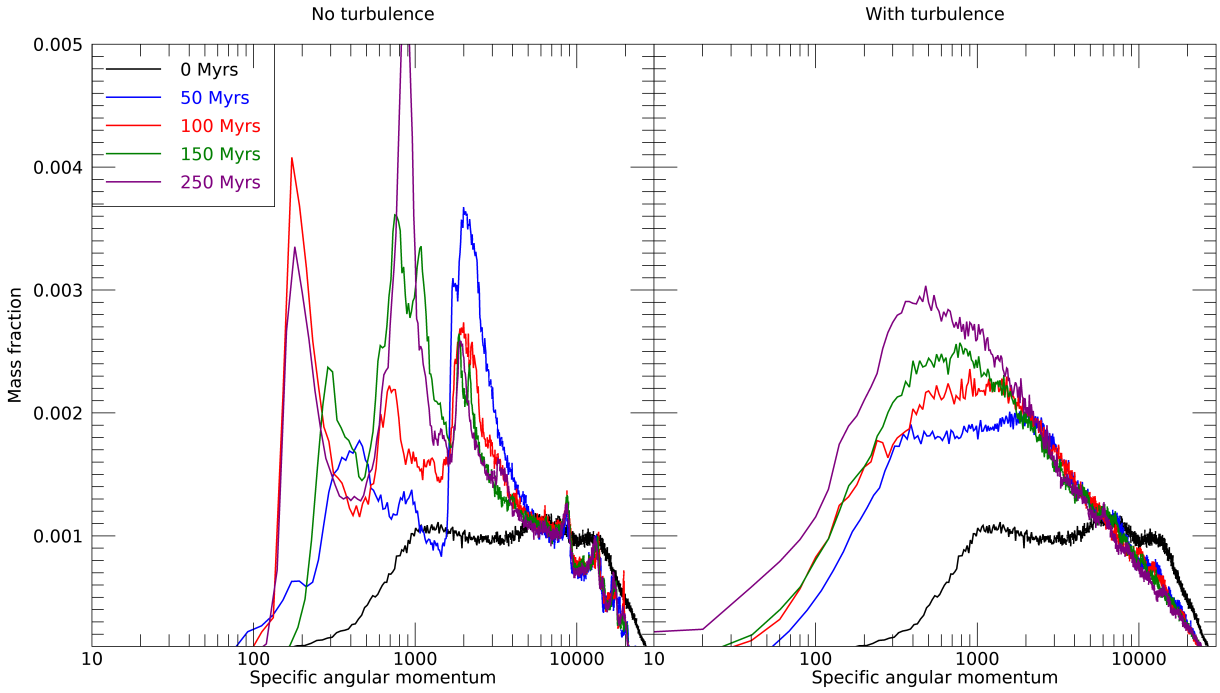

Figure 2.7: Distribution of the mass fraction of gas as a function of specific angular momentum (units of km pc s^{-1}) at different times for the simulations without turbulence (left) and with turbulence (right). The graph was calculated using a specific angular momentum bin size of 20 km pc s^{-1}. In the simulation without turbulence, the shape of the distribution is relatively unchanged after 100 Myrs. In contrast, the angular momentum settles into a single-peak distribution in the run with turbulence, and this peaks shifts towards lower angular momentum values over time, thus accounting for the inward migration of gas.

due to "turbulent" viscosity induced by my driving method. This explains the slow inward migration of gas in my simulation.

To estimate the viscosity, ν_{turb}, induced by my turbulence method, I use the accretion rate due to α-viscosity (Shakura & Sunyaev, 1973; Pringle, 1981):

$$\dot{M} \approx 3\pi\nu_{turb}\Sigma, \tag{2.12}$$

where $\dot{M}$ is the mass inflow rate and Σ is the surface density.

To estimate $\dot{M}$, I calculate the mass inside a radius of 30 pc over time (see Figure 2.8). I approximate the rate from 150 Myrs to 250 Myrs as a straight line, and find a slope of $\dot{M} = 0.004$ $M_\odot$/yr. Similarly, I adopt the value of Σ at r = 30 pc to be 300 $M_\odot/pc^2$, which is the average value between 150 and 250 Myrs (see Figure 2.9). Thus, I evaluate the viscosity to be $\nu_{turb} = 4.2 \times 10^{23}$ cm^2/s.

Alternatively, I can use the definition of α-viscosity $\nu_{turb} = \alpha c_s H$, where $\alpha \leq 1$ is a parameter that adjusts the strength of the viscosity, c_s is the sound speed, $H = c_s/\Omega$, and Ω is the angular velocity due to the gravitational potential. Assuming the gas in my simulations is mainly composed of molecular hydrogen (H_2), $c_s = 0.64$ km/s. The value of H at r = 30 pc is ~ 0.2 pc (see Figure 2.10). This results in a value for $\nu = 3.7 \times 10^{22}$ cm^2/s (assuming $\alpha = 1$). However, the actual thickness of the disk at $r = 30$ pc is much larger, ~ 2 pc (see Figure 2.10). Using this value, I obtain $\nu_{turb} = 3.7 \times 10^{23}$ cm^2/s, which is comparable to the value I calculated above using the mass inflow rate.

To understand the implications of this calculated turbulent viscosity, I make a comparison similar to that described in Sormani et al. (2018), as follows: to significantly affect the dynamics of a gaseous disk, the viscous timescale, $t_\nu \sim R^2/\nu$ (where R is the radius of the disk), must be shorter than the Hubble time ($t_H = 14$ Gyrs). This condition gives a lower limit to the value of the viscosity, $\nu_{min} \approx R^2/t_H$. Using $R = 200$ pc (the radius of my simulated CMZ disk) gives a minimum viscosity of $\nu_{min} = 8 \times 10^{23}$ cm^2/s. This value

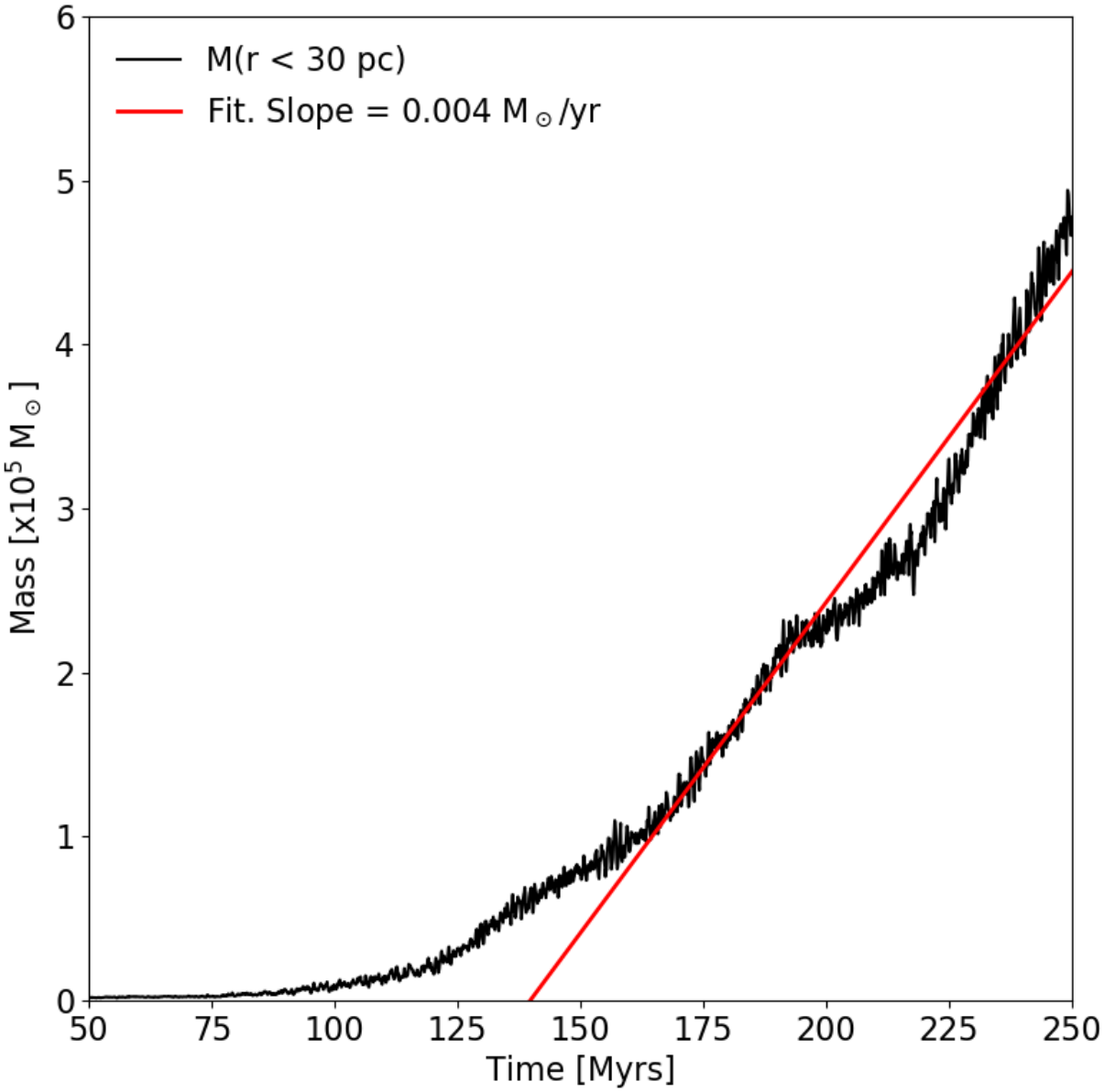

Figure 2.8: Plot of the mass inside a radius of 30 pc over time (simulation with turbulence). To estimate the mass inflow rate, I approximate the rate from t = 150 Myrs to 250 Myrs as a straight line. The slope of the fit is 0.004 $M_\odot$/yr.

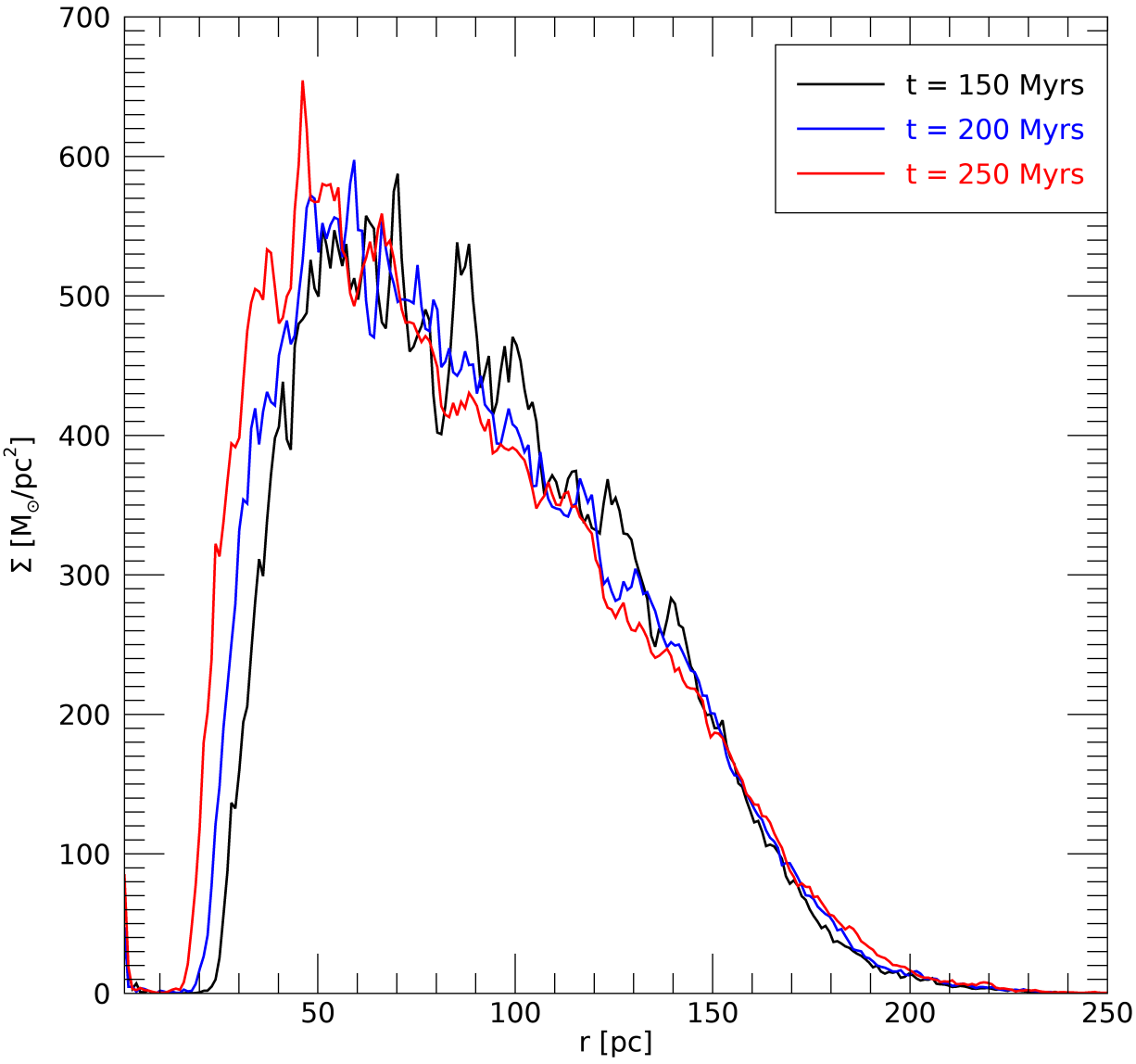

Figure 2.9: Plot of surface density of the simulation with turbulence at t = 150, 200 and 250 Myrs.

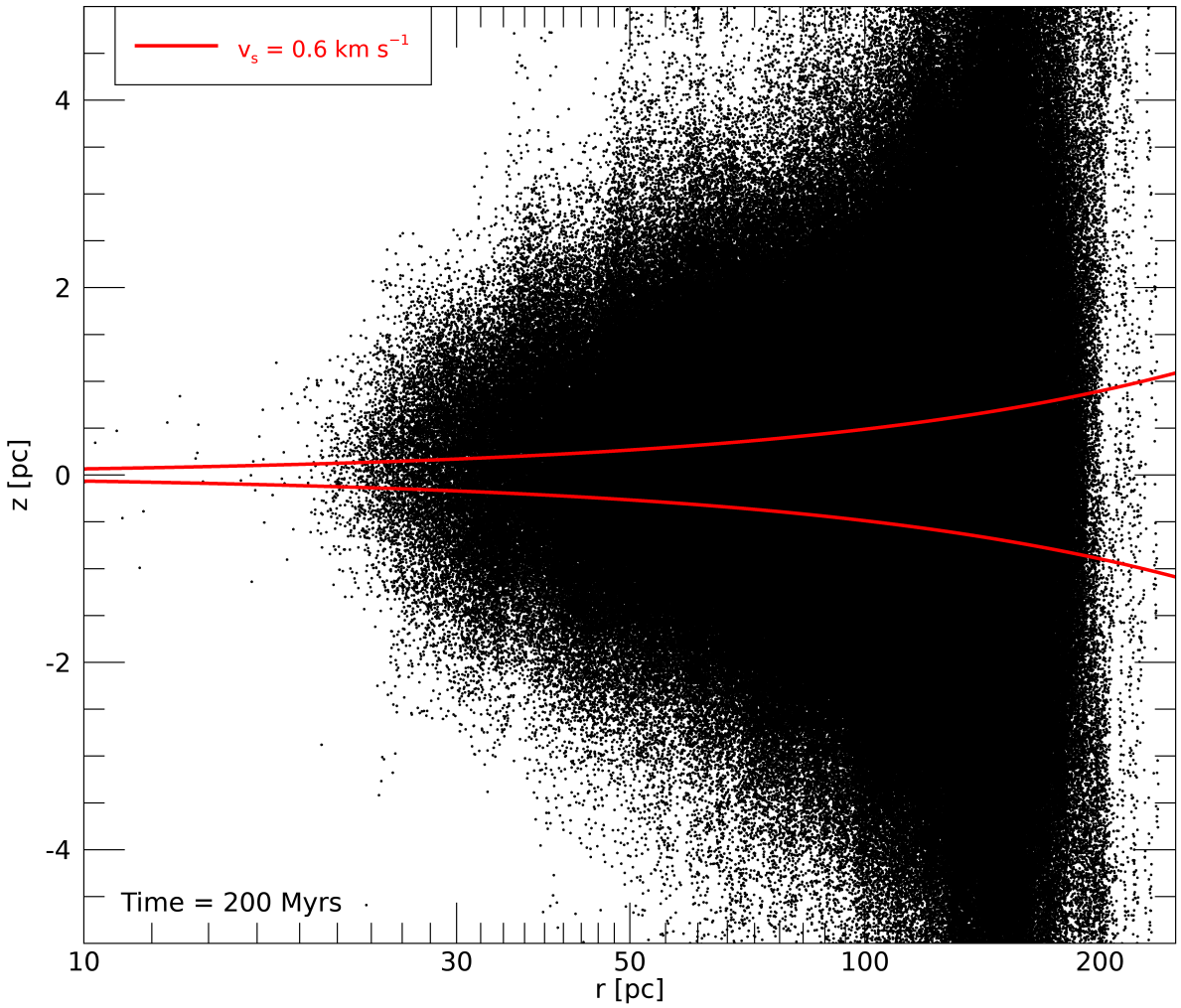

Figure 2.10: Particle position plot z vs. r of the simulation with turbulence at t = 200 Myrs. The red lines indicate the scale height value $H = c_s/\Omega$, where c_s is the sound speed, and Ω is the angular velocity due to the gravitational potential. Owing to turbulence, the disk is about 10 times thicker than the theoretical value of H.

of ν_{min} is roughly a factor of 2 higher than the value $\nu_{turb} \approx 4 \times 10^{23}$ cm^2/s calculated from my simulations. This result is consistent with the findings by Sormani et al. (2018), where they found that the viscosity used in their simulations of galactic nuclear rings, $\nu = 3 \times 10^{24}$ cm^2/s (which was sufficient to significantly affect the morphology of their simulated rings) was a factor of ~ 10 smaller than the corresponding minimum viscosity for nuclear rings, $\nu_{min} = 8 \times 10^{25}$ cm^2/s (for a $R = 1$ kpc ring). Thus, my results support Sormani et al. (2018) conclusion that viscosity may be more effective in influencing the dynamics of gaseous systems than implied by generic estimates such as the one described above.

I note that my viscosity calculations are only approximations, since the values of $\dot{M}$, Σ, and the thickness of the disk, vary over radius and time. Thus, the viscosity induced by my turbulence method will also vary with radius and time. A more careful analysis of the turbulent viscosity imposed by my driving method is reserved for a future investigation.

2.7 Summary and Discussion

Supersonic turbulence occurs over a wide range of length scales in the interstellar medium, especially within molecular clouds. The importance of turbulence in modulating star formation in the interstellar medium was further highlighted recently by a combination of numerical and analytical studies (e.g., Krumholz & McKee, 2005; Burkhart, 2018). It has also been suggested that turbulence plays a key role in forming the very first star-clusters and perhaps even globular cluster progenitors (e.g., Naoz & Narayan, 2014; Chiou et al., 2019). Furthermore, turbulence in the centers of galaxies, particularly in my own CMZ, seems to greatly influence its thermal structure and star formation rate (e.g., Kruijssen et al., 2014).

Numerical simulations have shown that turbulence decays quickly, within a few dynamical timescales (e.g., Stone et al., 1998; Mac Low, 1999). Thus, in order to properly study the dynamics of the CMZ environment with numerical simulations, it is necessary to include a mechanism for turbulence driving. Typically, simulating turbulence in gas on galactic scales

is achieved by modelling star formation and feedback. However, I note that despite the high densities and the large amount of available gas, there is about an order of magnitude less active star formation in the CMZ than might be expected from the quantity and surface density of molecular gas (e.g., Longmore et al., 2013; Kruijssen et al., 2014). Therefore, other physical processes may supplement this methodology to explain the high-velocity dispersions observed in the CMZ.

This prompted me to develop a more general mechanism for driving turbulence. Consequently, I adapted the Fourier forcing module described by Mac Low (1999) in order to simulate not just the CMZ, but this method can be applied in general to gas that orbits under the influence of a gravitational potential. I implemented this turbulence method to the SPH code Gadget2.

Rather than depending on a single grid of turbulence, as is typical with this method, I create instead many turbulent grids and use them to fill the volume of a larger simulation box. I then use trilinear interpolation to calculate and add a velocity kick to each SPH particle. The amplitude of these velocity increments is adjusted every injection time to maintain a constant energy input. As shown in Section 2.6, discontinuities in the added velocity field to the interfaces between grids are indistinguishable in the simulations.

Using a simplistic model of the CMZ consisting of a collection of Giant Molecular Clouds, my turbulence driving method allows me to study the dynamics of the gas and turbulence over long timescales. One of the main results in my simulations is that turbulence induces inward migration of gas, a result that is consistent with previous numerical simulations (e.g., Hobbs et al., 2011).

This chapter focuses on testing this new method in the context of a single physical scenario. However, my turbulence module is flexible and can be applied to study different physical scales. There are a number of parameters that can be adjusted:

- Power spectrum index: For incompressible turbulence, the Kolmogorov power spectrum in three dimensions is $\propto k^{-11/3}$ (Kolmogorov, 1941) (for a two-dimensional distribution, $P \propto k^{-8/3}$). For compressible turbulence, the power law index has been shown to be slightly steeper (e.g., Clark et al., 2011). Milky Way observations have found power law slopes of -2.8 to -3.2 in 2D maps (Elmegreen & Scalo, 2004a, and references therein). In my tests I used a power spectrum index of -4, but the power spectrum index can be modified to match observations in order to create more applicable simulations.

- The number of distinct realizations of turbulence grids: in order to avoid coherence in scales larger than L_{cube}, each of the turbulence grids has a different realization of velocity fields, drawn randomly from a library of 10 realizations. This library can be expanded with more realizations, which could potentially improve the "randomness" of the turbulence. However, this library will be limited by the memory constraints of the computing resources.

- The size of the turbulence grids (L_{cube}): in my code, this parameter also represents the largest scales on which turbulence is injected. Thus, modifying this allows flexibility in studying different turbulence injection scales depending on the physical environments to be simulated. For example, in Salas et al. (2020), I use my driving method to study how turbulence affects the formation of galactic nuclear rings. There, I discuss galactic scale ($L_{global} = 4$ kpc) simulations using larger grids of turbulence ($L_{cube} = 64$ pc).

- The number of turbulence grids per side: modifying this parameter (in tandem with the previous one, L_{cube}), allows for adjusting the size of the overall simulation domain, L_{global}.

- The total energy of injection, ΔE_{in}, and time interval between injections, N_t: these parameters need to be tuned depending on the physical environment to be simulated. In Section 2.9 I vary these parameters in order to find the optimal values to use.

However, different gas configurations will require different parameters than the ones used here. For example, I expect that smaller values of ΔE_{in} and larger values of N_t may be sufficient to balance self-gravity in lower density gas.

Software: Figure 2.2, 2.3 and 2.4 were done using the SPH visualization software `SPLASH` (Price, 2007). I used Gadget2 (Springel, 2005) to build my turbulence method. The version of the code that includes my turbulence routine can be found in my online repository: https://github.com/jesusms007/turbulence.

2.8 Appendix: Constant energy input rate

In this Section I derive Equation 2.11.

My algorithm adds a velocity "kick" to each particle every N_t timesteps while maintaining a constant energy input rate $\dot{E_{in}} = \Delta E_{in}/(N_t \Delta t)$, where Δt is the simulation timestep (fixed to be equal to 1000 yrs), and:

$$\Delta E_{in} = E_2 - E_1 = \frac{1}{2} m_p \sum_{i=1}^{N_{sph}} \vec{v_{2,i}} \cdot \vec{v_{2,i}} - \frac{1}{2} m_p \sum_{i=1}^{N_{sph}} \vec{v_{1,i}} \cdot \vec{v_{1,i}} \ , \tag{2.13}$$

where $\vec{v_{1,i}}$ is the velocity vector of a particle at time t_1 (before the kick), and

$$\vec{v_{2,i}} = \vec{v_{1,i}} + A\Delta\vec{v_i} = \vec{v_{1,i}} + A\sqrt{G\rho_i}\ \vec{I_i}(x,y,z) \tag{2.14}$$

is the velocity of the particle at time t_2 (after the kick). Therefore, $t_2 - t_1 = N_t \Delta t_s$. The function $\vec{I}(x,y,z)$ is the interpolation function that represents the turbulent velocity increment based on the particle's position (hereafter called $\vec{I}$), and A is the target variable.

Equation 2.13 then becomes:

$$\Delta E_{in} = \frac{1}{2} m_p \left[\sum_{i=1}^{N_{sph}} \left(\vec{v_{1,i}} + A\sqrt{G\rho_i}\ \vec{I_i} \right) \cdot \left(\vec{v_{1,i}} + A\sqrt{G\rho_i}\ \vec{I_i} \right) - \sum_{i=1}^{N} \vec{v_{1,i}} \cdot \vec{v_{1,i}} \right] \tag{2.15}$$

By simplifying Equation 2.15, the result is:

$$\Delta E_{in} = \frac{1}{2} m_p \sum_{i=1}^{N_{sph}} \left[A^2 G \rho_i \vec{I}_i \cdot \vec{I}_i + 2A\sqrt{G\rho_i}\ \vec{I}_i \cdot \vec{v_{1,i}} \right] \tag{2.16}$$

This equation always gives both positive and negative values for A and my code always chooses the positive value. However, to ensure that the injection of turbulence does not violate the conservation of total angular momentum of the gas, I simply multiply A by a factor of -1 or $+1$, alternating between these two factors every time the driving is performed. This ensures that, over time, the net angular momentum added to the gas particles is approximately zero while keeping the same increase in energy ΔE_{in}.

Furthermore, I change each of the 64^3 cubes of turbulence every time the driving is performed. This is to mimic the random nature of turbulence. Regardless of the source of turbulence, I expect that a parcel of gas will experience a coherent turbulent driving force during a given time interval. I can justify changing each grid every N_t timesteps if I consider that the crossing time of a parcel of gas traveling at an orbital speed of v$\approx$ 150 km s^{-1} through the average scale of a turbulence cube, i.e., $L_{ave} \approx 1$ pc, is $t_{cross} \approx 6000$ yrs. Hence, I conclude that there is little need for the velocity field to be coherent on timescales longer than 6 timesteps, thus justifying my replacement of each turbulence cube as long as N_t is more than a few.

2.9 Appendix: Dependence on turbulence parameters

Here I describe the tests I carried out to study the performance of my turbulence algorithm in order to choose N_t and ΔE_{in} values for my CMZ model. While these parameters are better represented in form of a rate, the results of this section indicate that the time interval at which the turbulence is injected affects the subsequent evolution of the gas.

I tested driving the turbulence every 1 to 5 timesteps for a total of 25 tests: for each N_t, I

used $\Delta E_{in} = 10^{46}$ to 10^{50} ergs, in a factor of 10 increments. I ran each simulation for 100 Myrs to allow the system to reach a quasi-steady state.

As a proxy for the evolution of the systems, I plot the average number density (n_{ave}) as a function of time, as shown in Figures 2.11 to 2.15. For the simulations with N_t= 2 and 3, the time evolution of n_{ave} is very similar (except for the case with ΔE_{in}= 10^{50} ergs, whose n_{ave} evolution diverges from all other runs). The average density oscillates due to the interplay between turbulence and self-gravity, potentially reaching a steady-state by $\sim$ 50 Myrs.

I also plot in Figures 2.11 to 2.15 the RMS number density (n_{RMS}) from $t = 50 - 100$ Myrs, in order to better discern differences between runs. The runs with parameter N_t= 4 and 5 show higher average densities, as expected, because in these cases, turbulence is injected less frequently, allowing gravity more time to compress the gas to higher densities. However, given their high density RMS peaks, these runs are less consistent and more chaotic than those with lower values of N_t. Also, the runs with $N_t = 5$ were only run for 50 Myrs due to the fact that the tests with $\Delta E_{in} = 10^{46}$ to 10^{48} ergs exhibited high density clumps which slowed down the computation time. These clumps originate because in those cases, the turbulence is not injected often enough to support the gas against local gravitational collapse. Particles pile on top of each other, and due to the nature of the kernel used by Gadget2, once the distance between particles approaches the smoothing length, the pressure gradient is no longer correct and the particles stick together, creating very high density clumps.

Additionally, in Figures 2.11 to 2.15, I plot the distribution of mass fraction as a function of density (density PDF) at $t = 50$ and 100 Myrs for each run. Inside a molecular cloud, the density PDF is shaped by the complex interaction between turbulence, self-gravity, magnetic fields and stellar feedback. As a result, it is an effective tool to determine the dynamical state of the gas (e.g. Federrath et al. 2010). In most of my test runs, the calculated density PDF resembles a lognormal distribution, a result that several groups have found for isothermal

gas (e.g., Vazquez-Semadeni 1994; Klessen 2000 and others). This gives me confidence that my new turbulence forcing module is consistent with previous studies of turbulence. Thus, I can fit the density PDFs to Gaussian functions of $x = \ln(n/n_0)$ with mean μ and dispersion σ:

$$f_M = C \exp\left[\frac{(x - |\mu|)^2}{\sigma^2}\right]. \tag{2.17}$$

The mass-weighted median number density (half of the mass is at densities above and below this value) is proportional to e^{μ}. I indicate this parameter with vertical bars in both figures. For each value of $N_t = 1$, 2 and 3, the value mass-weighted median number density is consistent for all energies, except $\Delta E_{in} = 10^{50}$.

Finally, it is a standard result in the literature that high-density regions are created by turbulence due to supersonic turbulent convergent flows (e.g., Elmegreen & Scalo 2004a; McKee & Ostriker 2007). The increasing values of n_{ave} with ΔE_{in} seen in Figures 2.11 to 2.14 agrees with this result.

The tests with parameter $N_t = 2$ and 3 show better consistency in the range of densities in the simulations ($n \sim 10^{3-4}$ cm^{-3}) than the other test runs. Based on their density evolution, I notice that the exact choice of of energies in this range of injection intervals has little effect on the final results. Thus I opt for the parameters $N_t = 2$ and $\Delta E_{in} = 10^{47}$ ergs as the standard choice for my CMZ model simulated in Section 2.6.

As a final note, I remind the reader that I are only testing this parameter-space of injection energies and intervals in a specific physical scenario, namely, that of a CMZ-like environment. I expect that similar choice of parameters will be useful in different environments, but further testing is needed. However, my goal here is to show that my proof-of-concept method gives consistent results and agrees with previous results in the literature. A more comprehensive analysis of the turbulence method that I introduce in this chapter is left for future work.

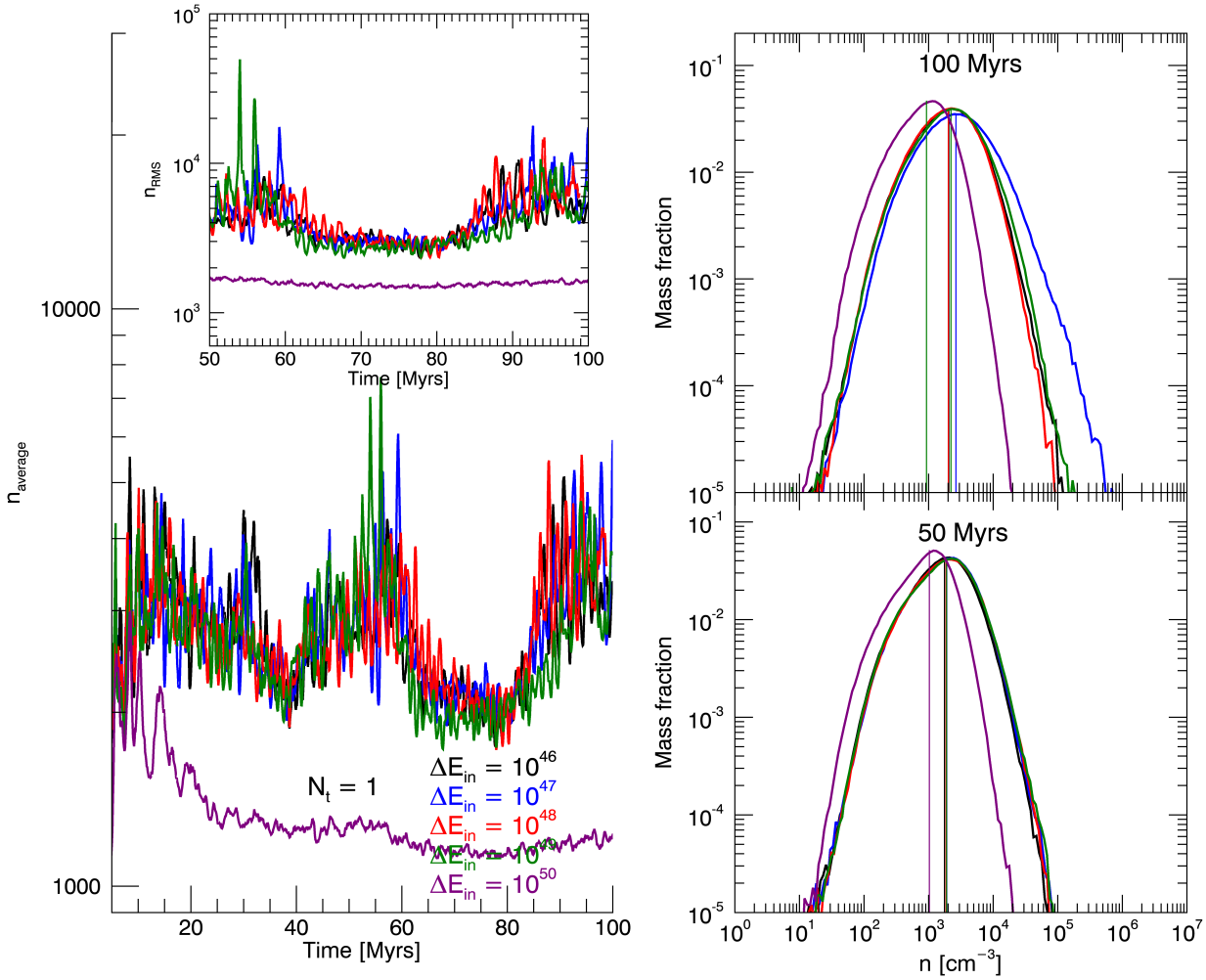

Figure 2.11: Median density, RMS density and density PDF for tests with $N_t = 1$. The mass-weighted median density is plotted with a vertical line. The density PDF is approximately lognormal.

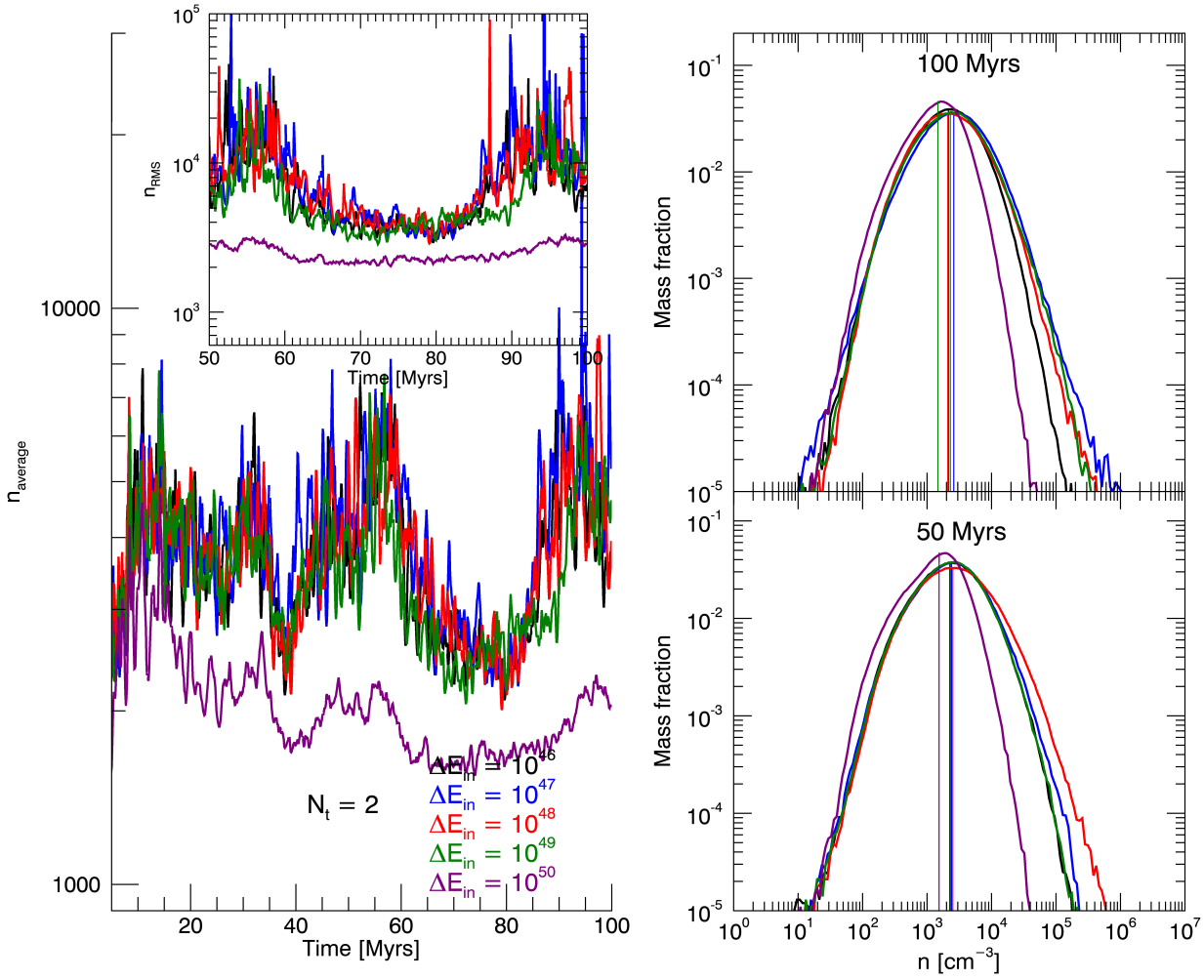

Figure 2.12: Median density, RMS density and density distribution function for tests with $N_t = 2$. The distribution is lognormal. The mass-weighted median density is plotted with a vertical line.

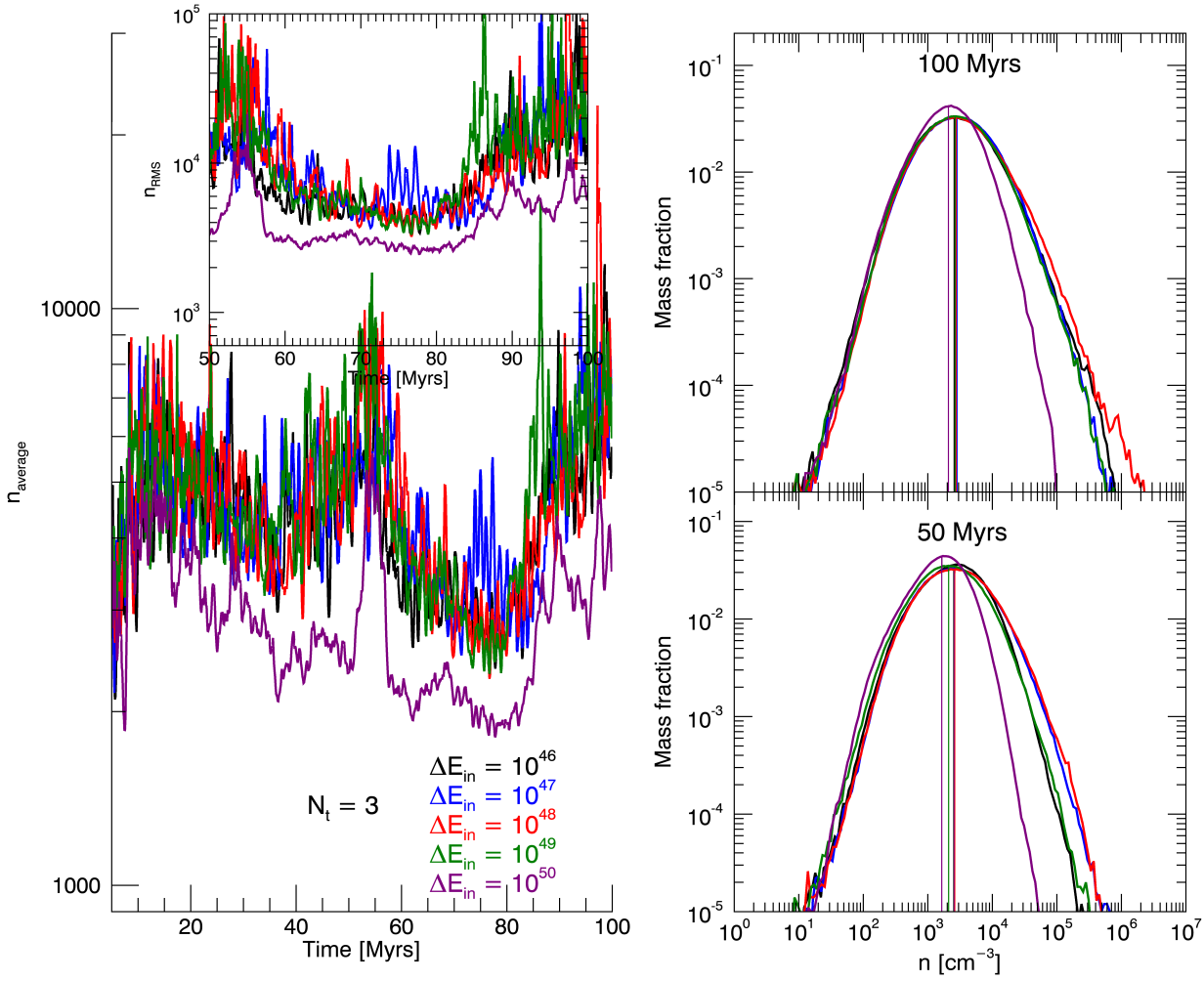

Figure 2.13: Median density, RMS density and density distribution function for tests with $N_t = 3$. The distribution is lognormal. The mass-weighted median density is plotted with a vertical line.

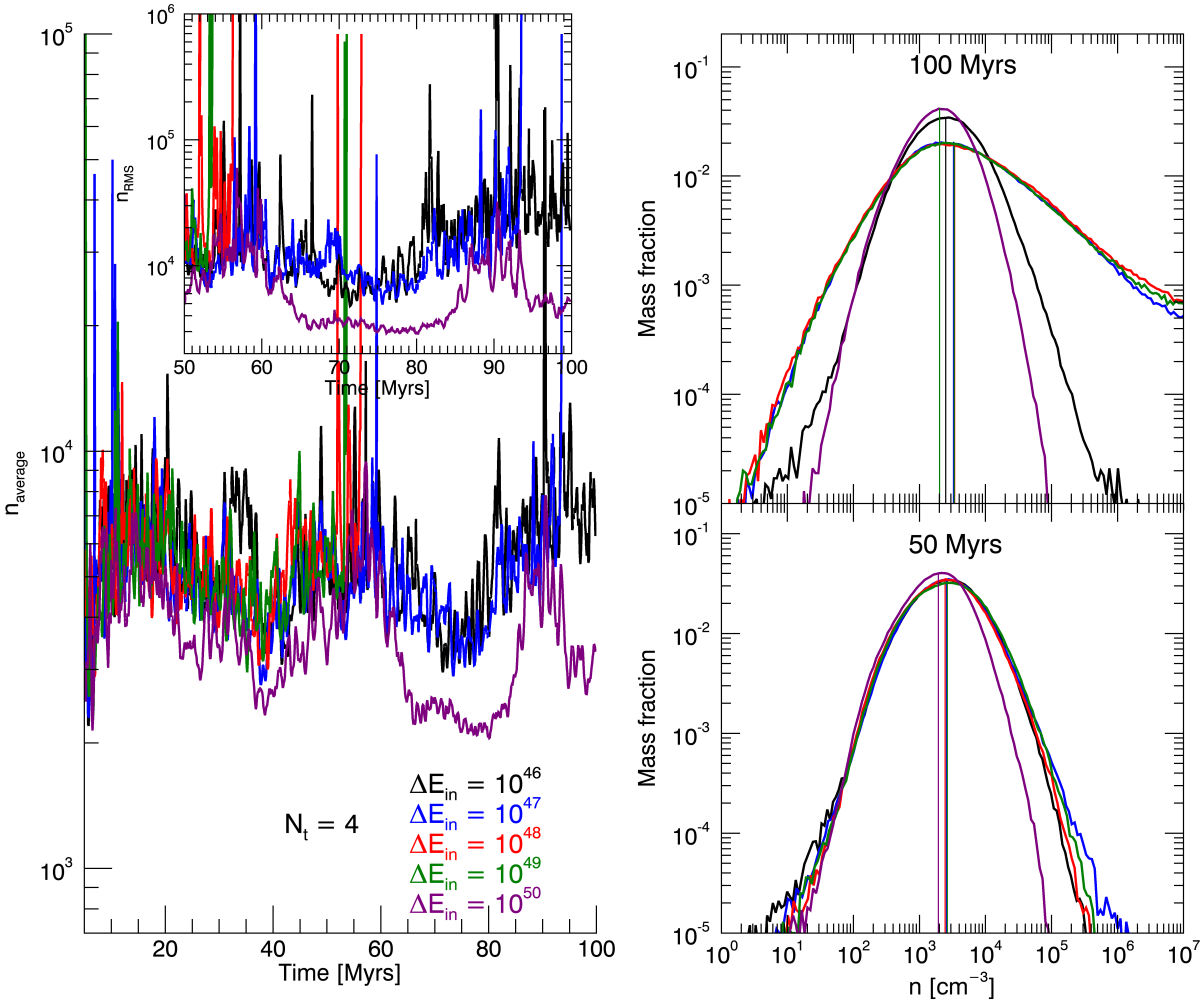

Figure 2.14: Median density, RMS density and density distribution function for tests with $N_t = 4$. The distribution is lognormal. The mass-weighted median density is plotted with a vertical line.

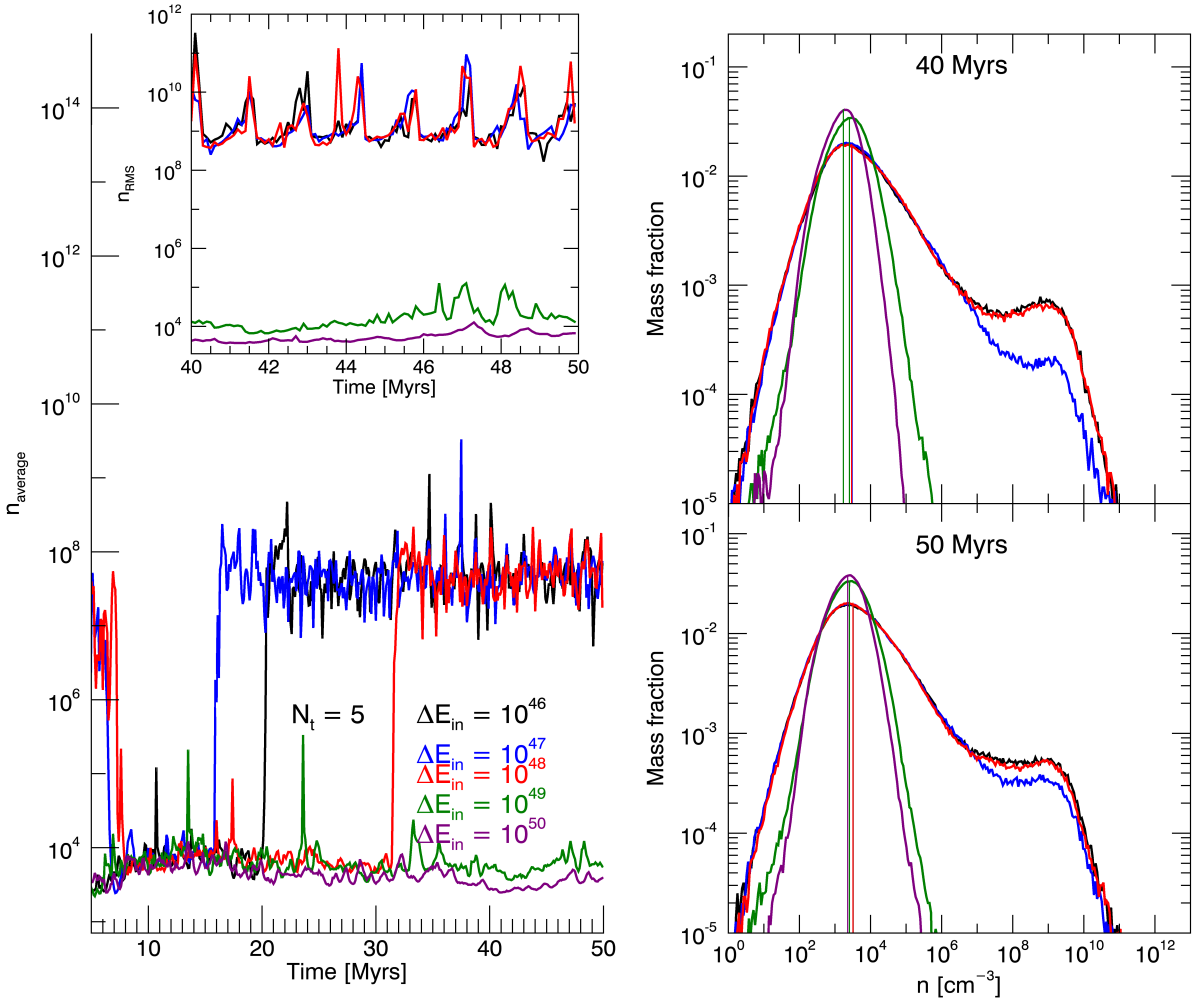

Figure 2.15: Median density, RMS density and density distribution function for tests with $N_t = 5$. The mass-weighted median density is plotted with a vertical line. These tests were run only up to 50 Myrs. The density PDF of the runs with $\Delta E_{in} = 10^{46} - 10^{48}$ ergs deviate dramatically from lognormal.

CHAPTER 3

The effects of turbulence in galactic nuclear gas rings

In this Chapter I present a summary of the paper Salas et al. (2020), which was written in collaboration with my advisors Mark R. Morris and Smadar Naoz.

3.1 Introduction

Nuclear gaseous rings are a common morphological feature of barred galaxies (e.g., Buta & Combes, 1996; Knapen, 2005; Comerón et al., 2010; Comerón, 2013; Buta, 2017b,a). Stellar bars introduce non-axisymmetric torques which produce morphological substructures in the gaseous medium, such as a pair of dust lanes at the leading side of the bar, and a nuclear gaseous ring near the center (e.g., Sanders & Huntley, 1976; Roberts et al., 1979; Athanassoula, 1992; Buta & Combes, 1996; Martini et al., 2003b,c). These nuclear rings can serve as a gas reservoir for the accretion disk that surrounds the supermassive black hole (SMBH) that is present at the centre of most galaxies.

Similarly, our Galaxy has such a ring of radius $\sim 100-150$ pc, corresponding to the densest and most massive part of the Central Molecular Zone (CMZ, Morris & Serabyn 1996; Molinari et al. 2011; Kruijssen et al. 2015; Henshaw et al. 2016). The CMZ is thought to be created and fed from the outside by the Galactic bar. According to the most widely accepted theory of galactic dynamics, the gas initially settles into X_1 orbits, which occur between the corotation radius and the inner Lindblad resonance (ILR) of the bar potential (e.g., Binney et al., 1991).

As inwardly migrating gas approaches the ILR, there is an innermost stable X_1 orbit inside of which the orbits become self-intersecting. The gas compresses and shocks near the edges of these orbits, loses angular momentum and descends onto X_2 orbits, which are closed and elongated orbits that have their long axes oriented perpendicular to the bar (Binney et al. 1991; Athanassoula 1992; Jenkins & Binney 1994; Gerhard 1996). The shocks along the innermost X_1 orbit are presumed responsible for compressing the gas into molecular form, and the accumulated molecular gas on X_2 orbits comprises the observed CMZ (e.g., Binney et al., 1991). However, it is unclear how fast molecular gas is transported further in toward the central few parsecs, and which mechanisms are responsible for its transport.

The generic dynamical description of the formation of a gaseous nuclear ring does not take into account the effects of thermal pressure. For example, Patsis & Athanassoula (2000); Kim et al. (2012); Sormani et al. (2015a) and Sormani et al. (2018), showed that, for a given underlying gravitational potential, the size and morphology of nuclear rings depend on the sound speed in the gaseous medium. Furthermore, it has been shown that the size and location of nuclear rings are also loosely related to the location of the ILR, and thus to the bar pattern speed, although the predicted location is more accurate for strongly barred potentials (e.g., Buta & Combes 1996; Sormani et al. 2015b, 2018).

Relatively high gas temperatures (70-100 K) are one of the key properties of CMZ clouds, and there is evidence showing that the gas is kept warm by the dissipation of turbulence (Immer et al., 2016; Ginsburg et al., 2016). Furthermore, the large turbulent velocity dispersion within the CMZ must be responsible for supporting the gas against gravitational collapse, since the thermal pressure of the gas would be insufficient. This motivates the need to balance the effects of self-gravity. Generally, the effects of turbulence on galactic-scale simulations have been investigated by using momentum and energy injection from supernova (SN) explosions, which are known to drive turbulence in the interstellar medium (ISM, e.g., Norman & Ferrara 1996; Mac Low & Klessen 2004; Joung & Mac Low 2006). However, I take

a different approach from previous studies by driving the turbulence via a Fourier forcing module, based on the methods by Stone et al. (1998) and Mac Low (1999). The details of this method are described in Salas et al. (2021) (Chapter 2).

Here I perform simulations of gas residing in the central few kiloparsecs of a barred galaxy, using 3D smoothed-particle hydrodynamics (SPH). My main goal is to apply my turbulence driving method to simulations of gaseous nuclear rings that include self-gravity (i.e., the mutual gravitational interactions between the SPH particles), and to compare how the effects of forced turbulence differ from the effects of thermal pressure in both low and high sound speed simulations.

3.2 Numerical Methods

In this work, I use the same gravitational potential and turbulence method described in Chapter 2. The key differences are as follows:

- I compare two different values for the bar pattern speed: a "fast" bar with $\Omega_{bar} = 63$ km s^{-1} kpc^{-1}, which has been adopted by previous studies (e.g., Kim et al., 2011; Sormani et al., 2015a; Krumholz & Kruijssen, 2015), and a "slow" bar with $\Omega_{bar} = 40$ km s^{-1} kpc^{-1}, which is the most recent estimate of the pattern speed of the Galactic bar (Bland-Hawthorn & Gerhard, 2016; Portail et al., 2017).

- I fill the volume of my simulation domain (4 kpc per side, as opposed to 512 pc in Chapter 2) with 64^3 cubic lattices, each drawn randomly from my library. Each lattice is given a physical size of 64 pc per side (as opposed to 8 pc in Chapter 2). Thus, turbulence is driven at scales from $64/2 = 32$ pc (for $k = 2$) to $64/128 = 0.5$ pc (for $k = 128$).

- No external pressure term is used.

As mentioned in the previous Chapter, my turbulence implementation contains two free parameters: ΔE_{in}, the total energy input per injection, and N_t, the number of timesteps between velocity "kicks" (the timestep is fixed in all simulations to be equal to 1000 yrs). I demonstrate that my turbulence module produces consistent results in the range $E_{turb} = 10^{46} - 10^{50}$ ergs, which corresponds to $\sim 0.01 - 100\%$ of the thermal energy of the system. I also show that N_t must be relatively low (N_t= 2-5) in order to counteract the self-gravity of the high-density gas, due to its fast free-fall time ($t_{ff} \sim 1/\sqrt{G\rho}$). In the work presented here, however, I expect the densities of my large-scale simulations to be much lower than those in Chapter 2 (Salas et al., 2021), which allows me to consider larger values for N_t.

Here, I consider two extremes, namely a "low turbulence" model and a "high turbulence" model. This is achieved by tuning the two free parameters, E_{turb} and N_t. For simplicity, I fix E_{turb} to be 10^{47} ergs, and use two values for N_t, 100 and 2, which represent the low and high turbulence models, respectively. I expect the turbulence parameters in real galactic centers to fall somewhere between these two extremes.

3.3 Initial conditions

As a proof-of-concept, I create a simplistic model of a galactic disk consisting of an outer radius of 2 kpc, an inner radius of 30 pc, and a Gaussian scale height of 50 pc. The disk contains a total mass of 10^8 $M_\odot$, with each SPH particle having a mass of 130 $M_\odot$. The particles are initially in circular orbits, with their velocities calculated using the potential described in Section 2.2.3. All simulations were run using an isothermal equation of state.

3.4 Results

I performed 4 tests with turbulence driving, using the slow and fast bar pattern speed values and the low and high turbulence parameters described in Section 3.2. The system reaches steady state by $\sim$ 150 Myrs, thus I ran simulations ran for 200 Myrs, which is long enough

Test name	Turbulence	c_s (km s^{-1})	Self gravity	Pattern speed (km s^{-1} kpc^{-1})
SBLSP	None	0.6	No	40
SBHSP	None	10	Yes	40
SBLT	Low (ΔE_{in}= 10^{47} ergs, N_t= 100)	0.6	Yes	40
SBHT	High (ΔE_{in}= 10^{47} ergs, N_t= 2)	0.6	Yes	40
FBLSP	None	0.6	No	63
FBHSP	None	10	Yes	63
FBLT	Low (ΔE_{in}= 10^{47} ergs, N_t= 100)	0.6	Yes	63
FBHT	High (ΔE_{in}= 10^{47} ergs, N_t= 2)	0.6	Yes	63

Table 3.1: Summary of all tests. SB and FB stand for "slow bar" and "fast bar", respectively. LSP and HSP stand for "low sound speed" and "high sound speed", respectively. HT and LT stand for "high turbulence" and "low turbulence", respectively. The low turbulence models correspond to injecting ΔE_{in}= 10^{47} ergs of energy every N_t= 100 timesteps, and the high turbulence models correspond to injecting ΔE_{in}= 10^{47} ergs of energy every N_t= 2 timesteps.

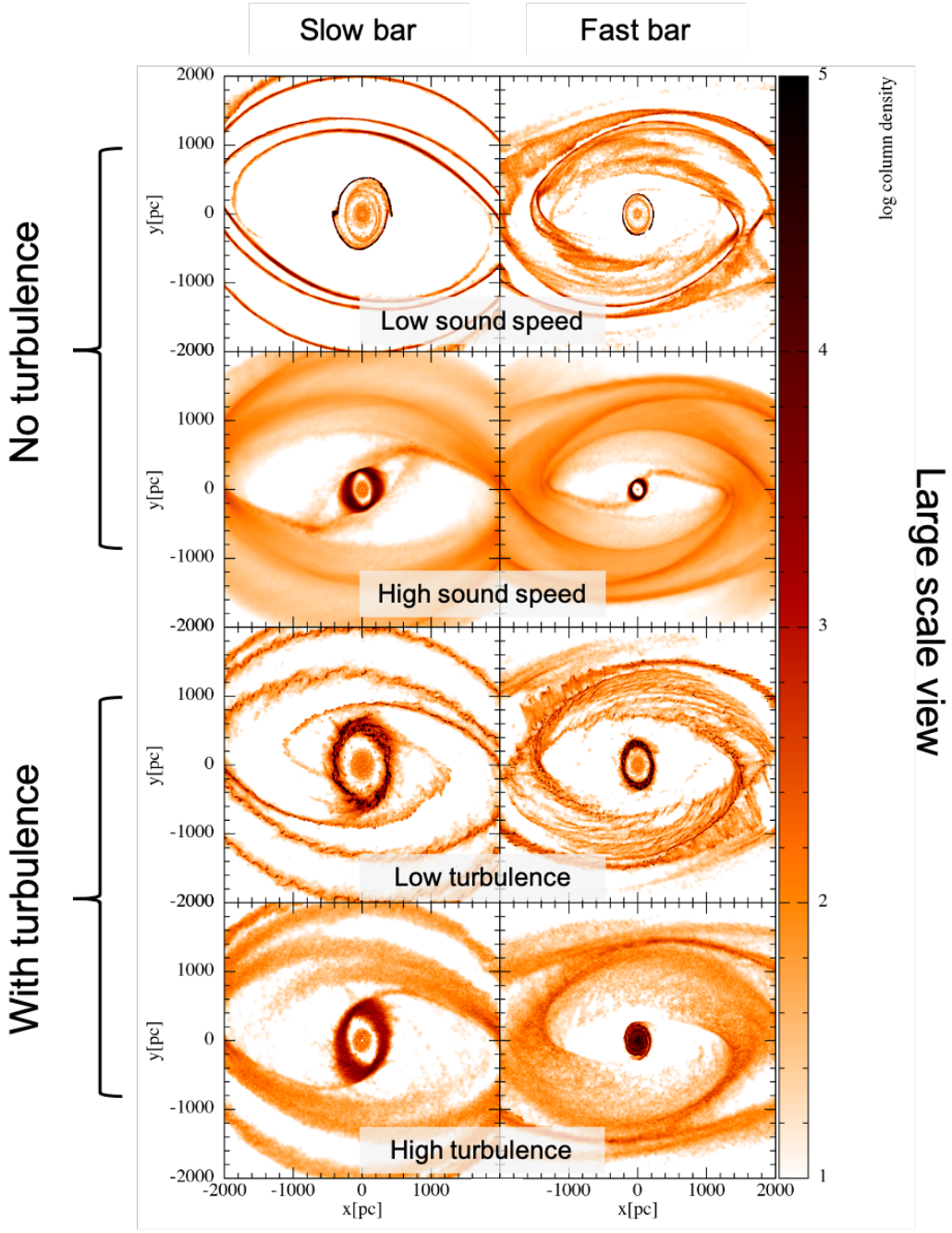

Figure 3.1: Face-on view of the simulations at t = 200 Myrs. The slow-bar model produce a bigger ring than the fast-bar model, as expected. Furthermore, the high turbulence tests make the nuclear rings more spread out (dispersed). The long axis of the bar lies along the x-axis.

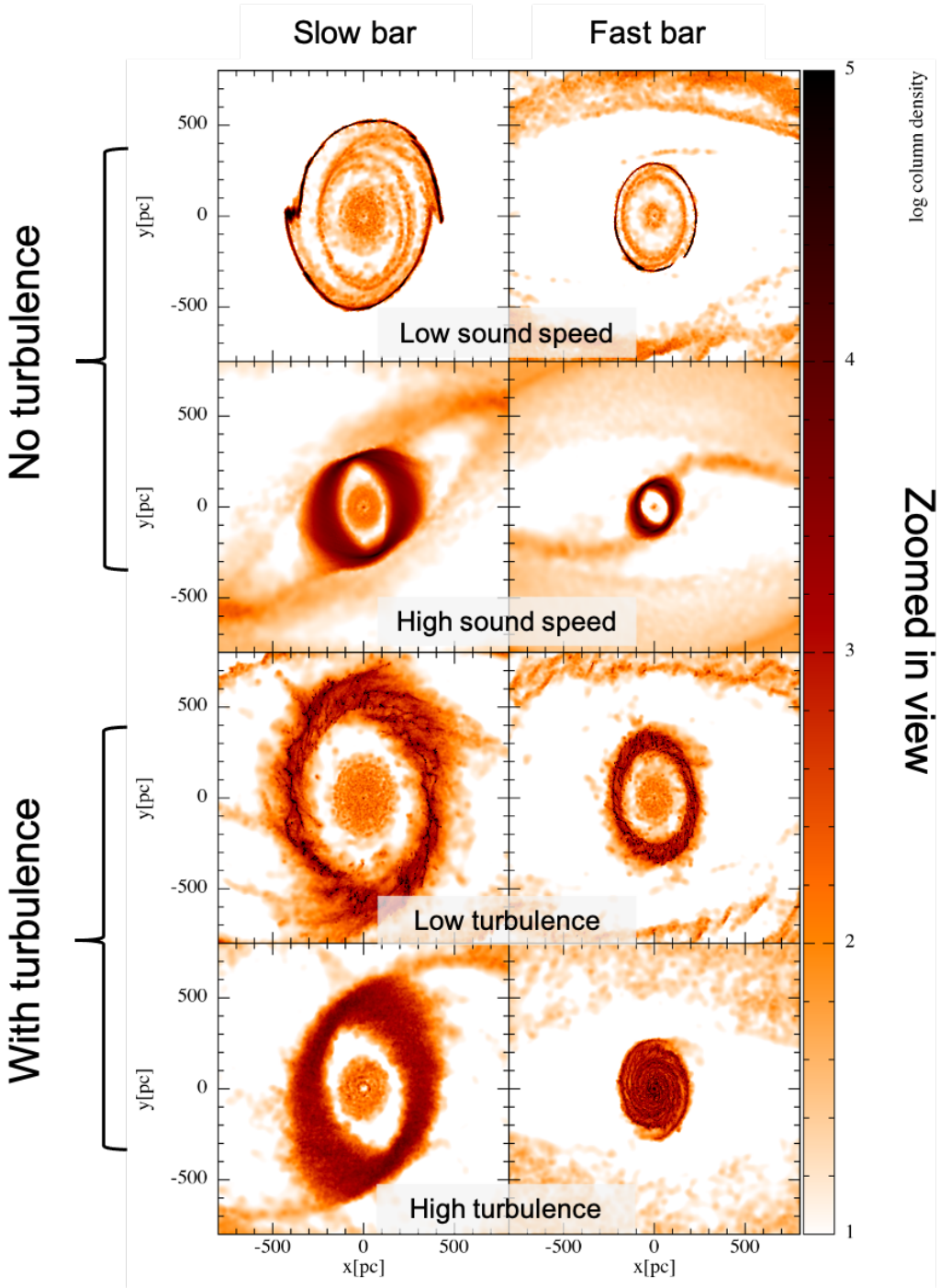

Figure 3.2: Face-on view of the simulations at t = 200 Myrs, zoomed-in to the inner 800x800 pc. The long axis of the bar lies along the x-axis.

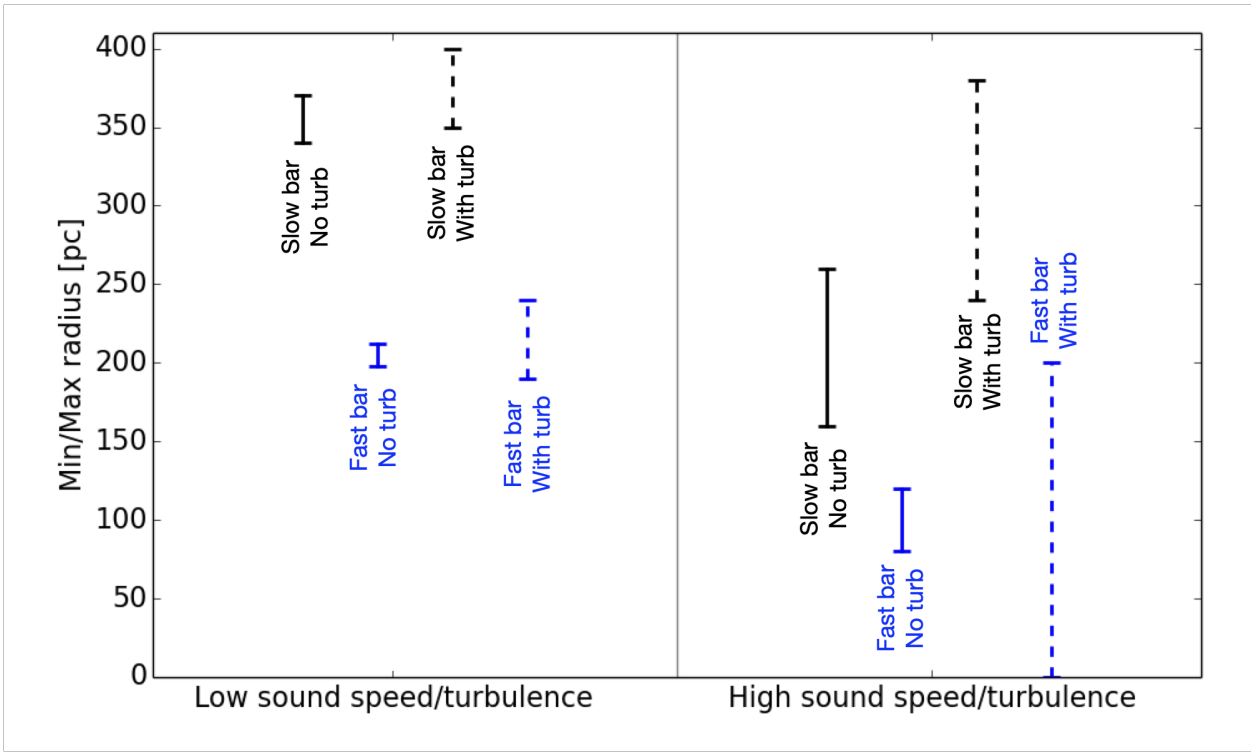

Figure 3.3: Radial thickness comparison for the nuclear rings in all 8 simulations. For each vertical radial distance line, the points (horizontal dashes) represent the minimum and maximum radial distances of the ring (along the $+x$ axis). Black lines indicate the slow bar tests, while blue lines indicate the fast bar tests. Solid lines indicate the tests without turbulence, and dashed lines indicate the tests with turbulence.

to capture the relevant dynamics, in addition to save computational time. For comparison, I also performed 4 tests with no turbulence: two of these simulations were done using a sound speed of $c_s = 0.6$ km s^{-1} (same as with the runs with turbulence. This value corresponds to a temperature of about 100 K, assuming the gas is primarily molecular), and the other two were done using a sound speed of $c_s = 10$ km s^{-1}. Each of these was also done with a slow and fast bar. Table 4.1 summarizes the parameters used in each test. The nomenclature is as follows: FB and SB correspond to "Fast Bar" and "Slow Bar", respectively. LSP and HSP correspond to "Low Sound Speed" and "High Sound Speed". Similarly, LT and HT indicate "Low Turbulence" and "High Turbulence", respectively.

3.4.1 Ring comparison

Here I investigate the morphology of the rings produced by the different bar pattern speeds and the effects of turbulence. Figure 3.1 and 3.2 show the final state of the gas at $t = 200$ Myrs for all simulations performed. In all runs, the gas accumulates on x_2 orbits, forming an elongated ring. Moreover, the smallest nuclear rings were produced by the fast bar tests, as expected, since the bar pattern speed influences the location of the nuclear ring (e.g., Sormani et al., 2015c). The size of a nuclear ring is related to the radius of the ILR (Buta & Combes, 1996; Sormani et al., 2018): increasing the pattern speed pushes the ILR inward, thus yielding a smaller ring.

For clarity, I encapsulate the size difference between the nuclear rings in Figure 3.3, where I show the spread (radial thickness, i.e., the minimum and maximum radius along the $+x$ axis) of the rings in each simulation. Black lines indicate the slow bar tests, while blue lines indicate the fast bar tests. Solid lines indicate the tests without turbulence, and dashed lines indicate the tests with turbulence.

Among the simulations without turbulence, the tests with high sound speed produce smaller nuclear rings than those with low sound speed. This effect has been explored by Kim et al.

(2012) and later by Sormani et al. (2015a, 2018), who demonstrated that nuclear rings shrink in size with increasing sound speed. In particular, Sormani et al. (2018) found that because of the high sound speed in their simulations, the thermal pressure forces are significant and lead to the development of shocks. This shocked gas is slowed down, and starts falling closer to the center than in low sound speed simulations (for more details on the effects of thermal pressure on nuclear rings, see Section 5.2 of Sormani et al. 2018).

Meanwhile, my turbulence treatment induces a more dispersed (spread out) structure to the nuclear rings compared to the runs without turbulence (especially those with low sound speed). Similarly, the high turbulence runs produce more dispersed nuclear rings than the low turbulence (and the low sound speed) runs, which was expected. Additionally, turbulence induces a more filamentary structure in gas density, compared to the more diffuse gas density in the simulations without turbulence (as was also described in Salas et al. 2021). In Figure 3.2 I show a zoom-in of the inner 800×800 pc of the simulations, where these differences can be seen more clearly.

In particular, the simulation with a fast bar and high turbulence (FBHT) produces a nuclear ring that is completely filled and smaller than in all other turbulence runs. This effect is similar to that found in the simulations by Tress et al. (2020), which demonstrated that turbulence due to SN feedback greatly influences inflow from the CMZ to the central few parsecs. my turbulence methodology (with a high turbulence energy injection, as in the FBHT test) captures these effects, which help drive gas from the nuclear ring to the inner few pc.

As mentioned in Salas et al. (2021), the spreading of the nuclear rings can be attributed to the "turbulent" viscosity induced by my driving method. Because of this viscosity, angular momentum is transferred from the inner parts of the nuclear ring to the outer parts. The inner parts of the ring lose some angular momentum and move inward, while the outer parts gain some angular momentum and move outward. The net effect is that the rings spreads

		Method 1		Method 2		
Test name	M_{ring} ($x10^7$ $M_\odot$)	Ring thickness H (pc)	$\nu_{turb} = c_s H$ (cm^2/s)	$\dot{M}_{average}$ ($M_\odot$/yr)	$\Sigma_{average}$ ($M_\odot/pc^2$)	$\nu_{turb} = \dot{M}/3\pi\Sigma$ (cm^2/s)
SBLT	4.7	80	$1.5x10^{25}$	0.05	60	$2.6x10^{25}$
SBHT	4.6	100	$2x10^{25}$	0.03	80	$1.2x10^{25}$
FBLT	1.0	20	$4x10^{24}$	0.001	50	$6.4x10^{23}$
FBHT	1.4	30	$6x10^{24}$	0.006	100	$2x10^{24}$

Table 3.2: Tabulated values used to calculate the turbulent viscosity, ν_{turb}, for each of the runs with turbulence.

(e.g., Shakura & Sunyaev, 1973; Lynden-Bell & Pringle, 1974; Pringle, 1981). I estimate the turbulent viscosity induced by my driving method below.

3.4.2 Turbulent viscosity

As I showed in Salas et al. (2021), I can approximate the viscosity induced by my driving module using the concept of α-viscosity (Shakura & Sunyaev, 1973; Pringle, 1981). First, I use the standard definition:

$$\nu_{turb} = \alpha_\nu c_s H \tag{3.1}$$

where $\alpha_\nu \leq 1$ is a parameter that adjusts the strength of the viscosity, and H is the vertical thickness (scale height) of the nuclear ring. I estimate H and calculate ν_{turb} for each ring in the simulations with turbulence (assuming $\alpha_\nu = 1$), and present them in Table 3.2, shown under the label "Method 1". I note that the nuclear rings in the "slow bar" (SB) tests are vertically thicker (larger H) than the "fast bar" (FB) tests, thus leading to higher values of ν_{turb}. This can be explained by the fact that a slower bar pattern speed creates bigger rings, which contain more mass (which I also indicate in Table 3.2, shown as M_{ring}), and thus receive a larger fraction of the injected turbulent energy than the smaller rings.

Alternatively, I can estimate ν_{turb} by using the mass accretion rate due to α-viscosity

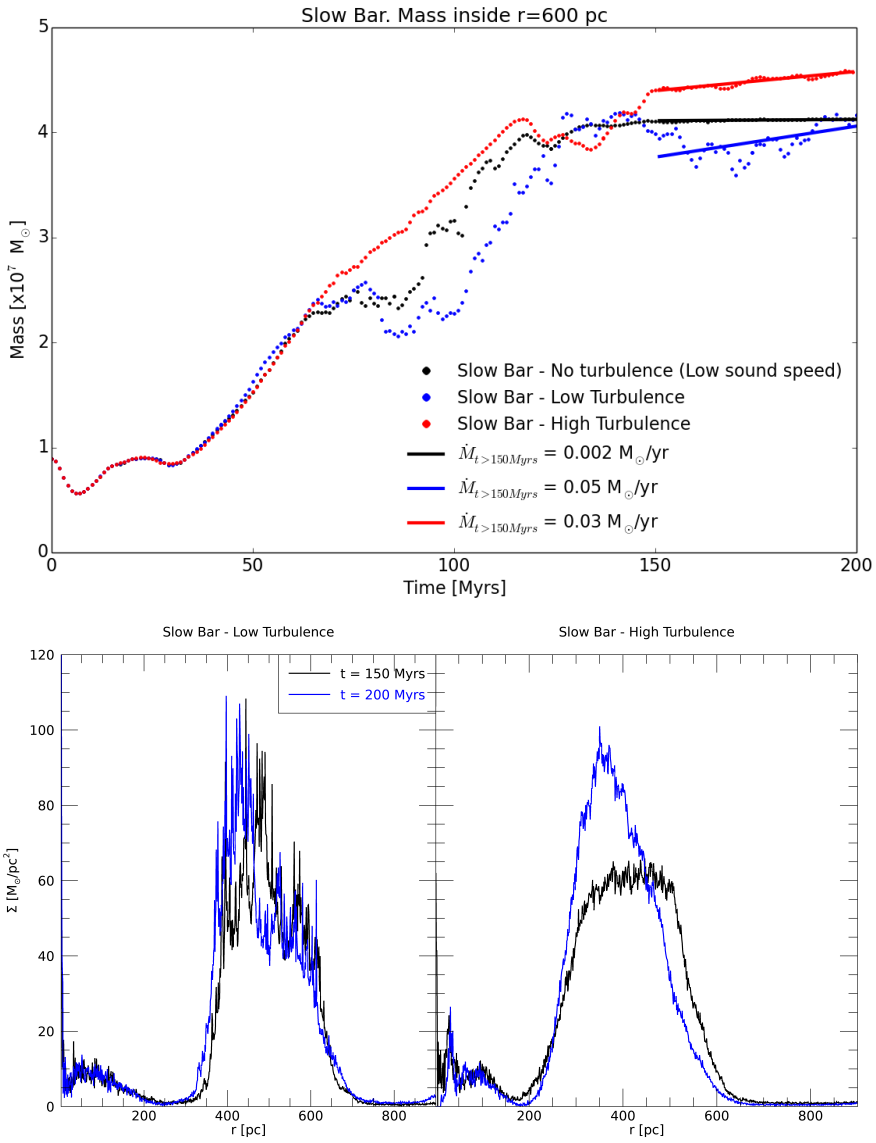

Figure 3.4: Top: mass inside a radius of $r = 600$ pc as a function of time. The black points represent the slow bar, no turbulence simulation (SBLSP). Similarly, the blue and red points represent the low turbulence (SBLT) and high turbulence (SBHT) simulations, respectively. I approximate the mass evolution after 150 Myrs as a straight line, and compute the slope, $\dot{M}$. Bottom: plots of surface density (Σ) versus radius for the SBLT (bottom left) and SBHT (bottom right) simulations. The black and blue lines correspond to $t = 150$ and 200 Myrs, respectively.

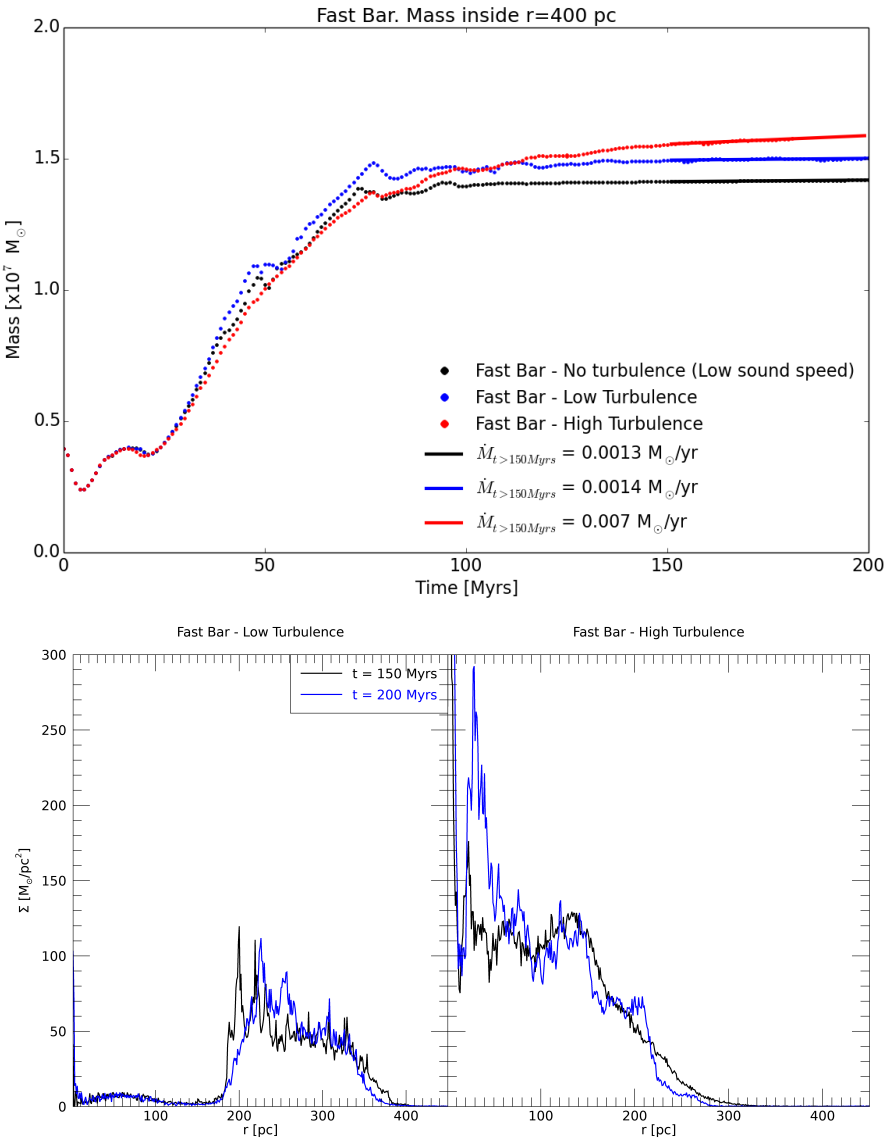

Figure 3.5: Top: mass inside a radius of $r = 400$ pc as a function of time. The black points represent the fast bar, no turbulence simulation (FBLSP). Similarly, the blue and red points represent the low turbulence (FBLT) and high turbulence (FBHT) simulations, respectively. I approximate the mass evolution after 150 Myrs as a straight line, and compute the slope, $\dot{M}$. Bottom: plots of surface density (Σ) versus radius for the FBLT (bottom left) and FBHT (bottom right) simulations. The black and blue lines correspond to $t = 150$ and 200 Myrs, respectively.

(Shakura & Sunyaev, 1973; Pringle, 1981):

$$\nu_{turb} = \frac{\dot{M}}{3\pi\Sigma} \tag{3.2}$$

where $\dot{M}$ is the mass accretion rate and Σ is the surface density.

To determine $\dot{M}$, I show in the top panel of Figure 3.4 the mass inside a radius of $r = 600$ pc (which is a radius large enough to contain the nuclear rings) of the slow-bar simulations with turbulence (low turbulence indicated in blue, high turbulence indicated in red). I consider only the time after 150 Myrs, i.e., after the gas has settled into $x1$ and $x2$ orbits and reached a steady state, and fit the slopes as straight lines. I find an average mass inflow rate of $\dot{M} = 0.05$ $M_\odot$/yr for the low turbulence run, and $\dot{M} = 0.03$ $M_\odot$/yr for the high turbulence run. I also tabulate these results in Table 3.2. For comparison, I also show in the top panel of Figure 3.4 the corresponding values for the low sound speed, no turbulence run.

To calculate Σ, I plot in the bottom panel of Figure 3.4 the surface density vs radius at 150 Myrs and 200 Myrs of the slow bar simulations with turbulence. I used the midpoint radius to calculate the average of both times, which is $r = 500$ pc for the slow bar, low turbulence run (left panel of Figure 3.4), and $r = 400$ pc for the slow bar, high turbulence run (right panel of Figure 3.4). The average values for the surface density at those radii for both runs are $\Sigma = 60 M_\odot/pc^2$ and $\Sigma = 80$ $M_\odot/pc^2$, respectively. Thus, using Equation 3.2, I compute ν_{turb} for both slow bar simulations with turbulence and present them in Table 3.2, under the label "Method 2". Thus, I find that, for the slow bar (SB) simulations, the calculated values of ν_{turb} using Equations 3.1 and 3.2 (i.e., Methods 1 and 2) differ by less than a factor of two.

Similarly, Figure 3.5 illustrates the same analysis as described for Figure 3.4, except for the fast bar simulations. However, to estimate $\dot{M}$, I consider in this case the mass inside a radius $r = 400$ pc (enough to contain the smaller nuclear rings). Also, to calculate Σ, I use the average of both 150 and 200 Myrs at $r = 300$ pc for the fast bar, low turbulence run (left

panel of Figure 3.5) and $r = 100$ pc for the fast bar, high turbulence run (right panel of Figure 3.5). I estimate the values of $\dot{M}$, Σ and ν_{turb} and present them in Table 3.2. I find that the calculated values of ν_{turb} using Equations 3.1 and 3.2 (i.e., Methods 1 and 2) to be different by about a factor of three in the case of the fast bar, high turbulence (FBHT) simulation. In the case of the fast bar, low turbulence (FBLT) simulation, the values of ν_{turb} differ by about a factor of 10. This can be explained by the fact that, as noted above, because the resulting nuclear ring in a fast bar simulation is relatively small, it receives a smaller fraction of the injected turbulent energy. This fact, combined with an already low turbulent injection rate (as is the case in the FBLT run), seems to not contribute significantly to the mass inflow compared to the fast bar simulation without turbulence (FBLSP, see the top panel of Figure 3.5).

To compare my calculated values of ν_{turb} to estimates of the viscosity derived from the characteristics of entire galaxies, I use the estimate from Lynden-Bell & Pringle (1974):

$$\nu = \frac{1}{3} c \frac{a}{f} \ , \tag{3.3}$$

where c is the velocity dispersion, a is a typical molecular cloud size, and f is the filling fraction. Using the values $c = 8$ km/s, $a = 10$ pc and $f = 0.1$, Lynden-Bell & Pringle (1974) estimated a turbulent viscosity of $\nu = 8 \times 10^{25}$ cm^2/s. The values of ν_{turb} I present in Table 3.2 are in good agreement with this estimation, especially for the slow bar simulations.

Finally, the effects of viscosity on nuclear gaseous rings were explored also by Sormani et al. (2018), who found that nuclear rings spread over time, as expected. I find qualitative similarities between their simulations and mine, especially for those with low turbulence (cf. figure 7 in Sormani et al. 2018). However, I emphasize that unlike standard viscosity treatments, my turbulence method is capable of not only inducing an effective viscosity, but also producing the typical filamentary density structures that should be expected in the presence of turbulence.

3.5 Summary and conclusion

As suggested by Sormani et al. 2019 (and references therein), the sizes of nuclear rings are generally controlled by: 1) the strength of the galactic bar, 2) the bar pattern speed, and 3) the sound speed. In this work, I explore the inclusion of turbulence, and compare it to the effects of thermal pressure due to low and high sound speeds (i.e., temperatures) in the absence of turbulence. I find that turbulence has the effect of spreading out nuclear rings, as well as promoting mass inflow to the center. Both of these effects are due to the viscosity generated by turbulence, as explored in Salas et al. (2021).

The qualitative differences between the runs with and without turbulence are apparent in Figures 3.1 and 3.2. My turbulence treatment creates smaller and more dispersed rings than the low sound speed, no-turbulence tests. The creation of smaller rings was previously shown to depend on the speed of sound (e.g., Kim et al., 2012; Sormani et al., 2015a, 2018). In particular, the nuclear rings shrink in size with increasing sound speed and viscosity. My turbulence method creates a turbulent viscosity, which has been shown to promote the transfer of angular momentum and enhance the rate of inward migration (Wang et al., 2009; Hobbs et al., 2011), thus creating a smaller and more dispersed ring.

This is especially true for the fast bar, high turbulence (FBHT) simulation, which has a ring that is completely filled in. This occurs because of the large turbulence injection rate in combination with a fast bar pattern speed. This is consistent with prior work showing that turbulence enhances inflow rates towards supermassive black holes (SMBHs). In particular, simulations by Tress et al. (2020) showed that SN feedback drives gas from the CMZ into the Circumnuclear Disk located in the central few parsecs. This is because stellar feedback associated with episodes of star formation activity in the CMZ can stochastically launch parcels of gas towards the center (e.g., Davies et al. 2007). Other authors have suggested that SN feedback and supersonic turbulence inside accretion disks (e.g., Wang et al. 2009) can promote accretion onto SMBHs by enhancing angular momentum transfer (e.g., Collin

& Zahn 2008; Chen et al. 2009; Palouš et al. 2020a). This effect was confirmed also by **?**, which used the turbulence algorithm presented here to study the effects of turbulence on the evolution of the CND, and among their results, found that my turbulence method enhances accretion rates from the CND toward the central black hole.

Finally, it is worth noting that the ring produced by the FBHT test is similar, in terms of shape and mass, to that of Kim et al. (2011) (cf. their figure 1). This is not entirely surprising since my FBHT simulation uses the same gravitational potential, the same value for the bar pattern speed, and same initial mass of the large-scale disk as in their study. The main difference between the two simulations is the mechanism for turbulence driving. Kim et al. (2011) used a model of stellar feedback in which SN are simulated by injecting thermal energy into surrounding SPH particles. My turbulence module injects kinetic energy in the form of a velocity field with a k^{-4} power spectrum to all particles. This comparison shows that my turbulence driving method is comparable to standard methods of SN feedback in driving turbulence. However, turbulence in the Galaxy, and particularly in the CMZ, does not necessarily come only from SN feedback. In fact, the dominant source of turbulence in the CMZ has not been yet conclusively identified (Kruijssen et al., 2014). Turbulence is produced by the interplay of many sources: SN blasts, gas instabilities, stellar winds, magnetic fields which produce hydromagnetic waves and MHD instabilities, etc., all which work in different scales and combine to create a turbulence spectrum that has been reported in the literature to approximately obey a power law (e.g., Elmegreen & Scalo, 2004b). Hence, the turbulence injection mechanism used here can account for many sources of turbulence within the adopted range of scales.

Due to computational constraints, in this work I focused only on a limited range of injection scales, as well as two limiting cases for the strength of the turbulence injection. A more heuristic exploration of the turbulence parameters and turbulence scales, in combination with a more refined gravitational potential of the inner Galaxy, would be of value for constructing

improved models that can be compared directly and statistically with the observed density and velocity dispersions in the CMZ. Furthermore, the turbulence method described here can be adapted to other SPH and grid codes, some of which could offer more elaborate techniques to capture the physics of the CMZ more accurately. Thus, the results presented here indicate that my turbulence driving module is a promising way to model turbulence in this complex environment.

CHAPTER 4

The effects of turbulence in the circumnuclear disk

In this Chapter I present a summary of the paper Dinh et al. (2021), which was done in collaboration with UCLA undergraduate student Cuc K. Dinh. I was her primary research mentor from August 2019 to January 2021.

4.1 Introduction

The Galactic Center (GC) is a vibrantly active region hosting a 4×10^6 $M_\odot$ supermassive black hole, manifested as the radio source Sgr A* (e.g., Ghez et al., 2008). The black hole is orbited by a molecular gas structure known as the Circumnuclear Disk (CND, Becklin et al. 1982; Morris & Serabyn 1996). This moderately dense ($10^4 - 10^6$ cm^{-3}) and massive (few 10^4 $M_\odot$) disk has an inner radius of ~ 1.5 pc and a spatially variable outer radius of 3-7 pc (Serabyn et al., 1986; Sutton et al., 1990; Morris & Serabyn, 1996; Oka et al., 2011; Etxaluze et al., 2011). It is also relatively warm, with a temperature of a few hundred Kelvin (e.g. Genzel et al., 1985; Güsten et al., 1987; Genzel, 1989; Jackson et al., 1993; Morris & Serabyn, 1996; Bradford et al., 2005; Requena-Torres et al., 2012; Lau et al., 2013; Mills et al., 2013), and a smaller amount of gas exceeding 500 K (Mills et al., 2017).

Numerous observational studies have identified various structural components of the CND. For example, Martín et al. (2012) detail three kinematically distinct molecular structures having separate inclinations and peak rotation velocities. Other features that have been

described include lobes, extensions, arcs, streamers and arms (e.g., Güsten et al., 1987; Sanders, 1998; Christopher et al., 2005; Montero-Castaño et al., 2009; Hsieh et al., 2017). Density clumps are also frequently mentioned in the literature, though their definition varies depending on the study (e.g., Güsten et al., 1987; Sutton et al., 1990; Jackson et al., 1993; Marr et al., 1993; Shukla et al., 2004; Christopher et al., 2005; Montero-Castaño et al., 2009; Martín et al., 2012; Lau et al., 2013; Smith & Wardle, 2014).

At present, the origin of the CND remains an open question; some studies argue that this disk is a transient structure, while others suggest that it is quasi-stable and long-lived. The transient argument is largely based on the disk's non-uniformity: the presence of clumps and streams (e.g., Genzel et al. 1985; Christopher et al. 2005; Montero-Castaño et al. 2009; Martín et al. 2012; Lau et al. 2013). Because the rotational dynamics of the disk are dominated almost entirely by the central black hole, the disk should experience strong differential rotation that smooths out non-uniformities such as clumps on an orbital time scale. The observed non-axisymmetric density distribution has therefore been invoked as evidence that either the CND was recently formed, and that the observed structure is therefore short-lived (e.g., Güsten et al., 1987; Requena-Torres et al., 2012), or that the structures within the disk are dense enough to be tidally stable (Jackson et al., 1993; Vollmer & Duschl, 2001b,a; Shukla et al., 2004; Christopher et al., 2005; Montero-Castaño et al., 2009). However, multiple studies have found that the clumps have densities ranging up to a few times $\sim 10^5$ cm^{-3}, which falls well below the critical Roche density of $\sim 3 \times 10^7$cm^{-3} (e.g., Güsten et al. 1987; Requena-Torres et al. 2012; Lau et al. 2013; Mills et al. 2013). Thus, the observed density concentrations are tidally unstable, which has led some to conclude that the CND is a transient structure, with a lifetime of a few dynamical timescales ($\sim 10^4$-10^5 yrs, Güsten et al. 1987). A popular model to account for the transient structures within the CND is that a passing cloud was gravitationally captured by the black hole. This "infalling cloud" was then tidally disrupted into what is now the CND (Sanders, 1998; Bradford et al., 2005; Bonnell & Rice, 2008; Wardle & Yusef-Zadeh, 2008; Hobbs & Nayakshin, 2009; Alig et al., 2011; Oka

et al., 2011; Mapelli et al., 2012; Mapelli & Trani, 2016; Trani et al., 2018; Goicoechea et al., 2018; Ballone et al., 2019).

The long-term evolution of the CND is therefore the question before us. Are we seeing it soon after it has been created, and will it persist as a quasi-stable structure well into the future, or will it be dissipated by various forms of energetic activity at the Galactic center?

An important factor to consider when addressing these questions is that the CND is subject to various sources of turbulence, which come from the active environment of the Galactic Center. These can be in the form of supernovae (e.g., Mezger et al. 1989; Martín et al. 2012), outflows from the Nuclear Stellar Cluster (e.g., Morris & Serabyn 1996; Genzel et al. 2010) and Sgr A*, and turbulence due to the CND's toroidal magnetic field, which has a strength on the order of a few milligauss (e.g., Marshall et al. 1995; Bradford et al. 2005; Hsieh et al. 2018). These perturbers may play a vital role in the CND's morphology. However, the general effect of turbulence driving on the disk's structural evolution is still largely uncertain.

In Dinh et al. (2021), we performed 3D smoothed particle hydrodynamic (SPH) simulations that include self-gravity and my turbulence driving method to investigate how different scales of turbulence affect the CND's dynamical evolution. Our aim was to determine whether turbulence can help us distinguish between the transient and non-transient ideas.

4.2 Numerical Methods

In order to simulate the CND, I included into Gadget2 the gravitational potential of the inner 10 pc of the Galaxy. Furthermore, I added the effects of pressure by a surrounding medium in a manner identical to Section 2.2.2.

4.2.1 Gravitational potential

I include into Gadget2 the gravitational potential of the inner 10 pc of the Galaxy, which includes the supermassive black hole (Sgr A*) and the Nuclear Stellar Cluster (NSC, e.g., Do et al. 2009; Schödel et al. 2009). In other words, the total potential, Φ_T is:

$$\Phi_T = \Phi_{bh} + \Phi_{NSC} \ . \tag{4.1}$$

The gravitational potential of the black hole is included as a point-mass potential:

$$\Phi_{bh} = -\frac{GM_{bh}}{r} \ , \tag{4.2}$$

where $M_{bh} = 4 \times 10^6$ M$_\odot$, and r is the radial distance from SgrA*. Furthermore, to include the gravitational effects of the NSC, I adopt the potential described by Stolte et al. (2008):

$$\Phi_{NSC} = \frac{1}{2} v_c^2 \ln\left(R_c^2 + r^2\right) \ , \tag{4.3}$$

where $v_c = 98.6$ km/s is the velocity on the flattened portion of the rotation curve at very large radii, and $R_c = 2$ pc is the core radius.

4.2.2 Turbulence driving

For the simulations presented in this Chapter, we used a modified version of the turbulence driving method described in Salas et al. (2021) (see also Chapter 2). I describe the modifications below:

We use two different turbulence models that represent different physical scenarios (see Section 4.2.3). The physical size of these turbulence cubes are set to L_{cube} per side, depending on the turbulence model. The volume of the simulation's domain (which is 10 pc per side) is filled with a number N of these cubic lattices per side (where $N = 4$ or 100, depending on the model, see Section 4.2.3), each drawn randomly from the usual library of 10 files of turbulence.

Run name	Turbulence scale	ΔE_{in} (ergs)	Δt (yrs)
STS-t100-47	Small (0.05-10^{-4} pc)	10^{47}	100
STS-t500-47	Small (0.05-10^{-4} pc)	10^{47}	500
LTS-t5-49	Large (2-0.3 pc)	10^{49}	10^5
LTS-t5-50	Large (2-0.3 pc)	10^{50}	10^5

Table 4.1: Parameters of all turbulence runs. ΔE_{in} corresponds to the total energy per injection, and $\Delta t = N_t \Delta t_s$ is the time between injections.

To drive the turbulence, the code adds a velocity increment to every SPH particle, i, given by (see Equation 2.10):

$$\Delta \vec{v}_i(x, y, z) = F(\rho_i) A \vec{I}_i(x, y, z) \ . \tag{4.4}$$

The term $F(\rho_i)$ is a factor that depends on the particle's density, ρ_i, and on the turbulence model (see Section 4.2.3). Any particle outside the simulation domain does not receive any turbulent energy.

As described in Chapter 2, my turbulence implementation contains two free parameters: ΔE_{in}, the total energy input per instance of turbulent energy injection, and $\Delta t = N_t \Delta t_s$, the time between velocity "kicks". I show below the chosen parameters in our models.

4.2.3 Turbulence models

Here I describe our turbulence models and assumptions. We consider 1) a large-scale model and 2) a small-scale model, each corresponding to different physical scenarios. Table 4.1 summarizes the runs and parameters to be used based on our models.

Model 1 - Small turbulence scales (STS)

We first investigate a small-turbulence-scale model by setting $L_{cube} = 0.1$ pc (where L_{cube} is defined in Chapter 2). Thus, energy is injected on scales $\lambda = 0.05$ pc to 10^{-4} pc (for $k = 2$ and $k = 128$, respectively). We fill the volume of our simulation domain ($10 \times 10 \times 10$ pc) with $N = 100$ of these boxes per side. This model can represent, for example, turbulence driven by stellar winds, occasional novae, and outflows from Wolf-Rayet stars throughout the CND. We expect such perturbations to affect the surrounding gas of the CND on few-hundred-year timescales. Therefore, we run two injection timescales, $\Delta t = 100$ yrs and $\Delta t = 500$ yrs. The injection energy was set to $\Delta E_{in} = 10^{47}$ ergs. In comparison, the wind of a standard AGB star emits about 10^{41} ergs of energy every 100 yrs, assuming a mass loss rate of 10^{-6} $M_\odot$/yr and a wind speed of 15 km/s. The energy injection in this STS model would then be equivalent to the wind of $\sim 10^6$ AGB stars distributed throughout the disk, assuming all of that energy is transferred to the gas[1].

Furthermore, in Salas et al. (2021) the turbulent velocity kicks have a density dependence factor $F(\rho) = \sqrt{G\rho}$, which helps counteract the effects of self-gravity. This density factor is not needed in this STS model since a temperature of 200 K creates a sufficient thermal pressure gradient in the gas disk to counteract its self-gravity. Thus, in this model we eliminate this density dependence by setting $F(\rho) = 1$.

Model 2 - Large turbulence scales (LTS)

We next consider a large-turbulence-scale model by setting $L_{cube} = 4$ pc. Thus, energy is injected on scales $\lambda = 2 - 0.03$ pc (for $k = 2$ and $k = 128$, respectively). This model represents, for example, turbulence driven by supernovae (SNe). We fill the volume of our simulation domain with $N = 4$ of these boxes, each box occupying a quadrant of the

[1]The energy injection in the STS model represents an upper limit. However, as we discuss in Section 4.4, even this large energy injection does not affect the CND significantly. Thus, any lower (and more realistic) energy injection would have even less discernible effects on the CND.

simulation domain (which in this case has a volume of $8 \times 8 \times 4$ pc). Because the effect of a supernova is localized to a few parsecs and not distributed uniformly across the disk, we activate the turbulence driving only in one randomly chosen quadrant of the simulation volume at a time.

We expect disturbances caused by SNe to drive turbulence over longer timescales than in the case of STS. Thus, we adopted an injection interval of 10^5 yrs, roughly the average lifetime of a supernova remnant. Furthermore, given the number of massive stars within the central few parsecs of the Galaxy (e.g., Do et al. 2013; Nishiyama & Schödel 2013) we might expect their recurrence timescale to be also on the order of 10^5 years. SN explosions release $\sim 10^{51}$ ergs of energy, which drives a blast wave through the ambient ISM. However, the properties of the environment within which a SN explodes strongly affect the fraction of energy that is deposited into the surrounding gas (Dwarkadas & Gruszko, 2012). For example, Cox (1972) estimates that 10% of the initial SN energy is retained as thermal and kinetic energy in the gas. Chevalier (1974) obtained a fraction between 4-8%, depending on the ambient density, assumed homogeneous. Other studies have found fractions from up to 50% (McKee & Ostriker, 1977; Cowie et al., 1981) to just a few percent (Slavin & Cox, 1992; Walch & Naab, 2015). Therefore, we opted for testing energy injection values of ΔE_{in}= 10^{49} and 10^{50} ergs, which correspond to 1% and 10% of a typical SN energy, respectively. Additionally, here we use a density factor of $F(\rho) = \rho^{-1/4}$ (see Equation 4.4) to capture the density dependence of the expansion velocity of a SN shockwave during the snowplow phase (e.g., Cioffi et al., 1988).

Finally, as was shown in Salas et al. (2021) (and in Chapter 2), our turbulence method enhances the inward angular momentum transport of gas. In this model, rather than a slow inward migration, the large-scale perturbations could potentially send gas onto ballistic trajectories towards the center. Thus, to counteract the rapid filling of the CND cavity due to turbulence, I included an additional modification to Gadget2 in order to mimic the

outflow from the young nuclear cluster of massive, windy stars. I achieve this by adding a radially outwards velocity, $v_i(r)$, to every SPH particle, i, within 1.5 pc of the center (see Section 4.6 for further details):

$$v_i(r) = f v_{esc,i}(r) \sqrt{\frac{n_0}{n_i}} \ , \tag{4.5}$$

where $v_{esc,i}(r)$ is the escape velocity of an SPH particle at radius r, $n_0 = 10$ cm^{-3} is the assumed outflow number density where it strikes the inner edge of the CND (the simulations by Blank et al. 2016 assumed an outflow density of $n_0 = 100$ cm^{-3} at $r = 0.5$ pc. However, since the outflow's density decreases by $1/r^2$, $n_0 \approx 10$ cm^{-3} at $r = 1.5$ pc), and n_i is the number density of an SPH particle at the inner edge of the CND. Finally, I add the free parameter f in order to adjust the magnitude of this radial velocity so that the inner edge maintains a stable radius. This also avoids launching particles off to infinity, which creates numerical errors in the simulations. In our calculations, we find the optimal value of $f = 0.15$.

I note that this treatment is artificial, since a realistic treatment of the NSC's outflow proves to be extremely difficult with Gadget2. However, the goal here is only to prevent the rapid inflow caused by the turbulence, which causes numerical problems when particles pile up near the origin.

4.3 Initial conditions

For simplicity, we start with a gas disk having initial parameters drawn from observations: an inner radius of 1.5 pc, outer radius 4.5 pc, and a Gaussian scale height of 0.2 pc. The disk contains 10^6 SPH particles and a total mass of 4.5×10^4 M$_\odot$. The particles are initially in circular orbits, with their velocities calculated using the potential described in Section 4.2.1. All simulations were run using an isothermal equation of state with $T = 200$ K.

4.4 Results

We ran each turbulence test for 3 Myrs, which is far greater than the dynamical timescale of the disk ($\sim 0.1 - 0.3$ Myrs), allowing us to assess the long-term effect of the induced perturbations. The results are shown and described below.

4.4.1 Model 1 (STS)

Snapshots of the time evolution of the STS-t100-47 run are shown in Figure 4.1, which present the column number density maps at 1, 2 and 3 Myrs (here I show only one of the runs, since both STS simulations are qualitatively identical). Given that the spatial scales over which the energy injection is distributed are relatively small, the net effect of turbulence is manifested on only the smallest of scales, as expected. The small-scale converging flows create a granular structure throughout the disk, and this texture continues during the entire simulation.

Furthermore, my driving method creates a "turbulent" viscosity which promotes the transfer of angular momentum, as discussed in Salas et al. (2021) (Chapter 2). These viscous forces broaden the disk slightly: the disk expands radially outwards, which increases the outer radius, while the inner radius decreases slightly. The cavity closes at a faster rate than the disk's expansion, but the inward migration rate was still relatively slow. We did not impose an artificial radial outflow as in the LTS runs, since we presumed, correctly, that it was not needed. Overall, the STS models reached steady state early on in the simulations.

4.4.2 Model 2 (LTS)

The evolutionary progressions of the LTS-t5-49 and LTS-t5-50 runs are shown in Figures 4.2 and 4.3, respectively. The effects of the turbulence are much more prominent here than in the STS models. The large-scale turbulence perturbations are quickly stretched out into long arcs by the strong tidal shear, which promotes the formation of continuous, orbiting

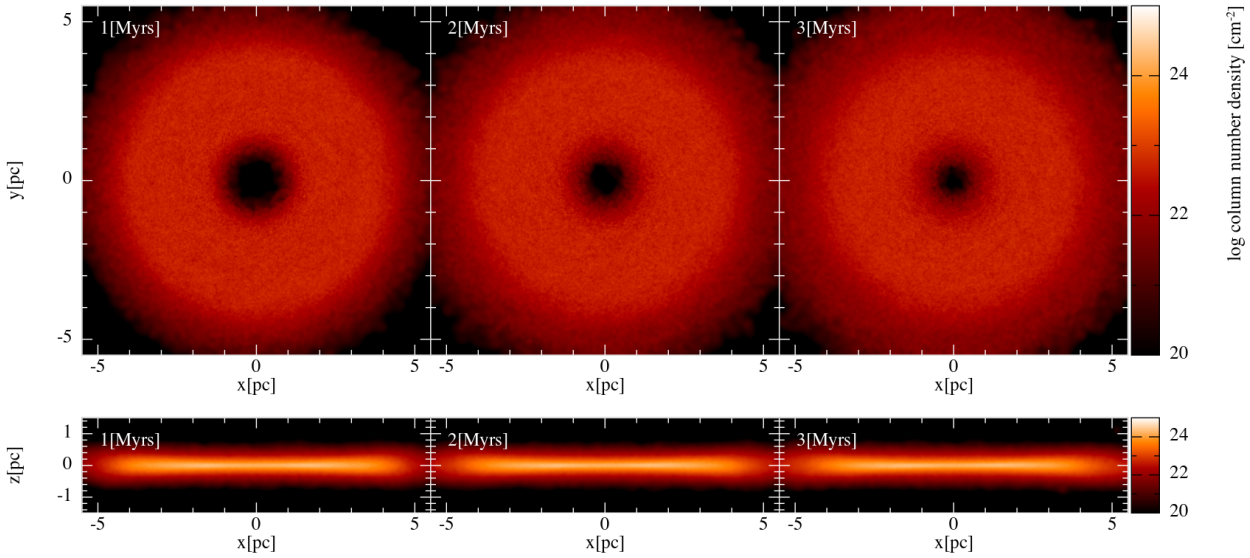

Figure 4.1: Column number density of the Small Turbulence Scale (STS) model featuring its evolution through the simulation. The simulation was run for 3 Myrs with injection energy of 10^{47} ergs at intervals of $\Delta t_N = 100$ years. Top panel: Face-on view; bottom panel: edge-on view.

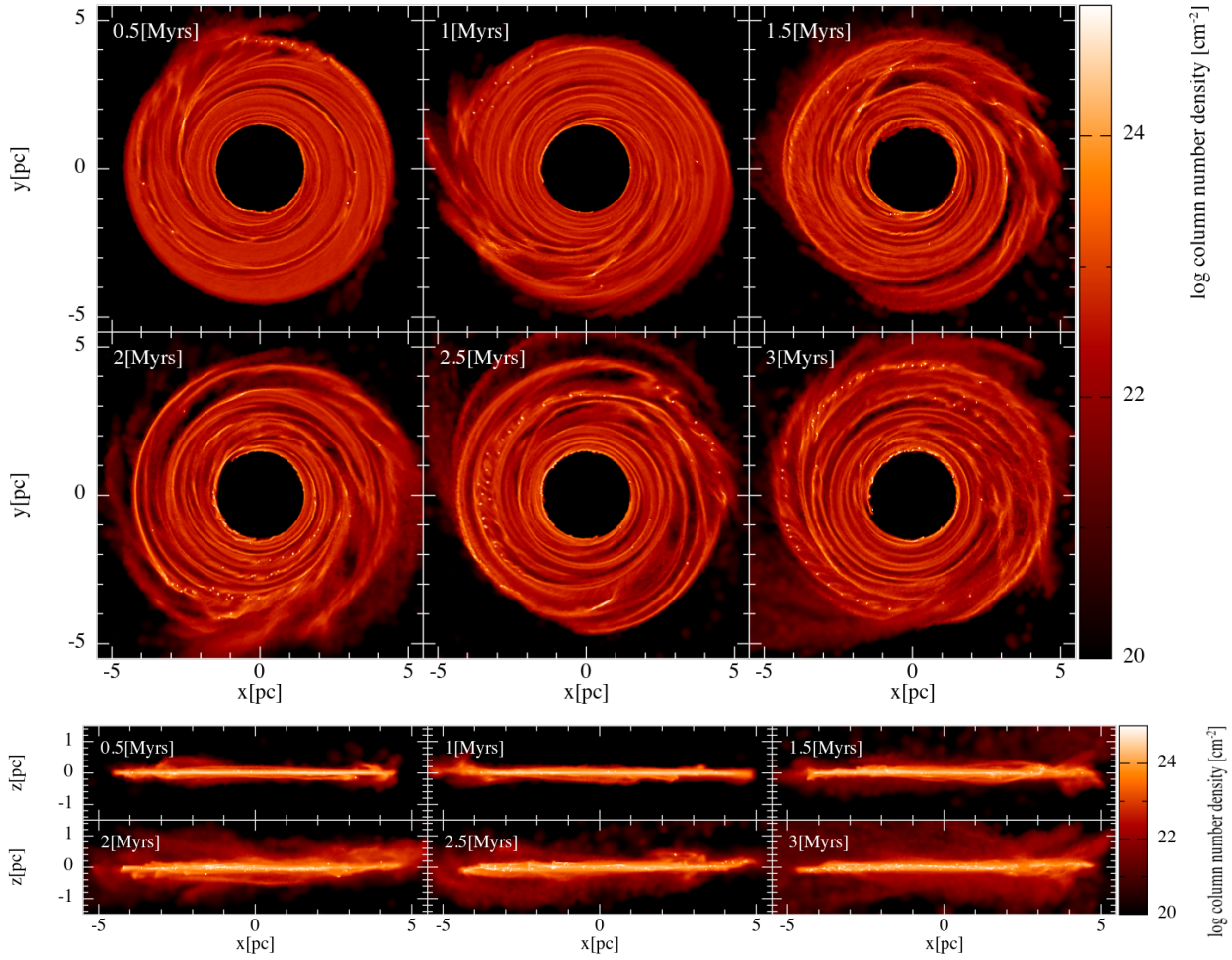

Figure 4.2: Column number density maps featuring the evolution of the Large Scale Turbulence model (LTS-t5-49). The run was run for 3 Myrs with injection energy of 10^{49} ergs at intervals of $\Delta t = 10^5$ years. Top: face-on view, rotates counter-clockwise. The disk is fully and densely permeated by identifiable spiral streams by ~ 1 Myr after the start of the simulation. Compact, high-density concentrations appear by 0.5 Myrs but are not prominent until 2 Myrs. Bottom: edge-on view. Material is increasingly perturbed off the disk as the model evolves.

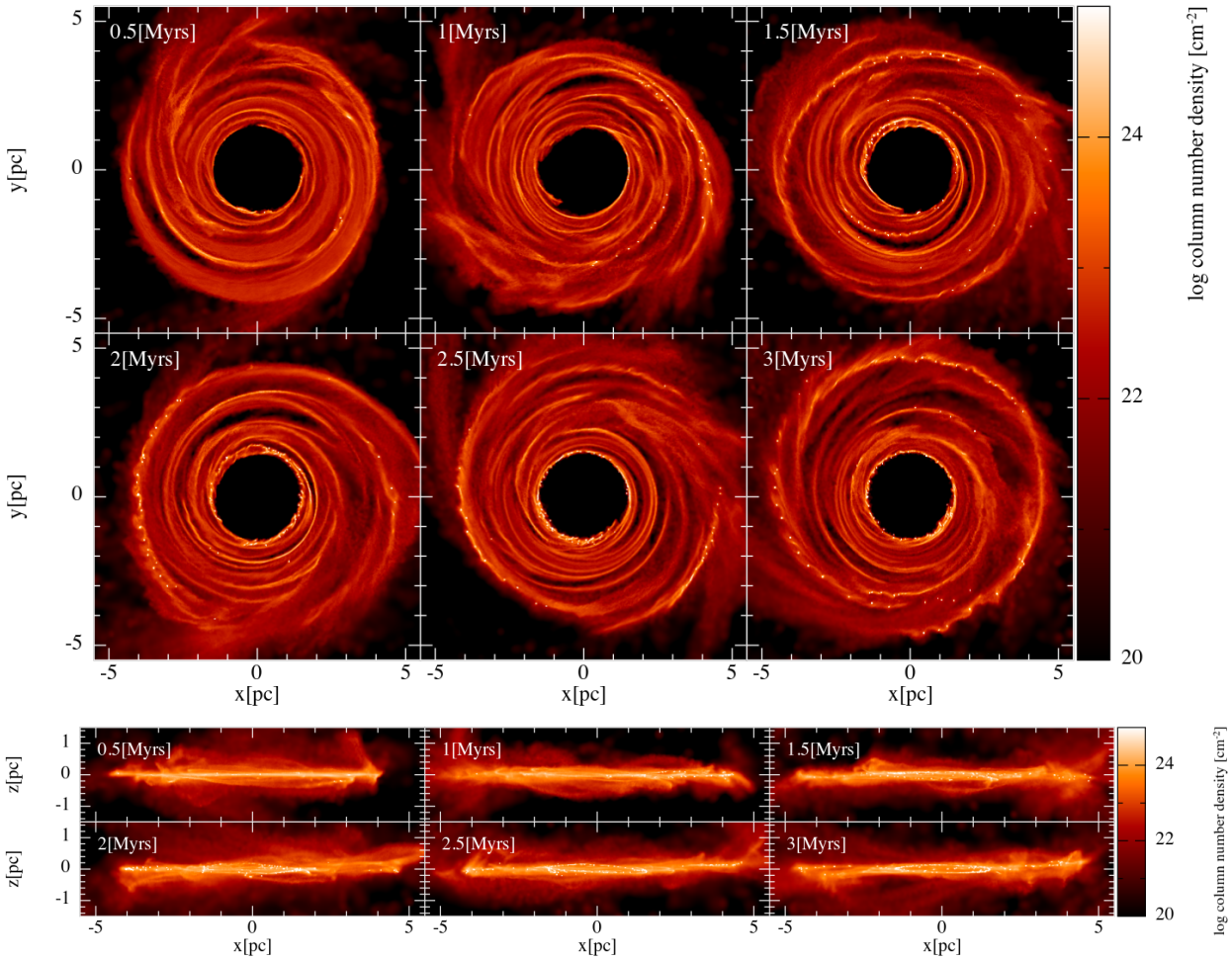

Figure 4.3: Column number density maps depicting the evolution of the Large Turbulence Scale model (LTS-t5-50). The simulation was run for 3 Myrs with injection energy of 10^{50} ergs at intervals of $\Delta t = 10^5$ years. Top: face-on view, rotates counter-clockwise. Much more distinct streams with higher densities (especially comparing to LTS-t5-49 at 3 Myrs). Bottom: edge-on view. More prominent perturbations off the disk plane than in the LTS-t5-49 model, as expected.

spiral stream segments. While these features are apparent in both runs, streams in the LTS-t5-49 run are less distinguishable in comparison to those in the LTS-t5-50 run. For example, the streams fully encapsulate the disk by $\sim 0.5 - 1$ Myrs in the LTS-t5-50 run, but only by ~ 1.5 Myrs in the LTS-t5-49 run. This is because the ten times greater energy in the LTS-t5-50 simulation provokes more prominent perturbations which are then sheared by the disk's rotation into higher contrast streams. This effect is showcased in Figure 4.4, where we plot the column number density map of the LTS-t5-50 run between two energy injections. The imprint of the turbulence grid is apparent at 1.71 Myrs (left panel in Figure 4.4). This imprint occurs at every injection, and it was was an expected result, since the size of the turbulence grid is comparable to the scale of the CND. While the injection procedure in this LTS model is geometrically oversimplified, the grid's imprint, as well as the turbulent perturbations, disappear and are quickly sheared into orbiting streams, leaving no memory of the shape of the initial disturbance domain.

The bottom panels of Figures 4.2 and 4.3 show that material was perturbed off the disk as the simulations evolved. This is because the turbulent velocity kicks in the LTS simulations are density-dependent: due to the imposed density factor of $F(\rho) = \rho^{-1/4}$ (see Equation 4.4), lower density promotes higher turbulent kicks. Thus, the turbulence is very effective in perturbing the lower density gas off the disk plane, creating an "atmosphere" of low-density gas surrounding the higher density disk. As such, the LTS-t5-50 run, due to its higher energy injection rate, had more material perturbed off the disk plane (see bottom panel of Figure 4.3) compared to the LTS-t5-49 run (bottom panel of Figure 4.2). For the remainder of this Chapter, I focus on the analysis of the LTS-t5-50 model due to its more prominent structure.

One more thing to note is the presence of compact, high-density concentrations (the small white points in Figures 4.2 and 4.3) in both runs. These points formed early on and slowly increased in number over the course of the simulations. These clumps originate because, as mentioned in Chapter 2, local regions collapse under self-gravity. Particles pile on top of

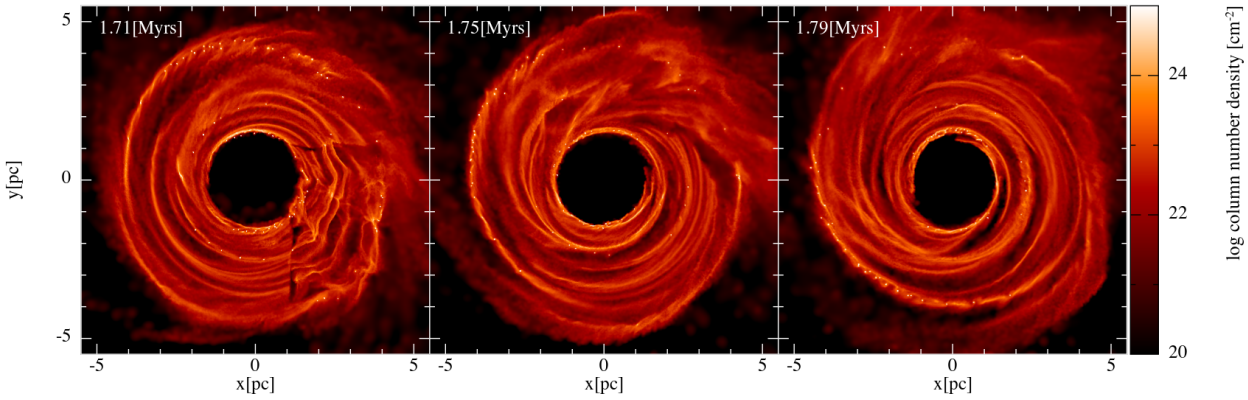

Figure 4.4: Column Number density map depicting the evolution of the Large Turbulent Scale model (LTS-t5-50) between two energy injections. Face-on view with the disk rotating counterclockwise. The imprint of the turbulence grid just after it is imposed is apparent at 1.71 Myrs (left panel). While the geometry of the turbulence injection is physically oversimplified, this structure is quickly dispersed by differential rotation, forming orbiting spiral streams that would undoubtedly be also produced by a more spatially continuous injection prescription.

each other, and due to the nature of the kernel used by Gadget2, once the distance between particles approaches the smoothing length, the pressure gradient is no longer correct and the particles stick together, creating high-density concentrations. These clumps are, in effect, sink particles that might have registered as stars if the simulations had included a prescription for star formation. Many of these clumps originate in the inner rim of the disk, which is a consequence of the piling up of particles due to the artificial radial outflow. Thus, we ignore these clumps and consider them as numerical artifacts. Their total mass is negligible, so they don't affect the evolution of the disk.

4.4.3 Comparing with observations: clumps

In order to better compare our simulation with observations of the CND, we must account for 1) the orientation of the CND in the sky, and 2) the display function of the observational data, be it linear or logarithmic.

Thus, we orient the model disk to account for the observed orientation, with a disk inclination of 70° and with the major axis at a position angle of 20° (e.g., Martín et al., 2012; Lau et al., 2013). We also display this orientation-adjusted view with a linearly scaled color map. An example is shown in Figure 4.5 (bottom left panel), which shows a snapshot of the LTS-t5-50 run at 1.83 Myrs. In addition, we convolve this column density map of the tilted LTS-t5-50 model with a 2D Gaussian kernel to match the typical full width at half-maximum beam size of existing observations (3.5", or 0.15 pc, e.g., Martín et al. 2012; Lau et al. 2013; Hsieh et al. 2017). As shown in the lower right panel of Figure 4.5, convolving the model gives rise to apparent clumps where the distorted streams become fortuitously projected and smoothed. However, most of these apparent clumps are not identifiable as such in the face-on view of the simulation (top row of Figure 4.5).

The sizes of these apparent clumps ($\sim 0.3-0.5$ pc) seem to be comparable to those described in the literature (Güsten et al., 1987; Sutton et al., 1990; Jackson et al., 1993; Marr et al.,

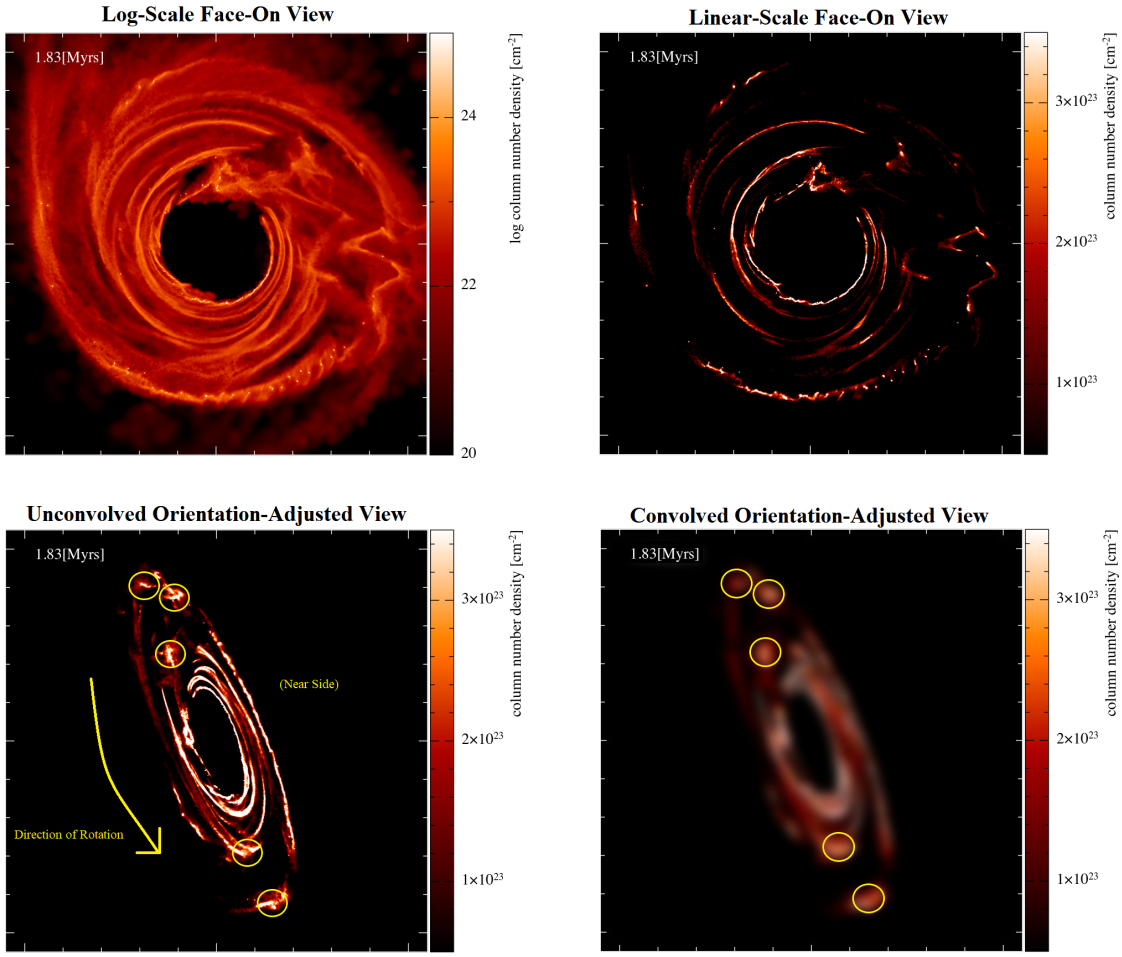

Figure 4.5: Column number density maps of the LTS-t5-50 model (domain size of 11x11 pc) at 1.83 Myrs. The upper two panels show the face-on log-scale column number density map (upper left) and its linear scale counterpart (upper right). The lower two panels compare the linear scale density map of the orientation adjusted model (lower left) with its convolved counterpart (lower right). The identified clumps are circled in yellow in both maps. There also appears to be a clump at the inner edge of the disk, however we do not consider it since it is likely a high density region due to the effects of the artificial radial outflow. The clumps in the convolved, orientation-adjusted view (bottom right) seem to be a confluence of distorted streams. Therefore, the clumps are mostly artifacts of both resolution and orientation.

1993; Shukla et al., 2004; Christopher et al., 2005; Montero-Castaño et al., 2009; Martín et al., 2012; Lau et al., 2013; Smith & Wardle, 2014), though the term "clumps" is defined in a variety of ways. For example, Lau et al. (2013) describe clumps characterized by enhanced density at the inner edge of the CND. These are possibly caused by Rayleigh-Taylor instabilities derived from the interaction of the central stellar winds and the inner edge of the CND (e.g., Blank et al., 2016). On the other hand, Montero-Castaño et al. (2009) describe the CND to be composed of tidally stable blobs with varied sizes ($\sim$ 0.15-0.54 pc), densities ($\sim 10^7$ to 10^8 cm^{-3}), and radial distances from Sgr A*.

In our model, however, apparent clumps emerge as a result of the disk projection, coupled with sampling with finite spatial resolution. In addition, when considering the two presentations of the orientation-adjusted model (lower left and right panels of Figure 4.5), we find the clumps to coincide with the densest sections of the streams. This result leads us to pose the question of whether at least some of the clumps seen in observational studies might be, in reality, turbulence-induced, transient unresolved structures in the CND. Perhaps further investigation of the CND's internal structure with higher resolution instruments such as ALMA could settle this question.

4.4.4 Comparing with observations: streams

The intrinsic structure in our LTS models consists of tidally stretched streams, which are evident when inspecting the column number density maps (see Figures 4.3 and 4.5), especially the linearly scaled maps (e.g., top right and bottom left panels of Figure 4.5). However, we can use more sophisticated methods to investigate these features in order to reduce biases when determining which particles correspond to which stream.

We employed the data clustering algorithm DBSCAN (part of the Python library *scikit-learn*, Pedregosa et al. 2011) to categorize the streams in our LTS model. DBSCAN views clusters as areas of high density (i.e., particle concentrations) separated by areas of low

density. As such, DBSCAN is able to find clusters of any shape, as opposed to the familiar "k-means" algorithm, which works better when clusters are approximately spherical. There are two parameters to the DBSCAN algorithm: *min_samples*, which represents the minimum number of points required to form a dense region, and *eps* (ϵ), which determines the minimum number of particles in a neighborhood for that neighborhood to be considered a "point". The algorithm starts with an arbitrary starting point. This point's ϵ-neighborhood is explored, and if it contains sufficiently many points, a cluster is started. Otherwise, the point is labeled as noise. Note that this point might later be found in a sufficiently sized ϵ-environment of a different point and hence be made part of a cluster.

I built a routine using DBSCAN and we applied it to the set of particle positions that have a density of at least 10^5 cm^{-3}, in order to capture the densest parts of the streams. We set *eps*, which determines the neighborhood radius of a "point" in a cluster, to 0.05 pc, and *min_samples* to 10. All particles within the inner 2 parsecs of the simulation were removed for this analysis, because the high-density region at the disk's inner edge formed due to the interaction of the gas with the artificial radial outflow. Therefore this high density region is ignored.

We applied this DBSCAN routine to the LTS-t5-50 simulation at different times and were able to identify streams in all cases. These streams are transient, with an approximate timescale dictated by the turbulence injection interval. The shape and quantity of the streams undergo frequent changes throughout the simulation; each stream is unique in its structure and longevity, a consequence of the stochastic nature of the turbulence injections. Regardless, the constant energy injections revitalize the shearing perturbations that maintain general stream morphology within the model; these streams dissipate within $1-2$ Myrs if the injections cease.

A representative example of this analysis is shown in Figure 4.6, where I show the face-on (top left) and orientation-adjusted (top right) particle position plots of the LTS-t5-50

model at 2.39 Myrs. The number and characteristics of streams found at these times vary, but streams are always present and are easily identified by DBSCAN, as shown in different colors in Figure 4.6. Furthermore, it is shown in the bottom panel of Figure 4.6 the radial velocity vs position angle of the streams, as was done by Martín et al. (2012) (c.f. their figure 9). The streams closely follow the trend outlined by the data points from their study, which were reproduced in the Figure. However, there is much overlap between streams which would be difficult to discern if the streams were not colored. For example, at Position Angle $\sim 200°$, there is noticeable overlap between the purple and orange streams. It is possible that similar structures seen in CND observations may present a similar degeneracy, especially if observed structures have been categorized by visual inspections. Thus, we note the importance of a clustering algorithm to find structures in the CND more effectively.

However, the DBSCAN routine was less effective at identifying streams when it was applied to the orientation-adjusted view because the tilt of the disk decreases particle separations and superposes streams upon each other, as shown in the upper right panel of Figure 4.6. In addition, streams that happened to connect at one or more locations are often unidentifiable as separate entities.

Consequently, our results indicate that there could be more streams than might normally be observed due to the disk's orientation or the resolution. Using an elaborated version of DBSCAN or some equivalent algorithm, perhaps one that includes velocity information, could facilitate the identification of streams and other structures in both observations and models.

4.5 Discussion

In this Chapter I have presented 3D SPH simulations, which where performed in collaboration with UCLA undergraduate student Cuc Dinh, that explore the effects of turbulence on the dynamical evolution of the CND. These simulations, which include self-gravity and

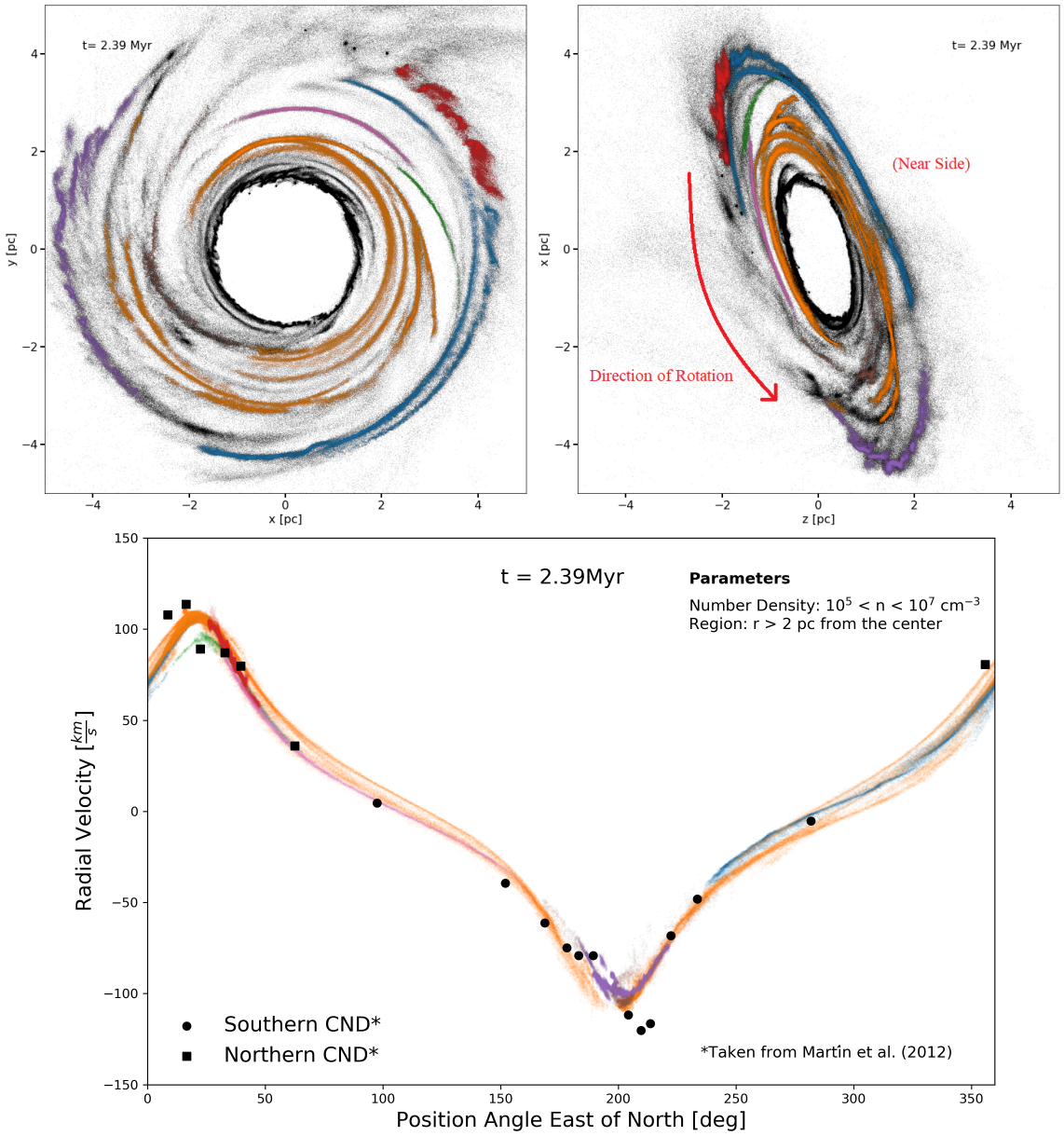

Figure 4.6: Results from DBSCAN on the LTS-t5-50 model at 2.39 Myrs. The upper left panel displays seven identified streams (colored) imposed on the entire disk model. The upper right panel accounts for the observed orientation. The streams were first identified in the face-on view before the model was rotated, thus they are less evident in the rotated view. The bottom panel shows the plot of radial velocities vs position angle of the particles in their corresponding streams (using the same colors). This trend closely follows the data points from Martín et al. (2012), which are reproduced in the Figure.

an adapted turbulence driving mechanism, are based on two models representing different driving scales.

The Small Turbulence Scale (STS) models did not show sufficient structure to match the morphology revealed by observations (see Figure 4.1). This is not surprising since the scales at which turbulence is stirred in this model are quite small ($0.05 - 10^{-4}$ pc) and their effect on the much larger scale CND is only to endow it with a grainy appearance. This implies that sources of turbulence that operate on such small scales only have a minor impact on the overall dynamics of the CND. Sources that operate on these scales include not only stellar winds, as previously mentioned, but also novae, pulsar wind nebulae, winds from AGB stars, winds from Wolf-Rayet and massive main-sequence stars, and magnetorotational instabilities (MRIs) from the predominantly torodial, few-milligauss magnetic field threading through the CND (e.g., Werner et al., 1988; Hildebrand et al., 1990, 1993, C.D. Dowell et al. in preparation).

In contrast, we found that turbulence driving in the Large Turbulence Scales (STS) models, which included the effects of larger scale (2-0.03 pc) sources of turbulence, such as supernova blasts, had much greater effects on the disk's evolution (see Figure 4.3). Here, the large-scale turbulence perturbations led to the formation of streams and clumps, some of which might resemble observational features of the CND. However, these streams are partially obscured when we account for both the disk's orientation and the general resolution of observations. As such, our results suggest that not only can we match the streams observed in the CND, but there could be more streams than observed.

In addition, convolving the orientation-adjusted model (see Figure 4.5) to match the resolution of observations revealed clump-like structures similar to those detailed in a number of studies. Such "clumps" are difficult to discern in the original unconvolved, orientation-adjusted model. They are also not evident in either the linear or log-scale column-density maps of the face-on model. This suggests that at least some observed clumps could be ar-

tifacts of both the resolution and the orientation of the CND. We posit that the CND is subject to episodic disturbances on large scales that, when sheared, leave a persistent pattern of spiral stream segments. In the absence of continued episodic injections of turbulence, the disk returns to a smooth state on a time scale of a few million years.

4.5.1 Origin and Longevity of the CND

The results of our LTS model show that streams and apparent clumps both naturally arise in a long-lived disk subjected to large-scale perturbations. Thus, tidally unstable clumps do not necessarily indicate that the disk itself is a transient feature, as has often been argued (e.g., Güsten et al., 1987; Requena-Torres et al., 2012). Our LTS simulations show that these clumps and streams are dynamic, constantly appearing and dissipating due to the injected turbulence. Simulations by Blank et al. (2016) also show that interactions between the nuclear stellar cluster's strong winds and the orbiting, annular disk cause instabilities at the inner edge of the CND. The existence of such mechanisms for continuously creating tidally unstable and therefore short-lived clumps and streams implies that such features cannot be used to conclude either that the CND is a transient feature or that the clumps within it must be dense enough ($n_{H_2} > 3 \times 10^7$ cm^{-3}) to be virialized and therefore tidally stable, as has often been argued (e.g., Vollmer & Duschl, 2001b,a; Shukla et al., 2004; Christopher et al., 2005; Montero-Castaño et al., 2009). Such high densities would imply extremely large CND masses of $10^5 - 10^6$ M$_\odot$, which are inconsistent with the optically thin far-IR and submillimeter fluxes from the CND (Genzel et al., 2010; Etxaluze et al., 2011). The densities required for tidal stability are also much higher than have been inferred in many recent studies (Oka et al., 2011; Requena-Torres et al., 2012; Lau et al., 2013; Mills et al., 2013; Smith & Wardle, 2014; Harada et al., 2015; Goicoechea et al., 2018; Tsuboi et al., 2018). We conclude that clumps and streams in the CND must truly be transient features.

Based on the observation that the CND appears to be disequilibrated because of the presence of internal transient structures, many publications model the formation of the CND as a

recent event that resulted from the infall of a dense cloud toward the central black hole (Sanders, 1998; Bradford et al., 2005; Bonnell & Rice, 2008; Wardle & Yusef-Zadeh, 2008; Hobbs & Nayakshin, 2009; Alig et al., 2011; Oka et al., 2011; Mapelli et al., 2012; Mapelli & Trani, 2016; Trani et al., 2018; Goicoechea et al., 2018; Ballone et al., 2019). The idea rests on the assumption that a relatively massive cloud with a very small total angular momentum can somehow be produced near the black hole, or can be produced further away, but be unimpeded in its accelerating trajectory toward the black hole. However, those assumptions are questionable. Although there remains some uncertainty about the line-of-sight placement of clouds in the central molecular zone (CMZ, Morris & Serabyn 1996), gaseous structures in the CMZ appear to move on orbits that conform to the sense of Galactic rotation (e.g., Henshaw et al., 2016), even if they are influenced by a non-axisymmetric potential or by radial accelerations caused by extreme accretion or starburst activity at the center. Therefore CMZ clouds have considerable angular momentum. Creating a cloud with near-zero angular momentum, or one with a retrograde orbit that could eliminate the angular momentum of other clouds by colliding with them, would therefore require it to be scattered at a large angle, but there are no known massive perturbers that could do that, including other clouds, because the sizes of clouds are large enough that they cannot approach each other closely enough to cause scattering by more than about 10° without colliding and merging, thereby preserving their angular momentum. Even with some undefined scattering process at work, the phase-space volume into which clouds would need to be scattered to be brought from a distance of more than several parsecs to the vicinity of the black hole is very small; the centrifugal barrier for a CMZ cloud scattered at almost any angle would be encountered at a radius larger than that of the CND[2]. Furthermore, any large cloud having a non-conforming velocity would collide within a few dynamical times with other clouds and would be forced eventually into conformity with the CMZ. Consequently, the production of the CND by a

[2]Supernova blast waves can push ambient gaseous material from moderately large distances into the zone of the CND (Palouš et al., 2020b), but the mass of material moved in that way is much smaller than the mass of the CND.

radially infalling cloud appears to be extremely difficult. We therefore conclude that the CND is not a transient feature, but is rather an enduring structure that is fed piecemeal and relatively slowly and quasi-continuously by tidal streams from CMZ clouds already orbiting in its vicinity, as some authors have suggested (Ho et al., 1991; Wright et al., 2001; Hsieh et al., 2017; Tsuboi et al., 2018).

The evolution of the CND is also linked to its propensity to occasionally form stars and to its relationship to the central black hole. The young nuclear cluster of massive stars occupying the central 0.5 pc presumably formed in a starburst event from an earlier manifestation of the CND, when the inner radius extended all the way in to the black hole and probably fed the black hole at a far higher rate than it is fed at present. This could happen again if the CND continues to be sustained by inwardly migrating material from the outside and if it undergoes viscous evolution that eventually causes its inner edge to move inwards. Indeed, this could be a repetitive process in which the CND undergoes a limit cycle of activity punctuated in each cycle by a relatively brief starburst event (Morris et al., 1999). To address such a scenario, future simulations are needed to account for the effects of the magnetic field, CND feeding from the outside, and other physical processes not included in our models. Additionally, continued investigations with ALMA and other high-resolution instruments will be invaluable for investigating the internal disk morphologies proposed for the CND in this Chapter.

Software: Figure 4.1 to 4.5 were done using the SPH visualization software `SPLASH` (Price, 2007). We used a modified version of the Gadget2 code (Springel, 2005) which includes my turbulence method. The version of the code can be found in my online repository:
https://github.com/jesusms007/CNDturbulence.
Finally, we used the unsupervised machine learning algorithm DBSCAN, which is part of the Python library *scikit-learn* (Pedregosa et al., 2011).

4.6 Appendix: Artificial outflow

I showed in Salas et al. (2021) (Chapter 2) that me turbulence driving module enhances inward angular momentum transport of gas. To counteract the rapid filling of the CND cavity due to turbulence, I needed to mimic the effects of the outflow from the NSC on the inner edge of the CND. Blank et al. (2016) modelled the NSC's outflow by assuming a number density of $n_0 = 100$ cm^{-3} and a speed of $v_0 = 700$ km/s, propagating radially outward from a starting radius of $r = 0.5$ pc, and found that its interaction with the inner edge of the CND creates instabilities and a shock at their interface. However, for the simulations in this Chapter, I only approximate the effects of the outflow on the CND gas.

Due to the outflow, a parcel of gas at the inner edge of the disk will gain a radially outward velocity, but the gas in the disk will impede its progress. I assume ram pressure balance, such that the parcel's speed is constant. From the parcel's frame of reference, it experiences a ram pressure $P_{outflow} = \rho_0 v_0^2$ from one side (where ρ_0 and v_0 are the mass density and speed of the outflow, respectively), and a ram pressure from the opposite direction, $P_{CND} = \rho_{CND} v_{CND}^2$ (where ρ_{CND} is the mass density of the neighboring gas, which is assumed to be identical to the parcel's, and v_{CND} is the parcel's speed as seen from the CND's frame of reference). The parcel's speed will then be,

$$v_{CND} = \sqrt{\frac{\rho_0}{\rho_{CND}}} v_0 = \sqrt{\frac{\mu_0 n_0}{\mu_{CND} n_{CND}}} v_0 \ , \tag{4.6}$$

where μ_0 and μ_{CND} are the mean mass per particle of the outflow's ionized gas, and the molecular CND gas, respectively. The ratio $\sqrt{\mu_0/\mu_{CND}}$ is subsumed in the factor f, described below.

I then convert this treatment to work with Gadget2. However, here I consider the outflow's density at $r = 1.5$ pc, and since the outflow's density decreases with $1/r^2$, I thus adopt a value of $n_0 = 10$ cm^{-3}. Furthermore, because I am not accounting for the additional hydrodynamical interaction between the outflow and the CND, a speed of $v_0 = 700$ km/s,

which is much larger than the escape velocity, would send SPH particles flying out to infinity, causing numerical problems in the code. I simplify this problem by assuming that the largest speed this artificial outflow will add to an SPH particle (which happens when the SPH particle number density, n_i, is equal to the outflow's, i.e., $n_i = n_0$. For particles with $n_i < n_0$, no radial speed is added. This limit is acceptable since we find in our simulations that they are very few particles with $n_i < n_0$ throughout the disk) equals a fraction of the particle's escape speed, $f v_{esc,i}$. This parameter f was adjusted in order to maintain a stable radius of the CND's edge. In the testing phase, I found $f = 0.15$ satisfied this condition.

Thus, to mimic the NSC's outflow, every timestep the code adds a radially outward speed to every SPH particle, i, within a radius $r = 1.5$ pc equal to:

$$v_i(r) = f\sqrt{\frac{n_0}{n_i}} v_{esc,i}(r) \ , \tag{4.7}$$

where $v_i(r)$, $v_{esc,i}(r)$ and n_i are values corresponding to a given SPH particle.

CHAPTER 5

Conclusions

Supersonic turbulence occurs over a wide range of length scales in the interstellar medium, especially within molecular clouds. The importance of turbulence in modulating star formation in the interstellar medium was highlighted recently by a combination of numerical and analytical studies (e.g., Krumholz & McKee, 2005; Burkhart, 2018). Furthermore, turbulence in the Central Molecular Zone (CMZ) seems to greatly influence its thermal structure and star formation rate (e.g., Kruijssen et al., 2014).

Numerical simulations have shown that turbulence decays quickly, within a few dynamical timescales (e.g., Stone et al., 1998; Mac Low, 1999). Since observations indicate high turbulent velocity dispersions in the CMZ clouds (Morris & Serabyn, 1996), turbulence then must be driven by some physical stirring mechanism, e.g., magnetic fields, secular gas instabilities, feedback ejecta, etc. However, the main driving mechanism for turbulence in the CMZ has not yet been definitively identified (Kruijssen et al., 2014).

In this work I have presented a new method for driving turbulence in SPH simulations of gas that orbits under the influence of a gravitational potential. In order to avoid relying on a particular physical mechanism, I adopted a Fourier forcing module, which has the advantage of being independent of the source of turbulence. My turbulence treatment was based on the method described by Mac Low (1999), in which a turbulent velocity field is drawn from a spatially static pattern having a power spectrum $P(k) \propto k^{-n}$, where k is the wavenumber.

In Chapter 2 I described in detail this turbulence model, as well as the performance tests I conducted to show its effectiveness, based on my paper, (Salas et al., 2021). I showed how this turbulence injection method is capable of balancing the self-gravity of the gas, which allowed me to run simulations for long timescales and thereby follow the evolution of the CMZ. My results showed that turbulence induces flocculent spiral patterns in the CMZ, analogous to that found in galactic-scale simulations, as well as observations of other galactic centers. Additionally, I found that my turbulence injection method induces inward migration of gas, a result consistent with previous numerical simulations. I also described all the parameters that can be modified to simulate different physical scenarios, such as the scales of injected turbulence, and the size of the computational domain.

To further show how this new turbulence driving method can be used in other physical scenarios, in Chapter 3 I showed the results of SPH simulations from my paper, Salas et al. (2020), which showcases the effects of turbulence in galactic nuclear rings. I performed 3D simulations which include self-gravity of gas in a galactic barred potential out to a radius of 2 kpc. I studied how the formation of gaseous nuclear rings is affected by changing the bar pattern speed and the strength of the turbulence, and compared the results to the effects of thermal pressure (using simulations with a relatively high sound speed). I used two values for the bar pattern speed that have been discussed in the literature for our Milky Way Galaxy (40 and 63 km s^{-1} kpc^{-1}). My results showed that turbulence produces broader and smaller nuclear rings, and enhances gas migration towards the inner few pc of the galaxy, compared to simulations without turbulence. This was caused by the turbulent viscosity induced by the driving method. However, I emphasized that unlike standard viscosity treatments, my turbulence method is capable of not only inducing an effective viscosity, but also producing the typical filamentary density structures that should be expected in the presence of turbulence.

In fact, my results showed that a high turbulence injection rate is capable of driving gas

from the simulated nuclear ring to the central few parsecs, forming a pile up of material around the central black hole. Observations indicate that a Circumnuclear Disk (CND) of molecular gas occupies the central few parsecs of the Galactic Center. This disk is likely subject to turbulent disruptions from violent events in its surrounding environment, but the effect of such perturbations has not yet been investigated in detail. In Chapter 4, I presented simulations of the Circumnuclear Disk done in the paper by Dinh et al. (2021), written in collaboration with Cuc Dinh, whom I mentored for this project. We presented 3D, N-body/smoothed particle hydrodynamic (SPH) simulations using an adapted version of my turbulence driving method to investigate the CND's structural evolution, in particular its reaction to varied scales of injected turbulence. We found that, because of shear flow in the disk, transient arcs of gas (streams) naturally arise when turbulence is driven on large scales (up to $\sim$ 4 pc), as might occur when a supernova blast wave encounters the CND. Because energetic events arise naturally and often in the central parsecs of our Galaxy, this result suggests that the transient structures that characterize the CND do not necessarily imply that the CND itself is a transient structure. We also noted that features similar to the density concentrations, or "clumps", detailed in literature emerge when we account for the observed orientation of the disk and for the spatial resolution of observations.

5.1 Future Work

The next steps in modeling the dynamics of the CMZ should include the effects of magnetic fields. Complicated structures have been observed which revealed the presence of a strong magnetic field in the CMZ, such as non–thermal radio filaments (NTFs) within 150 pc of the GC (Yusef-Zadeh, 1989; Morris, 1990, 1994, 1996), including the Radio Arc (Yusef-Zadeh et al., 1984). By studying these NTFs, Yusef-Zadeh & Morris (1987a,b, 1988) have determined that the magnetic field within the NTFs has milligauss strength.

Consequently, the magnetic field within the CMZ can play a significant role on the dynamics

of the gas (see, e.g., Sofue 2007). But, in spite of the wide recognition of the strong magnetic field in the GC, there have been few theoretical studies that explore its role on the gas dynamics (e.g., Machida et al. 2009; Kim & Stone 2012; Machida et al. 2013; Suzuki et al. 2015). Some important questions to consider are: can magneto-hydrodynamic turbulence support the observed high gas densities in the CMZ against gravitational collapse? Are the resulting dynamics fundamentally different than adding artificial turbulence? Is the inclusion of both turbulence and magnetic fields necessary to reproduce the observed properties of the gas in the CMZ? The answers can provide a hint on the sources of the observed turbulence in the galactic center.

The ability to perform stable magneto-hydrodynamics (MHD) calculations in SPH has proven to be extremely difficult (Lewis et al., 2016). Grid methods, such as AMR or moving-mesh codes, are generally a more suitable tool for MHD simulations.

Some examples of available codes are: There are three different numerical codes that I can use for my thesis work:

- **ENZO** (Norman & Bryan, 1999): Is a community-developed AMR simulation code, designed for rich, multi-physics hydrodynamic astrophysical calculations. Enzo has a strong support structure for assistance and is capable of running on a wide range of systems (from personal workstations to High Performance Computing facilities).

- **ASTROBEAR** (Cunningham et al., 2009; Carroll-Nellenback et al., 2013): Is a high-resolution shock-capturing AMR/MHD code, and it includes several numerical solvers, integration schemes, and radiative cooling modules for astrophysical fluids.

- **GIZMO** (Hopkins, 2015): Is a flexible, multi-method, MHD + gravity code. It solves the hydrodynamic equations using a variety of different methods (SPH, as well as new Lagrangian Godunov–type methods). GIZMO is a heavily modified and improved version of Gadget2.

Furthermore, my turbulence method is flexible and can be adapted to these and other SPH or grid codes. Based on the work I present in this thesis, I believe that this injection method is a promising new tool to simulate turbulence in galactic centers.

APPENDIX A

The unseen companions of V-Hya

In this appendix I show an additional project that is separate from the main topic of this dissertation. The publication presented here (Salas et al., 2019) shows a numerical study that attempts to explain the mysterious ejections of the star V-Hydrae.

Monthly Notices of the ROYAL ASTRONOMICAL SOCIETY

MNRAS **487,** 3029–3036 (2019) doi:10.1093/mnras/stz1515
Advance Access publication 2019 June 3

Unseen companions of V Hya inferred from periodic ejections

Jesus M. Salas,[1]★ Smadar Naoz,[1,2] Mark R. Morris[1] and Alexander P. Stephan[1,2]

[1]*Department of Physics & Astronomy, University of California, Los Angeles, CA 90095, USA*
[2]*Department of Physics and Astronomy, Mani L. Bhaumik Institute for Theoretical Physics, University of California, Los Angeles, CA 90095, USA*

Accepted 2019 May 28. Received 2019 May 5; in original form 2019 February 15

ABSTRACT

A recent study using *Hubble Space Telescope* observations found periodic, high-speed, collimated ejections (or 'bullets') from the star V Hya. The authors of that study proposed a model associating these bullets with the periastron passage of an unseen, substellar companion in an eccentric orbit and with an orbital period of ∼8 yr. Here we propose that V Hya is part of a triple system, with a substellar companion having an orbital period of ∼8 yr, and a tertiary object on a much wider orbit. In this model, the more distant object causes high-eccentricity excitations on the substellar companion's orbit via the Eccentric Kozai–Lidov mechanism. These eccentricities can reach such high values that they lead to Roche-lobe crossing, producing the observed bullet ejections via a strongly enhanced accretion episode. For example, we find that a ballistic bullet ejection mechanism can be produced by a brown-dwarf-mass companion, while magnetically driven outflows are consistent with a Jovian-mass companion. Finally, we suggest that the distant companion may reside at few a hundred astronomical units on an eccentric orbit.

Key words: binaries: general – stars: evolution – stars: kinematics and dynamics.

1 INTRODUCTION

Observations from the *Hubble Space Telescope* (*HST*) over the past two decades have revealed an enormous complexity and diversity of structure in planetary nebulae (PNe; Balick & Frank 2002; Sahai, Morris & Villar 2011). *HST* surveys have revealed that more than half of PNe are bipolar or multipolar whereas mass-loss during the AGB phase is mostly spherical. This led Sahai & Trauger (1998) to propose that high-speed, collimated (jet-like) outflows during the late AGB phase that can change their orientation could be the reason behind the asymmetric morphology of PNe. These jets could be driven by interactions with a binary companion (Morris 1987); however, direct evidence supporting this idea has been lacking.

The carbon star V Hya is one example where there exists evidence for high-speed, collimated outflows (Lloyd Evans 1991; Knapp, Jorissen & Young 1997; Sahai & Trauger 1998; Sahai et al. 2003; Hirano et al. 2004; Sahai, Sugerman & Hinkle 2009). A recent study by Sahai, Scibelli & Morris (2016) presents new *HST* observations that span more than a decade and provide, with an unprecedented and detailed view, the extended history and characteristics of the bullet-like ejections from V Hya. Their data show that these high-speed (∼200–250 km s^{-1}) bullets are ejected once every ∼8.5 yr, and that the axis of ejection flip-flops around a roughly eastern direction, both in and perpendicular to the sky plane.

To account for this phenomenon, Sahai et al. (2016) proposed a model in which the bullets are associated with the periastron passage of a binary companion in an eccentric orbit with an orbital period of ∼8.5 yr. The bullets are likely ejected from an accretion disc formed around the companion that results from the gravitational capture of matter levitated into the primary's wind-formation zone, and perhaps directly from the primary's pulsating atmosphere. However, this hypothesis faces the difficulty that tidal forces between binary companions tend to shrink and circularize their orbits, or even cause mergers. To overcome this problem, we here propose a more elaborated model in which V Hya is part of a triple system. In such a system, a relatively distant third object can impose an eccentric orbit on the inner companion, and even lead to Roche-limit crossing, thus allowing the inner companion to accrete and eject mass.

Studies of stellar populations have shown that multiple star systems are very common, with ∼50 per cent of Sun-like stars having binary companions, and even higher fractions (∼70 per cent) are found for higher-mass stars (e.g. Raghavan et al. 2010). Moreover, it seems that many of these binaries are in triples or higher multiples. For example, Tokovinin (1997a) showed that ∼40 per cent of short-period binary stars with a low-mass (∼0.5–1.5 M$_\odot$) primary have at least one additional companion. Furthermore, among contact binaries it seems that about 42 per cent are in a triple configuration (e.g. Pribulla & Rucinski 2006). These and many other observational endeavours have revealed that triple star systems are common (e.g. Tokovinin 1997b; Tokovinin et al. 2006; Eggleton, Kisseleva-Eggleton & Dearborn 2007; Griffin 2012. See also Tokovinin 2008, 2014a,b).

★ E-mail: jesusms@astro.ucla.edu

Dynamical stability considerations dictate that triple systems must be hierarchical in scale, in which the ('inner') binary is orbited by a third body on a much wider ('outer') orbit. In this set-up, the inner binary undergoes large-amplitude eccentricity and inclination oscillations due to the 'Eccentric Kozai-Lidov' (EKL) mechanism (Kozai 1962; Lidov 1962. For a review, see Naoz 2016). These eccentricity excitations can drive the inner binary to have very small pericenter distances and even to merge (e.g. Naoz & Fabrycky 2014; Prodan, Antonini & Perets 2015; Naoz 2016; Stephan et al. 2016; Stephan, Naoz & Zuckerman 2017; Stephan, Naoz & Gaudi 2018).

The star V Hya is currently in its AGB stage with a mass of ∼1–2 $M_\odot$ and a radius of ∼2 au (see Zhao-Geisler et al. 2012). The rapid evolution of an AGB star in a triple system can play a major role in the dynamical evolution of such a system (e.g. Perets & Kratter 2012; Shappee & Thompson 2013; Michaely & Perets 2016; Naoz et al. 2016; Stephan et al. 2016; Toonen, Hamers & Portegies Zwart 2016; Stephan et al. 2017, 2018). For example, as the AGB star loses mass, it can reduce the separation ratio between the inner and outer orbits, thus re-triggering EKL eccentricity excitations (Shappee & Thompson 2013). In addition, as the star expands, tidal forces become more efficient since tides are highly sensitive to the stellar radius.

In particular for the V Hya system, EKL combined with post-main-sequence stellar evolution can drive the inner binary to very high eccentricities and even cause it to undergo Roche-lobe crossing, inducing the secondary object to accrete material from its companion, and perhaps eject some of this material from an accretion disc (Sahai et al. 2016). The mechanism we introduce here thus could explain the observed ejections from V Hya.

This paper is organized as follows. In Section 2 we describe the code and numerical set-up. Our results are shown in Section 3. A discussion of the implications of our model is given in Section 4, and we conclude in Section 5.

2 NUMERICAL METHODS

2.1 Stellar evolution and three-body dynamics

We solve the secular equations for a hierarchical triple system up to the octupole level of approximation (as described in Naoz et al. 2013a; Naoz 2016), including general relativistic effects for both the inner and outer orbits (Naoz et al. 2013b) and static tides for both members of the stellar binary (following Hut 1980; Eggleton, Kiseleva & Hut 1998, see Naoz 2016 for the complete set of equations). We also include the effects of stellar evolution on stellar radii and masses, following the stellar evolution code SSE by Hurley, Pols & Tout (2000). The interaction between the EKL mechanism and post-main-sequence stellar evolution has been demonstrated to play an important role in three-body dynamical evolution (see Perets & Kratter 2012; Shappee & Thompson 2013; Michaely & Perets 2016; Naoz et al. 2016; Stephan et al. 2016; Toonen et al. 2016; Stephan et al. 2017, 2018).

2.2 Numerical set-up

We divide the parameter space into a grid in which we choose among a set of initial values for the masses of the three bodies ($M_{\rm VHya}$, m_1, m_2), the semimajor axes of the inner and outer orbits (a_1, a_2), the eccentricities of the inner and outer orbits (e_1, e_2), and the inclination (i) between the two orbits.[1]

Based on SSE modeling, the Zero-Age Main Sequence (ZAMS) mass of V Hya ($M_{\rm VHya}$) was set to 2.2 $M_\odot$, appropriate for a carbon star. Each system is integrated for 1.2 Gyr unless a stopping condition is fulfilled. To allow for comparison with the observed system, we focus on the Late-AGB phase (L-AGB, i.e. 1.143–1.146 Gyr for the chosen mass) and determine whether the periastron of the inner orbit reaches the primary's Roche limit without merging. The Roche limit of V Hya is defined as (e.g. Paczyński 1971; Matsumura, Peale & Rasio 2010; Naoz 2016):

$$RL_{\rm VHya} = q\,R_{\rm VHya}\left(\frac{M_{\rm VHya}+m_1}{M_{\rm VHya}}\right)^{1/3} \quad (1)$$

where q is a numerical factor of order unity. However, the radius of an AGB star is not well defined; its stellar envelope can extend to large distances, perhaps filling its own Roche limit. Thus, it is reasonable to assume that mass accretion can occur when the inner companion reaches the primary's Roche limit. We note that the parameter q is rather uncertain, in particular for a bound eccentric case. Numerical simulations have suggested that this parameter can be about 2.7 (e.g. Guillochon, Ramirez-Ruiz & Lin 2011; Liu et al. 2013), and that value may be a lower limit. Other studies sometimes find and adopt a smaller value ($q \sim 1.4$–1.6; e.g. Paczyński 1971). Thus, here, we explore two limiting cases, one for which $q = 1.66$, as was adopted in Naoz, Farr & Rasio (2012), and another for which $q = 2.7$, adopted in Petrovich (2015). These two limiting cases represent two different physical pictures: interactions with an extended envelope ($q = 2.7$) and a contained envelope ($q = 1.66$). The integration was stopped when the inner orbit pericenter $R_{p,1}$ reaches 80 per cent of V Hya's radius, $R_{\rm VHya}$, i.e. $R_{p,1} \leq 0.8R_{\rm VHya}$.

We investigated a discrete range of initial values for m_1; a Neptune-sized planet (5×10^{-5} $M_\odot$), a Jupiter-sized planet (10^{-3} $M_\odot$), a brown dwarf (0.01 $M_\odot$), and a range of subsolar stellar companions (0.1, 0.3, 0.6, and 0.9 $M_\odot$). According to Sahai et al. (2016), the inner companion's mass should be sub-solar, thus we do not consider larger mass companions in our investigation.

The semimajor axis of the inner orbit (a_1) was set so that its period is 8.5 yr. We also note that it is unlikely that a planet around V Hya would have a high initial eccentricity. On the other hand, a stellar companion could have had a high initial eccentricity, but tides would have circularized its orbit by the time the primary entered the AGB phase. Thus, for the eccentricity of the inner companion, we adopt for simplicity an initial, almost circular orbit ($e_1 = 0.1$).

There is a degeneracy between m_2, a_2 and e_2 that comes from the Kozai time-scale (e.g. Naoz 2016):

$$t_{\rm quad} \propto \frac{a_2^2\left(1-e_2^2\right)^{3/2}\sqrt{M_{\rm VHya}+m_1}}{a_1^{3/2}m_2}. \quad (2)$$

and therefore we can restrict these parameters to a narrow range of values because this time-scale must be shorter than the lifetime of V Hya. However, if m_2 is larger than m_1, the system dynamics can be described well by a test particle approximation ($m_2 \gtrsim 7m_1$; Teyssandier et al. 2013). In this case, the inner orbit can reach extreme eccentricities in very short time-scales (e.g. Li et al. 2014a,b). Thus, we do not expect differences in the evolution of

[1] Throughout this paper, we use the subscripts 1 and 2 to indicate the values for the inner and outer orbits of the system, respectively. For the mass parameter, the subscripts indicate V Hya ($M_{\rm VHya}$), the inner companion (m_1) and the outer body (m_2).

Table 1. Grid of initial conditions for our 3-body model. A combination of all of these values gives a set of 2625 initial conditions. Parameters marked with an (*) were set the same for all computations. The semimajor axis of the inner orbit for each m_1 was calculated via $a_1 = (P_1^2(M_{\rm VHya} + m_1))^{1/3}$.

Parameter	Initial values
$M_{\rm VHya}$*	2.2 (in $M_\odot$)
m_1	5×10^{-5}, 0.001, 0.01, 0.1, 0.3, 0.6, 0.9 (in $M_\odot$)
m_2	0.01, 0.1, 0.3, 0.6, 0.9 (in $M_\odot$)
a_1*	Set such that $P_1 = 8.5$ yrs (∼5−6 au)
a_2	200, 400, 600, 800, 1000 (in au)
e_1*	0.1
e_2	0.3, 0.45, 0.6
i	35, 70 105, 140, 175 (in degrees)

systems for which $m_2 \gtrsim 7m_1$. We chose a lower limit of m_2 to be 0.01 $M_\odot$ (a brown dwarf). As with m_1, we chose an upper limit of $m_2 = 0.9$ $M_\odot$.

In the model we propose here, we assume that V Hya is part of a hierarchical triple system. This means that the value for a_2 must be much greater than a_1. Such a configuration allows us to use the secular approximation equations (Naoz 2016). Furthermore, a_2 needs to satisfy the following criterion for the secular approximation to be valid (e.g. Lithwick & Naoz 2011):

$$\epsilon = \frac{a_1}{a_2}\frac{e_2}{1-e_2^2} < 0.1, \quad (3)$$

where ϵ is a measure of the relative strengths of the octupole and quadrupole effects on the orbital dynamics. Therefore, we test a range of 200–1000 au in 200 au increments, with eccentricity values (e_2) of 0.3, 0.45, and 0.6.

Finally, we test a wide range of mutual orbit inclinations ($i = 35°$–$175°$ in $35°$ increments). Table 1 summarizes the parameters of our computations, which give a total of 2625 cases that were generated as initial conditions.

3 RESULTS

In this section we present the results from our 2625 simulated triple systems. We note that less than 1 per cent of our simulated systems were inconclusive, and thus we ignore those systems in our analysis.

We divide the simulations into 'survived' and 'merged' systems. We show examples in Fig. 1, which presents the time evolution of the inner orbit's semimajor axis (red), periastron distance (blue), and V Hya's stellar radius (purple) and Roche limit (green and cyan dashed lines). The Late AGB phase is shaded in purple, which lasts for ∼3 Myr for the chosen initial value of $M_{\rm VHya} = 2.2$ $M_\odot$.

(i) **Merged systems**: Here we include all systems in which the inner binary merged at any point of the evolution, which occurs in ∼37 per cent of all simulated cases (991/2625). These merged systems can be divided into two groups:

(a) **L-AGB mergers**: systems that merged during the L-AGB period (an example is shown in the middle panel of Fig. 1). These can happen via an EKL-induced high eccentricity (e.g. Shappee & Thompson 2013; Naoz & Fabrycky 2014; Stephan et al. 2018). Furthermore, because tides are highly sensitive to the stellar radius, the likelihood of a merger is increased at this stage of stellar evolution due to circularization and shrinking of the inner binary's orbit (e.g. Naoz 2016). These systems comprise ∼76 per cent of all mergers (752/991).

(b) **Pre-AGB mergers**: systems that merged in previous stages of the stellar evolution of V Hya (right-hand panel of Fig. 1). These occur due to strong EKL effects due to stellar-mass inner and outer companions, as well as strong tidal interactions between the inner binary members. Such systems are likely to give rise to blue stragglers (e.g. Perets & Fabrycky 2009; Naoz & Fabrycky 2014). These systems comprise ∼24 per cent of all mergers (752/991).

(ii) **Survived binary systems**: Here we include systems in which the inner companion survives the evolution of V Hya without merging. This occurs in ∼62 per cent of all simulated cases (1616/2625). In these systems, the semimajor axis of the inner orbit increases substantially at ∼1.146 Gyr, which is when the star sheds its outer layers and becomes a white dwarf. Most of these systems are 'no interaction' systems, in which the inner companion survives the evolution of V Hya without interacting with the primary's Roche limit (an example of such a system in shown in the left-hand panel of Fig. 1). In general, these are systems in which EKL effects were insufficient to induce high eccentricities due to, for example, nearly coplanar orbits[2] ($i = 35$ or 175 deg, such as the example in the left-hand panel of Fig. 1), high a_2 values, or ratios $m_2/m_1 \approx 1$. However, there are also systems where EKL effects did increase the inner orbit's eccentricity, but not enough to make the inner orbit's periastron cross the primary's Roche limit (see Fig. 3). Our investigation focuses on the subset of surviving systems in which the inner companion's periastron reaches the primary's Roche limit during the L-AGB phase. These occur in ∼8 per cent of all cases (examples of these systems' orbital evolution are shown in Fig. 2), and can be further divided into two subcategories:

(a) **'Grazing' systems**: where the inner companion's orbit reaches a high eccentricity ($e_1 > 0.1$) and crosses the primary's Roche limit during its periastron passage (examples are shown in the left-hand and middle panels of Fig. 2). This configuration is maintained for ∼1 Myr until the primary becomes a white dwarf, at which point the inner companion's orbit increases and exits the Roche limit. During this 1 Myr period, $M_{\rm VHya}$ ∼1.5−1.7 $M_\odot$, and $R_{\rm VHya}$ ∼1.6 au. In this configuration, the inner companion could, in principle, accrete material during its periastron passage. Then V Hya-like ejections could be produced by a transient accretion disc. The number of systems in this category depends on q. For $q = 2.7$, this condition is satisfied in ∼9 per cent of surviving systems (138/1616), while it is satisfied in only ∼2 per cent of surviving systems (27/1616) for $q = 1.66$.

(b) **'Temporary close binaries' (TCBs)**: systems where the inner companion's orbit circularizes during the Late-AGB phase and is engulfed by V Hya's Roche limit, but does not lead to a merger with the latter (an example is shown in the right-hand panel of Fig. 2). We call these systems 'temporary close binaries'. This condition is only satisfied using a factor of $q = 2.7$ in the definition of the Roche limit, and in ∼4 per cent of surviving systems (60/1616). While these cases could not produce V Hya-like systems, they are likely to end up as common envelope configurations because of the drag encountered inside the Roche limit.[3]

[2]Coplanarity does not guarantee a small eccentricity excitation, as was shown in Li et al. (2014a).

[3]Drag forces also affect the grazing systems we describe above. To determine whether the primary's extended envelope significantly affects the grazing companion's orbit is equivalent to asking whether the orbital average is

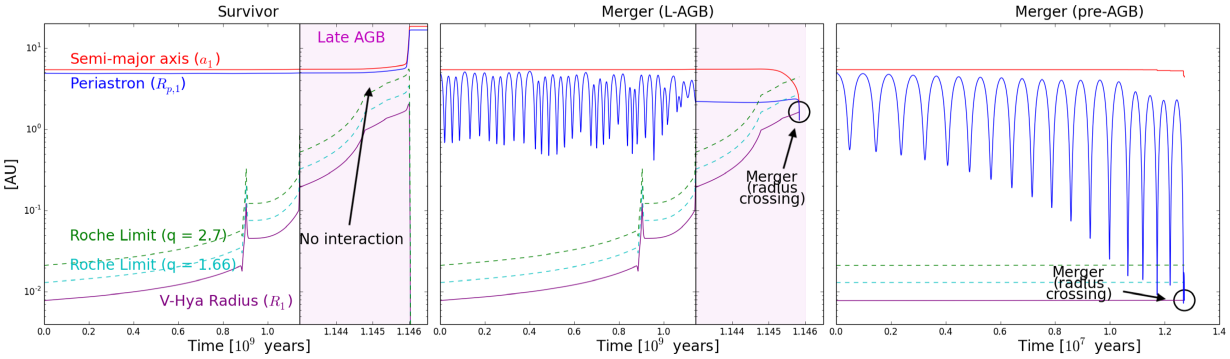

Figure 1. Example of orbital evolutions of survivor and merger systems. The purple-shaded region indicates the Late-AGB phase, which lasts for $\sim$ 3 Myr. *Left*: system in which the inner companion's periastron (blue line) never crosses V Hya's Roche limit (green-dashed line). The semi-major axis of the inner orbit (red line) increases substantially at $\sim$1.146 Gyr. This is because at this time the star sheds most of its mass and becomes a white dwarf. Initial system parameters for this system are $m_1 = 0.001$ M$_\odot$, $m_2 = 0.01$ M$_\odot$, $a_2 = 400$ au, $e_2 = 0.3$, $i = 175$ deg. *Middle*: system in which the inner companion merges with V Hya during the L-AGB phase. Initial system parameters are $m_1 = 0.001$ M$_\odot$, $m_2 = 0.01$ M$_\odot$, $a_2 = 200$ au, $e_2 = 0.45$ $i = 70$ deg. *Right*: system in which strong EKL oscillations of the inner orbit's periastron prompts the companion to merge with V Hya during the Main Sequence phase. Initial system parameters are $m_1 = 0.01$ M$_\odot$, $m_2 = 0.3$ M$_\odot$, $a_2 = 200$ au, $e_2 = 0.6$, and $i = 70$ deg.

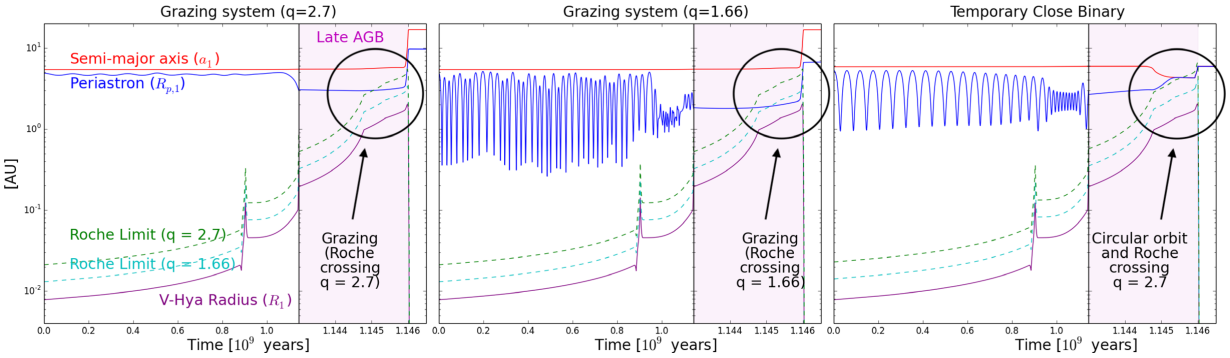

Figure 2. Example orbital evolutions of 'grazing' systems. The purple-shaded region indicates the Late-AGB phase, which lasts for $\sim$ 3 Myr. *Left*: system in which the inner companion's periastron (blue line) crosses V Hya's Roche limit (green dashed line, $q = 2.7$) during the L-AGB phase. Initial system parameters are $m_1 = 0.001$ M$_\odot$, $m_2 = 0.01$ M$_\odot$, $a_2 = 400$ au, $e_2 = 0.6$, $i = 105$ deg. *Middle*: system in which the inner companion's periastron (blue line) crosses V Hya's Roche limit (cyan dashed line, $q = 1.66$) during the L-AGB phase. Initial system parameters are $m_1 = 5 \times 10^{-5}$ M$_\odot$, $m_2 = 0.01$ M$_\odot$, $a_2 = 200$ au, $e_2 = 0.6$, $i = 35$ deg. *Right*: system in which the inner companion's orbit circularizes, and its semimajor axis (red line) crosses the Roche limit of V Hya (green dashed line, $q = 2.7$). Initial system parameters are $m_1 = 0.6$ M$_\odot$, $m_2 = 0.6$ M$_\odot$, $a_2 = 1000$ au, $e_2 = 0.6$, $i = 70$ deg.

We show in Fig. 3 how the mass of the inner companion (m_1) affects the evolution of the system. In the left-hand panel we illustrate the relationship between $D_{\rm min}$ and eccentricity. We define $D_{\rm min}$ as

$$D_{\rm min} = \min[(a_1(1-e_1)) - RL_{\rm VHya}], \quad (4)$$

valid in the secular approximation, compared to the orbital (or less than orbital) effects due to the drag force. In other words, if on an orbital time-scale the companion's velocity is changing significantly, then the secular approximation is invalid. So the question boils down to which force dominates over the orbital time-scale (the EKL produces forced eccentricity that remains constant over the entire $\sim$1 Myr in which the companion's periastron grazes the Roche limit of V Hya). Estimating the drag force as $F_{\rm drag} \approx 0.5\rho\pi R_1^2 v_1^2$, using $\rho = 10^{-8}$ g cm^{-3} (Lagadec et al. 2005), we a find very small change in velocity of the grazing companions (Jovians and brown dwarf-mass companions) due to the drag force ($<$ 1 per cent) over one orbit, the velocity will have been re-established by EKL again.

i.e. the minimum distance between the periastron of the inner orbit and V Hya's Roche limit ($D_{\rm min} = 0$ indicates Roche limit crossing, using $q = 2.7$). On the x-axis, we show the eccentricity at the time of $D_{\rm min}$ ($t_{D_{\rm min}}$, which occurs during the L-AGB phase). It is clear that most surviving stellar companions ($m_1 > 0.1$ M$_\odot$) circularize (reach final values of $e_1 \sim 0$). This is because stellar companions have larger radii than lower-mass objects, and since tides are highly dependent on the radius, their orbits circularize relatively quickly. Because of the relatively larger mass of stellar objects, the EKL mechanism isn't as effective since the distant tertiary has lower or similar mass.

Most companions with $m_1 = 0.1$ M$_\odot$ merge during or before the L-AGB phase, as indicated in the right-hand panel of Fig. 2. Most of the TCB systems contain a stellar mass $m_1 > 0.1$ M$_\odot$ companion, while brown dwarfs and planets ($m_1 < 0.1$ M$_\odot$) produce mainly grazing systems.

Most surviving non-stellar companions ($m_1 < 0.1$ M$_\odot$, i.e. Jovians and Brown dwarfs) follow a linear relation between $D_{\rm min}$

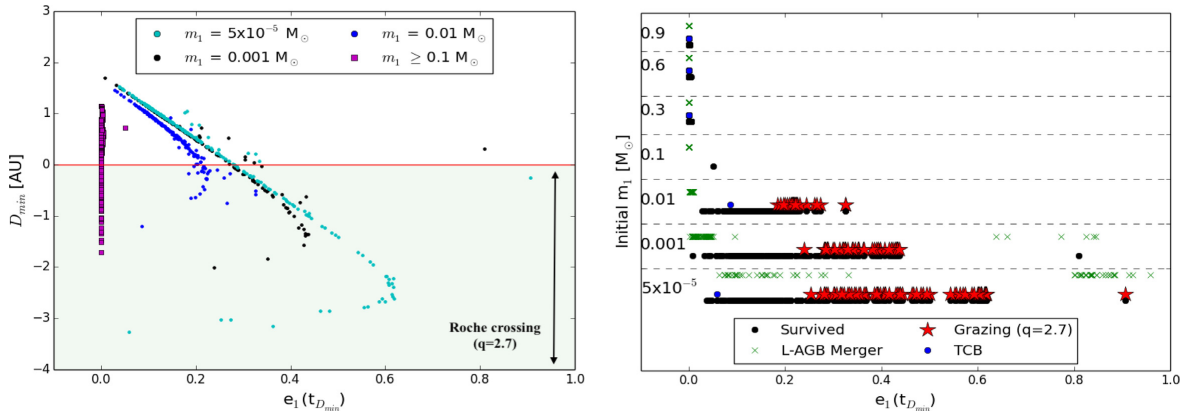

Figure 3. Illustration of how the end state of the system depends on the mass of the inner companion (m_1). *Left*: Plot of $D_{\rm min}$ (equation 4) versus the eccentricity of the inner orbit (e_1) at the time of minimum periastron distance to the primary's Roche limit ($t_{D\rm min}$, using $q = 2.7$). We do not include any merger system in this panel. Green-shaded region represents the Roche limit crossing. *Right*: Plot of outcomes as a function of initial m_1 versus and eccentricity of the inner orbit (e_1) at the time of minimum periastron distance to the primary's Roche limit ($t_{D\rm min}$, using $q = 2.7$). Stellar-mass ($m_1 > 0.1$ M$_\odot$, and a few planets) companions produce TCBs (blue dots), while planets (and brown dwarfs, all with $m_1 < 0.1$ M$_\odot$) produce grazing systems (red stars). Neptune-mass objects achieve the highest eccentricities. Green crosses (x) represent L-AGB mergers, and black dots (•) represent survivor systems (like those in the left-hand panel of Fig. 1).

and $e_1(t_{D\rm min})$. There is also a subtle mass dependence (see Fig. 3): lower-mass objects reach higher eccentricities. Using the upper limit value of $q = 2.7$, our simulations show that among all the objects that end up grazing the primary's Roche limit, there are more Neptune-mass objects than any other, followed by Jupiter-mass and brown dwarf companions. This is due to the fact that, for larger m_2/m_1 ratios, EKL effects approach the test particle approximation, in which the inner orbit achieves very high eccentricities. Moreover, tides become less effective for inner companions with small radii. Therefore, systems with Neptune-mass inner companions can graze V Hya's Roche limit with the highest eccentricities without being significantly affected by tidal forces.

We now examine constraints on the mass of the third, more distant companion, as well as its eccentricity and semimajor axis. Fig. 4 shows the percentage of grazing systems (relative to the total number of grazing brown dwarfs, Jupiters, and Neptunes) that contain different values of m_2, a_2, and e_2. Our results indicate that most grazing Neptunes were caused by far away ($a_2 \sim$ 800–1000 au), sub-solar mass companions ($m_2 > 0.1$ M$_\odot$; see the middle panel of Fig. 4). This is expected because a less massive tertiary would be torqued by m_1 (e.g. Naoz 2016; Naoz et al. 2017). Thus, a more massive m_2 is an expected consequence of the EKL mechanism. On the other hand, grazing brown dwarfs are more likely to take place for systems in which the tertiary is closer (as shown in Fig. 4, right-hand panel). This is also an expected consequence of the EKL mechanism (e.g. Naoz 2016). In this case, the ratio m_2/m_1 is smaller than those systems with Neptune-mass inner companions, and thus we need a closer tertiary for EKL effects to induce high eccentricities.

4 IMPLICATIONS FOR THE V HYA SYSTEM

4.1 Observational interpretation of the orbit

The model introduced by Sahai et al. (2016) suggests that the observed ejections from V Hya are associated with the periastron passage of an unseen companion in an eccentric orbit. Furthermore, their study suggested that the eccentricity of the companion has to be relatively large, $e \gtrsim 0.6$, in order for the companion to approach the primary within its stellar envelope at periastron.

However, here we relax the need for the companion to reach V Hya's radius, since crossing the Roche limit already provides an opportunity for interactions between V Hya and the companion. Furthermore, the low surface gravity, stellar pulsations, and their associated shocks, coupled with the radiation pressure that drives V Hya's stellar wind cause an increased scale height of its atmosphere, and therefore a measurable radius is not clearly definable (Zhao-Geisler et al. 2012).

4.2 Launching mechanism

The launching mechanism of the observed bullet ejections is largely uncertain. Here we consider the consequences of a few simple proof-of-concept launching mechanisms on our proposed scenario.

(i) The ballistic approximation (e.g. Dosopoulou, Naoz & Kalogera 2017) yields that the bullet speed $v_{\rm b}$ should be proportional to the periastron speed $v_{\rm p}$ plus the escape speed from the companion $v_{\rm esc}$, i.e.

$$v_{\rm b} \sim \sqrt{G(M_{\rm VHya} + m_c)\frac{1+e}{a(1-e)}} + \sqrt{\frac{2Gm_c}{r_c}} \qquad (5)$$

where $m_{\rm c}$ is the mass of the companion and $r_{\rm c}$ is its radius. A similar estimation was done by Livio (1997). As can be seen from equation (5), the jet's velocity is highly sensitive to the mass of the companion. In our case, each companion reaches different maximum eccentricity (see Fig. 3), however the pericenter velocity is typically much smaller than the escape velocity. In Fig. 5 we show ejection speed according to these approximations for different companions (Neptune, Jupiter, and brown dwarf). A brown dwarf gives an ejection speed of about 230 km s^{-1}, similar to the observed bullet speeds ($v \sim$ 200–250 km s^{-1}; Sahai et al. 2016; Scibelli, Sahai & Morris 2019).

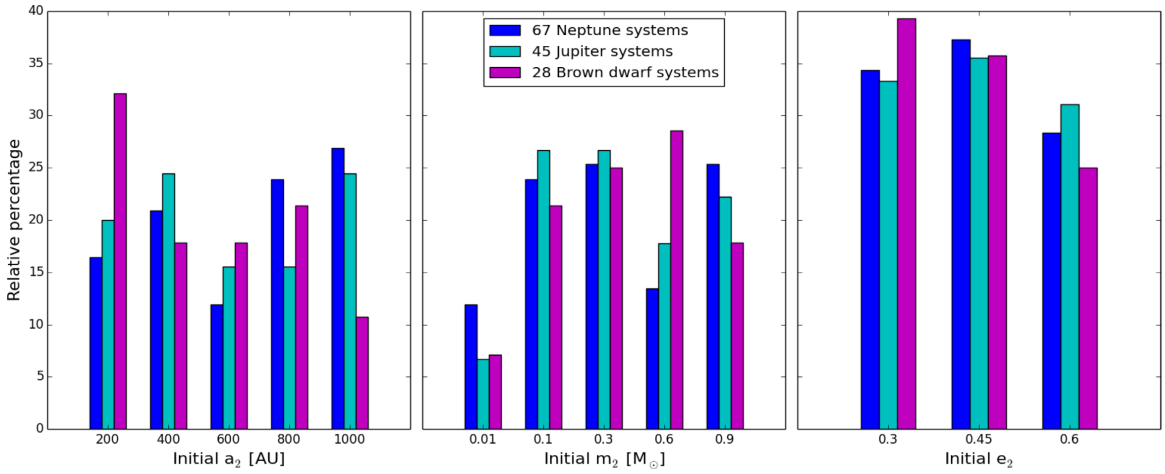

Figure 4. Percentages of Neptune, Jupiter, and brown dwarf systems (relative to total of grazing systems) for the values of m_2, a_2, and e_2. For example, in 33 per cent out of 28 systems with a brown dwarf (i.e. 9 systems), the location of m_2 is 200 au.

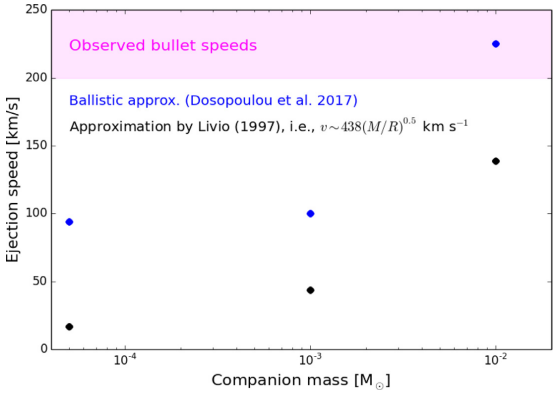

Figure 5. Jet ejection speed versus companion mass (for Neptune, Jupiter, and brown dwarf masses). Black dots represent the approximation by Livio (1997). The blue dots represent the ballistic approximation (Dosopoulou et al. 2017). The magenta-shaded region indicates the range of the observed bullets' speeds.

(ii) We also consider a magnetically driven launching mechanism. Following Fendt (2003), we consider an outflow velocity from a circum-planetary accretion disc:

$$v_{\rm b} \approx 63 \text{ km s}^{-1} \left(\frac{\Phi}{5\times10^{22}\text{ G cm}^2}\right)^{2/3} \left(\frac{P}{4\text{ d}}\right)^{-2/3} \times \left(\frac{\dot{M}_{\rm out}}{10^{-3}\,\dot{\rm M}_{\rm in}}\right)^{-1/3} \left(\frac{\dot{M}_{in}}{6\times10^{-5}\,{\rm M_J/yr}}\right)^{-1/3} \quad (6)$$

where Φ is the magnetic flux through the accretion disc, P is the outer edge disc's period, $\dot{M}_{\rm in}$ is the inflow rate, and $\dot{M}_{\rm out}$ is the outflow rate. If the companion swings through V Hya's Roche limit and forms a transient accretion disc,[4] we might expect ejections due to magnetically driven jets. This mechanism is sensitive to the magnetic field of the system. For example, some studies have suggested that Jupiter's magnetic field could have been as high as $\sim$ 500 G during its early formation period (Christensen, Holzwarth & Reiners 2009; Batygin 2018). Furthermore, one version of the model we propose here, i.e. a Jovian planet around V Hya, might resemble the environment of a protoplanetary system, and thus, we could consider magnetic field strengths of 500 G or greater. Similar to Fendt (2003), we adopt $10 \times R_{\rm c}$ as the outer disc edge. We also adopt $\dot{M}_{\rm out} = \dot{M}_{\rm in}$, i.e. all of the accreted mass is ejected. In Fig. 6 we show the ejection speed as a function of mass accretion rate, using values of $B = 500$ and 2000 G. As shown in the figure, accretion rates of $\sim 10^{-7}$ M$_\odot$/yr and a strong magnetic field ($B = 2000$ G) are necessary for a Jovian planet to cause ejection speeds of $\sim$200 km s^{-1}.

(iii) Another launching mechanism is described in Goodson & Winglee (1999). In their work, they considered accretion jets from accreting magnetic young stellar objects. They found that the ejection speeds are

$$v_{\rm b} = 585 P_{\rm d}^{-2/3} B_{\rm kG}^{2/3} R^{4/3} \dot{M}_8^{-1/3} \sin^{4/3}\theta_{\rm jet} \text{ km s}^{-1} \quad (7)$$

where $P_{\rm d}$ is the stellar rotation period in days, $B_{\rm kG}$ is the stellar surface magnetic field in kilogauss, R is the stellar radius in solar radii, $\dot{M}_8$ is the jet mass flux in units of 10^{-8} M$_\odot$/yr, and $\theta_{\rm jet}$ is the angle of ejection. For simplicity, we assume $\sin\theta_{\rm jet} = 1$, and a maximally rotating Jovian planet ($P_{\rm d} \approx 0.2$ d). We consider the same values of B and $\dot{M}_{\rm in}$ as before, and show the resulting jet speed values in Fig. 6. The speeds resulting from this mechanism are lower than those produced using equation (6).

4.3 Relevance for companions around evolved stars

In recent years a number of evolved stars have been observed to host Hot Jupiter companions (e.g. Johnson et al. 2008; Sato et al. 2008; Johnson et al. 2010, 2011a,b; Johnson, Morton & Wright 2013; Sato et al. 2013; Bieryla et al. 2014; Wittenmyer et al. 2015a,b).

[4]Note that the time-scales to form an accretion disk ($t \sim (G\rho)^{-1/2} \sim 1.2$ yr) is too long compared to the few months the companion typically spends inside the Roche limit. However, an accretion disc might be accumulated over one or more orbital revolution time-scale.

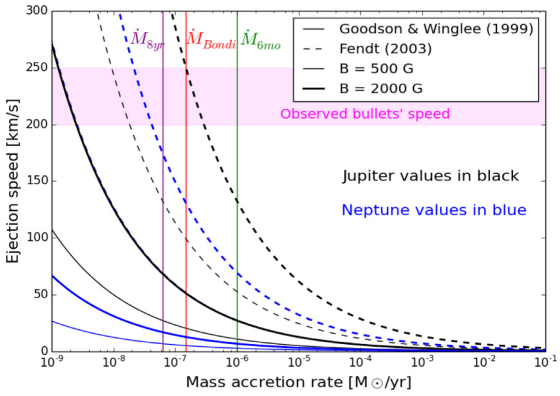

Figure 6. Plot of ejection speed versus mass input rate. Solid lines represent ejection speed values according to equation (7) (Goodson & Winglee 1999). Dashed lines represent values according to equation (6) (Fendt 2003). Black lines represent values due to a Jupiter planet, while blue lines represent values for a Neptune planet. Thicker lines represent values with $B = 2000$ G, while thinner lines represent values with $B = 500$ G. We also indicate some possible values of the mass accretion rate ($\dot{M}_{\rm in}$). The vertical purple line indicates the value due to the accretion of 1 bullet mass ($\sim 10^{27}$ g, Sahai et al. 2016) over 1 orbit (8 yr). Similarly, the vertical green line indicates the rate of accretion of 1 bullet mass over 6 months. The vertical red line represents Bondi accretion, assuming a density $\rho \sim 10^{-8}$ g cm^{-3} (estimate taken from Lagadec et al. 2005).

Recent work by Stephan et al. (2018) indicates the existence of a population of 'Temporary Hot Jupiters' (THJs), of which V Hya's unseen companion could be an example. In this model, a giant planet orbiting its parent star at a significant distance is perturbed by an outer stellar companion to reach high eccentricity values. Once the parent star becomes a red giant, tidal forces bring the planet closer, becoming Hot Jupiters until they are eventually engulfed by the expanding star. However, our model here suggests that a subset of these THJs would in fact become V Hya-like systems when they begin to interact with the expanding star's extended envelope. It can, thus, be speculated that a number of observed Hot Jupiters orbiting evolved stars are indeed progenitors of future V Hya-like objects.

5 SUMMARY

In this paper, we propose a dynamical configuration for the AGB star, V Hya, that accounts for its apparently periodic 'bullet' ejections. In our model, V Hya is part of a hierarchical triple system. The inner, 8.5-yr period orbit is composed of V Hya and a low-mass companion, and they are orbited by a distant tertiary. We have evolved a large set (2625) of realizations of this system, varying the masses, as well as the orbital separations, eccentricities, and inclinations of the system. Our goal is to constrain the parameter space for which a V Hya-like system can occur. We include the EKL mechanism, tides, general relativity, and post-main-sequence stellar evolution. The eccentricity oscillations associated with the EKL mechanism can potentially drive the inner companion to cross inside the primary's Roche limit. Such an interaction could produce jet-like ejections via a strongly enhanced accretion episode.

Our results can be summarized as follows:

(i) **Mergers**. In $\sim$37 per cent of all simulated cases, the inner companion merges with the primary, either due to strong tides during the primary's Late AGB phase, or due to extreme EKL effects that lead to a merger before the AGB phase.

(ii) **Surviving systems**. In $\sim$62 per cent of the simulated systems, the inner companion survives the evolution of the primary star until its WD phase without merging. Our investigation focuses on the subset of these cases that achieves Roche-limit crossing at periastron during the primary's Late AGB phase.

(iii) **Late-AGB, grazing systems**: cases that could potentially give rise to a V Hya-like system. In these systems, the inner companion's orbit reaches a high eccentricity ($e_1 > 0.1$) during the primary's Late-AGB phase and crosses the primary's Roche limit during periastron passage. Thus, the inner companion could, in principle, accrete material during this period. The percentage of systems in this category depends on the properties of the evolved star's envelope as well as the details of the interactions of the close-by companion with the Roche limit (Guillochon et al. 2011; Liu et al. 2013). We characterize this by adopting two different numerical pre-factors for the Roche limit. Specifically, in equation (1), we find that for $q = 2.7$ ($q = 1.66$), $\sim$5 per cent ($\sim$1 per cent) of all simulated systems may become V Hya-like systems. It is not surprising that only small percentage of the systems present this behavior as we are constraining ourselves to a very short time-scale in the evolution of the star (the Late-AGB phase represents 1/400 of our simulation time-scale). Grazing systems only occur with brown dwarfs, Jupiter, and Neptune-mass inner companions (Fig. 3). We can then estimate a possible mass and semimajor axis of the distant tertiary (Fig. 4). For example, we find more systems with a brown dwarf inner companion and a relatively close ($a_2 \sim 200$ au), stellar-mass ($m_2 \sim 0.6$ M$_\odot$) tertiary.

(iv) **Late AGB, temporary close binaries (TCBs)**. Unlike the systems in which their orbit circularizes and shrinks, in TCBs tides work to circularize the inner orbit during the primary's Late AGB phase, and the secondary migrates inside the primary's Roche limit, but a merger does not occur. Specifically, the mass-loss expands the semimajor axis, which helps the companion elude engulfment. We find these systems only when using a value of $q = 2.7$ in the definition of the Roche limit, and in $\sim$2 per cent of all cases we analyzed. While these cases would not produce V Hya-like systems, they are likely to end up as common envelope configurations because of the drag encountered inside the Roche limit. Most systems in this category contain stellar-mass inner companions ($m_1 > 0.1$ M$_\odot$).

Finally, we consider some possible launching mechanisms that could give rise to V Hya-like ejections. In particular, we examine a simple ballistic approach, as well as magnetically driven ejection processes that were suggested in the literature for proto-planetary systems and young stellar objects. Interestingly, we find (Fig. 5) that a simple ballistic mechanism can produce the observed ejection velocity for a brown dwarf companion. However, this version of our model causes tension with the companion's suggested eccentricity ($e_1 > 0.6$; Sahai et al. 2016), since our results indicate that tidal effects may limit a brown dwarf companion's eccentricity below $\sim$0.2. Note that Sahai et al. (2016) suggested an eccentricity that was based on the companion approaching V Hya's envelope at periastron ($R_{\rm VHya} \sim 2$ au). We relax this condition in our investigation.

Nevertheless, our results indicate that Jovian companions achieve the highest eccentricities during V Hya's Late AGB phase ($e_1 \sim 0.6$ for Neptune-mass companions, in agreement with the eccentricity suggested by Sahai et al. 2016). Here, a purely ballistic ejection does not produce speeds that match observations. Instead, a strong magnetic field ($B > 500$ G) is necessary for magnetically driven outflows

from a Jovian companion to achieve speeds of $\gtrsim 200\,\mathrm{km\,s^{-1}}$ (Fig. 6). This prediction can be used to distinguish competing mechanisms.

This proof-of-concept study suggests that V Hya-like ejections can result from EKL-induced interactions between AGB stars and Jovian or brown dwarf companions. The model presented here also provides a framework to explain the dynamics occuring in interacting binary systems in which the companion is a stellar, sub-stellar, or planetary object. This includes, for example, planets engulfed by giant stars (e.g. Soker, Livio & Harpaz 1984; Livio & Soker 2002; Gaudi et al. 2017; Stephan et al. 2018), the influence of planets on horizontal giant branch morphology (e.g. Soker 1998a), as well as binary progenitor models of bipolar PNe (e.g. Morris 1987; Soker 1998b).

ACKNOWLEDGEMENTS

The authors want to thank the reviewer whose comments and suggestions helped improve and clarify this manuscript. This work used computational and storage services associated with the Hoffman2 Shared Cluster provided by the UCLA Institute for Digital Research and Education's Research Technology Group. This material is based upon work supported by the National Science Foundation Graduate Research Fellowship Program under Grant No. DGE-1144087. S.N. and A.P.S. acknowledge partial support from the NSF through Grant AST-1739160.

REFERENCES

Balick B., Frank A., 2002, ARA&A, 40, 439
Batygin K., 2018, AJ, 155, 178
Bieryla A. et al., 2014, AJ, 147, 84
Christensen U. R., Holzwarth V., Reiners A., 2009, Nature, 457, 167
Dosopoulou F., Naoz S., Kalogera V., 2017, ApJ, 844, 12
Eggleton P. P., Kiseleva L. G., Hut P., 1998, ApJ, 499, 853
Eggleton P. P., Kisseleva-Eggleton L., Dearborn X., 2007, in Hartkopf W. I., Harmanec P., Guinan E. F., eds, IAU Symp. Vol. 240, Binary Stars as Critical Tools and Tests in Contemporary Astrophysics. Kluwer, Dordrecht, p. 347
Fendt C., 2003, A&A, 411, 623
Gaudi B. S. et al., 2017, Nature, 546, 514
Goodson A. P., Winglee R. M., 1999, ApJ, 524, 159
Griffin R. F., 2012, JA&A, 33, 29
Guillochon J., Ramirez-Ruiz E., Lin D., 2011, ApJ, 732, 74
Hirano N. et al., 2004, ApJ, 616, L43
Hurley J. R., Pols O. R., Tout C. A., 2000, MNRAS, 315, 543
Hut P., 1980, A&A, 92, 167
Johnson J. A. et al., 2011a, AJ, 141, 16
Johnson J. A. et al., 2011b, ApJS, 197, 26
Johnson J. A., Marcy G. W., Fischer D. A., Wright J. T., Reffert S., Kregenow J. M., Williams P. K. G., Peek K. M. G., 2008, ApJ, 675, 784
Johnson J. A., Howard A. W., Bowler B. P., Henry G. W., Marcy G. W., Wright J. T., Fischer D. A., Isaacson H., 2010, PASP, 122, 701
Johnson J. A., Morton T. D., Wright J. T., 2013, ApJ, 763, 53
Knapp G. R., Jorissen A., Young K., 1997, A&A, 326, 318
Kozai Y., 1962, AJ, 67, 591
Lagadec E., Mékarnia D., de Freitas Pacheco J. A., Dougados C., 2005, A&A, 433, 553
Li G., Naoz S., Kocsis B., Loeb A., 2014a, ApJ, 785, 116
Li G., Naoz S., Holman M., Loeb A., 2014b, ApJ, 791, 86
Lidov M. L., 1962, Planet. Space Sci., 9, 719
Lithwick Y., Naoz S., 2011, ApJ, 742, 94
Liu S.-F., Guillochon J., Lin D. N. C., Ramirez-Ruiz E., 2013, ApJ, 762, 37
Livio M., 1997, in Wickramasinghe D. T., Bicknell G. V., Ferrario L., eds, ASP Conf. Ser. Vol. 121, IAU Colloq. 163: Accretion Phenomena and Related Outflows. Astron. Soc. Pac., San Francisco, p. 845
Livio M., Soker N., 2002, ApJ, 571, L161
Lloyd Evans T., 1991, MNRAS, 248, 479
Matsumura S., Peale S. J., Rasio F. A., 2010, ApJ, 725, 1995
Michaely E., Perets H. B., 2016, MNRAS, 458, 4188
Morris M., 1987, PASP, 99, 1115
Naoz S., 2016, ARA&A, 54, 441
Naoz S., Fabrycky D. C., 2014, ApJ, 793, 137
Naoz S., Farr W. M., Rasio F. A., 2012, ApJ, 754, L36
Naoz S., Farr W. M., Lithwick Y., Rasio F. A., Teyssandier J., 2013a, MNRAS, 431, 2155
Naoz S., Kocsis B., Loeb A., Yunes N., 2013b, ApJ, 773, 187
Naoz S., Fragos T., Geller A., Stephan A. P., Rasio F. A., 2016, ApJ, 822, L24
Naoz S., Li G., Zanardi M., de Elía G. C., Di Sisto R. P., 2017, AJ, 154, 18
Paczyński B., 1971, ARA&A, 9, 183
Perets H. B., Fabrycky D. C., 2009, ApJ, 697, 1048
Perets H. B., Kratter K. M., 2012, ApJ, 760, 99
Petrovich C., 2015, ApJ, 799, 27
Pribulla T., Rucinski S. M., 2006, AJ, 131, 2986
Prodan S., Antonini F., Perets H. B., 2015, ApJ, 799, 118
Raghavan D. et al., 2010, ApJS, 190, 1
Sahai R., Trauger J. T., 1998, AJ, 116, 1357
Sahai R., Morris M., Knapp G. R., Young K., Barnbaum C., 2003, Nature, 426, 261
Sahai R., Sugerman B. E. K., Hinkle K., 2009, ApJ, 699, 1015
Sahai R., Morris M. R., Villar G. G., 2011, AJ, 141, 134
Sahai R., Scibelli S., Morris M. R., 2016, ApJ, 827, 92
Sato B. et al., 2008, PASJ, 60, 539
Sato B. et al., 2013, PASJ, 65, 85
Scibelli S., Sahai R., Morris M. R., 2019, ApJ, 870, 117
Shappee B. J., Thompson T. A., 2013, ApJ, 766, 64
Soker N., 1998a, AJ, 116, 1308
Soker N., 1998b, ApJ, 496, 833
Soker N., Livio M., Harpaz A., 1984, MNRAS, 210, 189
Stephan A. P., Naoz S., Ghez A. M., Witzel G., Sitarski B. N., Do T., Kocsis B., 2016, MNRAS, 460, 3494
Stephan A. P., Naoz S., Zuckerman B., 2017, ApJ, 844, L16
Stephan A. P., Naoz S., Gaudi B. S., 2018, AJ, 156, 128
Teyssandier J., Naoz S., Lizarraga I., Rasio F. A., 2013, ApJ, 779, 166
Tokovinin A., 2008, MNRAS, 389, 925
Tokovinin A., 2014a, AJ, 147, 86
Tokovinin A., 2014b, AJ, 147, 87
Tokovinin A., Thomas S., Sterzik M., Udry S., 2006, A&A, 450, 681
Tokovinin A. A., 1997a, Astron. Lett., 23, 727
Tokovinin A. A., 1997b, A&AS, 124, 75
Toonen S., Hamers A., Portegies Zwart S., 2016, Comput. Astrophys. Cosmol., 3, 6
Wittenmyer R. A., Gao D., Hu S. M., Villaver E., Endl M., Wright D., 2015a, PASP, 127, 1021
Wittenmyer R. A., Wang L., Liu F., Horner J., Endl M., Johnson J. A., Tinney C. G., Carter B. D., 2015b, ApJ, 800, 74
Zhao-Geisler R., Quirrenbach A., Köhler R., Lopez B., 2012, A&A, 545, A56

This paper has been typeset from a TEX/LATEX file prepared by the author.

Bibliography

Alig C., Burkert A., Johansson P. H., Schartmann M., 2011, MNRAS, 412, 469

Ao Y., et al., 2013, A&A, 550, A135

Armillotta L., Krumholz M. R., Di Teodoro E. M., McClure-Griffiths N. M., 2019, MNRAS, 490, 4401

Athanassoula E., 1992, MNRAS, 259, 345

Attwood R. E., Goodwin S. P., Whitworth A. P., 2007, A&A, 464, 447

Ballone A., Mapelli M., Trani A. A., 2019, MNRAS, 488, 5802

Balsara D. S., 1995, Journal of Computational Physics, 121, 357

Barnes J., Hut P., 1986, Nature, 324, 446

Becklin E. E., Gatley I., Werner M. W., 1982, ApJ, 258, 135

Binney J., Gerhard O. E., Stark A. A., Bally J., Uchida K. I., 1991, MNRAS, 252, 210

Bland-Hawthorn J., Gerhard O., 2016, ARA&A, 54, 529

Blank M., Morris M. R., Frank A., Carroll-Nellenback J. J., Duschl W. J., 2016, MNRAS, 459, 1721

Bonnell I. A., Rice W. K. M., 2008, Science, 321, 1060

Bradford C. M., Stacey G. J., Nikola T., Bolatto A. D., Jackson J. M., Savage M. L., Davidson J. A., 2005, ApJ, 623, 866

Burkhart B., 2018, ApJ, 863, 118

Burkhart B., Falceta-Gonçalves D., Kowal G., Lazarian A., 2009, ApJ, 693, 250

Buta R. J., 2017a, MNRAS, 470, 3819

Buta R. J., 2017b, MNRAS, 471, 4027

Buta R., Combes F., 1996, Fund. Cosmic Phys., 17, 95

Carroll-Nellenback J. J., Shroyer B., Frank A., Ding C., 2013, Journal of Computational Physics, 236, 461

Chen Y.-M., Wang J.-M., Yan C.-S., Hu C., Zhang S., 2009, ApJ, 695, L130

Chevalier R. A., 1974, ApJ, 188, 501

Chiou Y. S., Naoz S., Burkhart B., Marinacci F., Vogelsberger M., 2019, ApJ, 878, L23

Christopher M. H., Scoville N. Z., Stolovy S. R., Yun M. S., 2005, ApJ, 622, 346

Cioffi D. F., McKee C. F., Bertschinger E., 1988, ApJ, 334, 252

Clark P. C., Glover S. C. O., Klessen R. S., Bromm V., 2011, ApJ, 727, 110

Collin S., Zahn J. P., 2008, A&A, 477, 419

Comerón S., 2013, A&A, 555, L4

Comerón S., Knapen J. H., Beckman J. E., Laurikainen E., Salo H., Martínez-Valpuesta I., Buta R. J., 2010, MNRAS, 402, 2462

Cowie L. L., McKee C. F., Ostriker J. P., 1981, ApJ, 247, 908

Cox D. P., 1972, ApJ, 178, 159

Cunningham A. J., Frank A., Varnière P., Mitran S., Jones T. W., 2009, ApJS, 182, 519

D'Onghia E., Vogelsberger M., Hernquist L., 2013, ApJ, 766, 34

Davies R. I., Müller Sánchez F., Genzel R., Tacconi L. J., Hicks E. K. S., Friedrich S., Sternberg A., 2007, ApJ, 671, 1388

Dinh C. K., Salas J. M., Morris M. R., Naoz S., 2021, arXiv e-prints, p. arXiv:2102.09569

Do T., Ghez A. M., Morris M. R., Lu J. R., Matthews K., Yelda S., Larkin J., 2009, ApJ, 703, 1323

Do T., Lu J. R., Ghez A. M., Morris M. R., Yelda S., Martinez G. D., Wright S. A., Matthews K., 2013, ApJ, 764, 154

Dubinski J., Narayan R., Phillips T. G., 1995, ApJ, 448, 226

Dwarkadas V. V., Gruszko J., 2012, MNRAS, 419, 1515

Efstathiou G., Davis M., White S. D. M., Frenk C. S., 1985, ApJS, 57, 241

Elmegreen B. G., Scalo J., 2004a, ARA&A, 42, 211

Elmegreen B. G., Scalo J., 2004b, ARA&A, 42, 211

Emsellem E., Renaud F., Bournaud F., Elmegreen B., Combes F., Gabor J. M., 2015, MNRAS, 446, 2468

Etxaluze M., Smith H. A., Tolls V., Stark A. A., González-Alfonso E., 2011, AJ, 142, 134

Federrath C., Roman-Duval J., Klessen R. S., Schmidt W., Mac Low M.-M., 2010, A&A, 512, A81

G. R. Liu M. B. Liu G.-R. L., 2003, Smoothed Particle Hydrodynamics: A Meshfree Particle Method. World Scientific Publishing Co.

Gallego S. G., Cuadra J., 2017, MNRAS, 467, L41

Genzel R., 1989, in Morris M., ed., IAU Symposium Vol. 136, The Center of the Galaxy. p. 393

Genzel R., Watson D. M., Crawford M. K., Townes C. H., 1985, ApJ, 297, 766

Genzel R., Eisenhauer F., Gillessen S., 2010, Reviews of Modern Physics, 82, 3121

Gerhard O. E., 1996, in Blitz L., Teuben P. J., eds, IAU Symposium Vol. 169, Unsolved Problems of the Milky Way. p. 79 (arXiv:astro-ph/9604069)

Ghez A. M., et al., 2008, ApJ, 689, 1044

Ginsburg A., et al., 2016, A&A, 586, A50

Goicoechea J. R., Pety J., Chapillon E., Cernicharo J., Gerin M., Herrera C., Requena-Torres M. A., Santa-Maria M. G., 2018, A&A, 618, A35

Güsten R., Walmsley C. M., Pauls T., 1981, A&A, 103, 197

Güsten R., Genzel R., Wright M. C. H., Jaffe D. T., Stutzki J., Harris A. I., 1987, ApJ, 318, 124

Harada N., et al., 2015, A&A, 584, A102

Henshaw J. D., et al., 2016, MNRAS, 457, 2675

Hildebrand R. H., Gonatas D. P., Platt S. R., Wu X. D., Davidson J. A., Werner M. W., Novak G., Morris M., 1990, ApJ, 362, 114

Hildebrand R. H., Davidson J. A., Dotson J., Figer D. F., Novak G., Platt S. R., Tao L., 1993, ApJ, 417, 565

Ho P. T. P., Ho L. C., Szczepanski J. C., Jackson J. M., Armstrong J. T., 1991, Nature, 350, 309

Hobbs A., Nayakshin S., 2009, MNRAS, 394, 191

Hobbs A., Nayakshin S., Power C., King A., 2011, MNRAS, 413, 2633

Hockney R. W., Eastwood J. W., 1988, Computer simulation using particles

Hopkins P. F., 2015, MNRAS, 450, 53

Hsieh P.-Y., Koch P. M., Ho P. T. P., Kim W.-T., Tang Y.-W., Wang H.-H., Yen H.-W., Hwang C.-Y., 2017, ApJ, 847, 3

Hsieh P.-Y., Koch P. M., Kim W.-T., Ho P. T. P., Tang Y.-W., Wang H.-H., 2018, ApJ, 862, 150

Huettemeister S., Wilson T. L., Bania T. M., Martin-Pintado J., 1993, A&A, 280, 255

Immer K., Kauffmann J., Pillai T., Ginsburg A., Menten K. M., 2016, A&A, 595, A94

Jackson J. M., Geis N., Genzel R., Harris A. I., Madden S., Poglitsch A., Stacey G. J., Townes C. H., 1993, ApJ, 402, 173

Jenkins A., Binney J., 1994, MNRAS, 270, 703

Joung M. K. R., Mac Low M.-M., 2006, ApJ, 653, 1266

Julian W. H., Toomre A., 1966, ApJ, 146, 810

Keller B. W., Kruijssen J. M. D., 2020, arXiv e-prints, p. arXiv:2004.03608

Kim W.-T., Stone J. M., 2012, ApJ, 751, 124

Kim S. S., Saitoh T. R., Jeon M., Figer D. F., Merritt D., Wada K., 2011, ApJ, 735, L11

Kim W.-T., Seo W.-Y., Stone J. M., Yoon D., Teuben P. J., 2012, ApJ, 747, 60

Klessen R. S., 2000, ApJ, 535, 869

Knapen J. H., 2005, A&A, 429, 141

Kolmogorov A., 1941, Akademiia Nauk SSSR Doklady, 30, 301

Kruijssen J. M. D., Longmore S. N., Elmegreen B. G., Murray N., Bally J., Testi L., Kennicutt R. C., 2014, MNRAS, 440, 3370

Kruijssen J. M. D., Dale J. E., Longmore S. N., 2015, MNRAS, 447, 1059

Krumholz M. R., Kruijssen J. M. D., 2015, MNRAS, 453, 739

Krumholz M. R., McKee C. F., 2005, ApJ, 630, 250

Lau R. M., Herter T. L., Morris M. R., Becklin E. E., Adams J. D., 2013, ApJ, 775, 37

Lewis B. T., Bate M. R., Tricco T. S., 2016, preprint, (arXiv:1606.06972)

Longmore S. N., et al., 2013, MNRAS, 429, 987

Lynden-Bell D., Pringle J. E., 1974, MNRAS, 168, 603

Mac Low M.-M., 1999, ApJ, 524, 169

Mac Low M.-M., Klessen R. S., 2004, Reviews of Modern Physics, 76, 125

Mac Low M.-M., Klessen R. S., Burkert A., Smith M. D., 1998, Physical Review Letters, 80, 2754

Machida M., et al., 2009, PASJ, 61, 411

Machida M., Nakamura K. E., Kudoh T., Akahori T., Sofue Y., Matsumoto R., 2013, ApJ, 764, 81

Mapelli M., Trani A. A., 2016, A&A, 585, A161

Mapelli M., Hayfield T., Mayer L., Wadsley J., 2012, ApJ, 749, 168

Marr J. M., Wright M. C. H., Backer D. C., 1993, ApJ, 411, 667

Marshall J., Lasenby A. N., Harris A. I., 1995, MNRAS, 277, 594

Martín S., Martín-Pintado J., Montero-Castaño M., Ho P. T. P., Blundell R., 2012, A&A, 539, A29

Martini P., Pogge R. W., 1999, AJ, 118, 2646

Martini P., Regan M. W., Mulchaey J. S., Pogge R. W., 2003a, ApJS, 146, 353

Martini P., Regan M. W., Mulchaey J. S., Pogge R. W., 2003b, ApJS, 146, 353

Martini P., Regan M. W., Mulchaey J. S., Pogge R. W., 2003c, ApJ, 589, 774

McKee C. F., Ostriker J. P., 1977, ApJ, 218, 148

McKee C. F., Ostriker E. C., 2007, ARA&A, 45, 565

Mezger P. G., Zylka R., Salter C. J., Wink J. E., Chini R., Kreysa E., Tuffs R., 1989, A&A, 209, 337

Mills E. A. C., Güsten R., Requena-Torres M. A., Morris M. R., 2013, ApJ, 779, 47

Mills E. A. C., Togi A., Kaufman M., 2017, ApJ, 850, 192

Molinari S., et al., 2011, ApJ, 735, L33

Monaghan J. J., 2005, Reports on Progress in Physics, 68, 1703

Monaghan J. J., Gingold R. A., 1983, Journal of Computational Physics, 52, 374

Montero-Castaño M., Herrnstein R. M., Ho P. T. P., 2009, ApJ, 695, 1477

Morris M., 1990, in Beck R., Wielebinski R., Kronberg P. P., eds, IAU Symposium Vol. 140, Galactic and Intergalactic Magnetic Fields. pp 361–367

Morris M., 1994, in Genzel R., Harris A. I., eds, NATO Advanced Science Institutes (ASI) Series C Vol. 445, NATO Advanced Science Institutes (ASI) Series C. p. 185

Morris M., 1996, in Blitz L., Teuben P. J., eds, IAU Symposium Vol. 169, Unsolved Problems of the Milky Way. p. 247

Morris M., Serabyn E., 1996, ARA&A, 34, 645

Morris M., Polish N., Zuckerman B., Kaifu N., 1983, AJ, 88, 1228

Morris M., Ghez A. M., Becklin E. E., 1999, Advances in Space Research, 23, 959

Naoz S., Narayan R., 2014, ApJ, 791, L8

Nishiyama S., Schödel R., 2013, A&A, 549, A57

Norman M. L., Bryan G. L., 1999, in Miyama S. M., Tomisaka K., Hanawa T., eds, Astrophysics and Space Science Library Vol. 240, Numerical Astrophysics. p. 19 (arXiv:astro-ph/9807121), doi:10.1007/978-94-011-4780-4_3

Norman C. A., Ferrara A., 1996, ApJ, 467, 280

Oka T., Nagai M., Kamegai K., Tanaka K., 2011, ApJ, 732, 120

Padoan P., Jimenez R., Nordlund Å., Boldyrev S., 2004, Physical Review Letters, 92, 191102

Palouš J., Ehlerová S., Wünsch R., Morris M. R., 2020a, A&A, 644, A72

Palouš J., Ehlerová S., Wünsch R., Morris M. R., 2020b, A&A, 644, A72

Patsis P. A., Athanassoula E., 2000, A&A, 358, 45

Pavlovski G., Smith M. D., Mac Low M.-M., 2006, MNRAS, 368, 943

Pedregosa F., et al., 2011, Journal of Machine Learning Research, 12, 2825

Pogge R. W., Martini P., 2002, ApJ, 569, 624

Portail M., Gerhard O., Wegg C., Ness M., 2017, MNRAS, 465, 1621

Price D. J., 2007, PASA, 24, 159

Pringle J. E., 1981, ARA&A, 19, 137

Regan M. W., Mulchaey J. S., 1999, AJ, 117, 2676

Requena-Torres M. A., et al., 2012, A&A, 542, L21

Roberts W. W. J., Huntley J. M., van Albada G. D., 1979, ApJ, 233, 67

Rogallo R. S., 1981, NASTM, 81315

Rosdahl J., Schaye J., Dubois Y., Kimm T., Teyssier R., 2017, MNRAS, 466, 11

Salas J. M., Naoz S., Morris M. R., Stephan A. P., 2019, MNRAS, 487, 3029

Salas J. M., Naoz S., Morris M. R., 2020, arXiv e-prints, p. arXiv:2010.04170

Salas J. M., Morris M. R., Naoz S., 2021, AJ, 161, 243

Sanders R. H., 1998, MNRAS, 294, 35

Sanders R. H., Huntley J. M., 1976, ApJ, 209, 53

Scannapieco C., et al., 2012, MNRAS, 423, 1726

Schmidt W., Hillebrandt W., Niemeyer J., 2006, Computers & Fluids, 35, 353

Schödel R., Merritt D., Eckart A., 2009, A&A, 502, 91

Seo W.-Y., Kim W.-T., Kwak S., Hsieh P.-Y., Han C., Hopkins P. F., 2019, ApJ, 872, 5

Serabyn E., Guesten R., Walmsley J. E., Wink J. E., Zylka R., 1986, A&A, 169, 85

Shakura N. I., Sunyaev R. A., 1973, A&A, 500, 33

Shin J., Kim S. S., Baba J., Saitoh T. R., Hwang J.-S., Chun K., Hozumi S., 2017, ApJ, 841, 74

Shukla H., Yun M. S., Scoville N. Z., 2004, ApJ, 616, 231

Slavin J. D., Cox D. P., 1992, ApJ, 392, 131

Smith I. L., Wardle M., 2014, MNRAS, 437, 3159

Sofue Y., 2007, PASJ, 59, 189

Sormani M. C., Binney J., Magorrian J., 2015a, MNRAS, 449, 2421

Sormani M. C., Binney J., Magorrian J., 2015b, MNRAS, 451, 3437

Sormani M. C., Binney J., Magorrian J., 2015c, MNRAS, 454, 1818

Sormani M. C., Sobacchi E., Fragkoudi F., Ridley M., Treß R. G., Glover S. C. O., Klessen R. S., 2018, MNRAS, 481, 2

Sormani M. C., et al., 2019, MNRAS, 488, 4663

Spergel D. N., Blitz L., 1992, Nature, 357, 665

Springel V., 2005, MNRAS, 364, 1105

Springel V., Hernquist L., 2002, MNRAS, 333, 649

Stolte A., Ghez A. M., Morris M., Lu J. R., Brandner W., Matthews K., 2008, ApJ, 675, 1278

Stone J. M., Ostriker E. C., Gammie C. F., 1998, ApJ, 508, L99

Sutton E. C., Danchi W. C., Jaminet P. A., Masson C. R., 1990, ApJ, 348, 503

Suzuki T. K., Fukui Y., Torii K., Machida M., Matsumoto R., 2015, MNRAS, 454, 3049

Trani A. A., Mapelli M., Ballone A., 2018, ApJ, 864, 17

Tress R. G., Sormani M. C., Glover S. C. O., Klessen R. S., Battersby C. D., Clark P. C., Hatchfield H. P., Smith R. J., 2020, MNRAS, 499, 4455

Tsuboi M., Kitamura Y., Uehara K., Tsutsumi T., Miyawaki R., Miyoshi M., Miyazaki A., 2018, PASJ, 70, 85

Vazquez-Semadeni E., 1994, ApJ, 423, 681

Vollmer B., Duschl W. J., 2001a, A&A, 367, 72

Vollmer B., Duschl W. J., 2001b, A&A, 377, 1016

Walch S., Naab T., 2015, MNRAS, 451, 2757

Wang J.-M., Yan C.-S., Li Y.-R., Chen Y.-M., Xiang F., Hu C., Ge J.-Q., Zhang S., 2009, ApJ, 701, L7

Wardle M., Yusef-Zadeh F., 2008, ApJ, 683, L37

Werner M. W., Davidson J. A., Morris M., Novak G., Platt S. R., Hildebrand R. H., 1988, ApJ, 333, 729

Wolfire M. G., Hollenbach D., McKee C. F., Tielens A. G. G. M., Bakes E. L. O., 1995, ApJ, 443, 152

Wright M. C. H., Coil A. L., McGary R. S., Ho P. T. P., Harris A. I., 2001, ApJ, 551, 254

Xu G., 1995, ApJS, 98, 355

Yusef-Zadeh F., 1989, in Morris M., ed., IAU Symposium Vol. 136, The Center of the Galaxy. p. 243

Yusef-Zadeh F., Morris M., 1987a, AJ, 94, 1178

Yusef-Zadeh F., Morris M., 1987b, ApJ, 322, 721

Yusef-Zadeh F., Morris M., 1988, ApJ, 329, 729

Yusef-Zadeh F., Morris M., Chance D., 1984, Nature, 310, 557

Zhao H., Spergel D. N., Rich R. M., 1994, AJ, 108, 2154